A NEW CONDUCTIVE MEMBRANE-BASED MICROFLUIDIC PLATFORM FOR ELECTROKINETIC APPLICATIONS

by

Xiaotong Fu

A dissertation submitted to Johns Hopkins University in conformity with the requirements for the degree of Doctor of Philosophy

Baltimore, Maryland

January 2017

© 2017 Xiaotong Fu

All Rights Reserved

Abstract

Micro-total-analysis-system (uTAS), a technology branches from the broader concept, microfluidics, has emerged as a powerful tool for many biological and chemical applications. uTAS typically features sample-to-answer designs, minute sample assumption and short processing time, which are highly desired in point-of-care diagnostics or high-throughput chemical analysis. Despite a large number of microfluidic devices reported with the uTAS concept, most designs were detection and sensitivity focused, ignored the necessary sample preparation steps. In recent years, the increasing demand for chip automation has boosted research efforts on sample preparation.

Electric force serves as one of the most applicable tools among on-chip sample processing techniques due to its portable and easy-integrating nature. To date, research has yielded a large number of designs utilizing electric field as a driving force, also known as electrokinetics, for on-chip sample processing, such as sample purification, enrichment, mixing and sorting. One biggest issue researchers countered using electric field is undesired surface reactions that may cause Faradaic reactions, electrode corrosion, and contaminations. While several microfluidic platforms have been developed to address this issue, there are still growing efforts to create new micro-design that are capable of providing sufficient electric field with improved stability, portability, and robustness.

This thesis seeks to address the electrokinetic-based on-chip sample preparation issue in two aspects, continuity and flow control, which represent two main challenges of on-chip sample preparation: a limited capability to continuously process samples and

lacking necessary modules for precise flow control under large extent chip integration. We first developed a new electrokinetic platform with integrated conductive membranes to effectively generate a uniform three-dimensional electric field inside microfluidic channels. The new design also has proved superiorities in avoiding surface reactions, improving portability, and reducing the fabrication cost. We then solved the continuity issue with a free flow electrophoresis device created from the platform. The free flow nature of the device allows for continuous sample throughput while adding electric field perpendicularly offers additional manipulating factors. Utilizing the newly developed free flow electrokinetic chip, we have successfully demonstrated two common on-chip sample processing functions: parallel separation and sample enrichment. On the other hand, the flow control issue is tackled by creating essential on-chip control modules under microfluidic setting. We have designed several microfluidic units with the platform to facilitate on-chip flow regulation, including micro-pumps, a sample injector, a local flow meter and a potential automatic control panel. All the flow control modules can be directly integrated into any soft lithography based sample processing modules without affecting the original designs, which significantly eases the integration difficulty. The ultimate goal of this research shall lead to a microfluidic platform that can perform essential on-chip sample pretreatments in a continuous manner and allows need-based customization. The platform shall be easily integrated with essential power functions and feedback mechanisms for automatic flow control, which offer a possibility to real highly integrated portable devices. Eventually, we can build the real uTAS by combining the platform with our real-time biosensor and turning it into a sample-to-answer uTAS.

In the first chapter of this thesis, a general background correlated to my research work is provided. The introduction includes the uTAS concept and its related technologies, explains the increasing demand for on-chip sample preparation techniques, and discusses current sample process modules using electrokinetic force. It leads to Chapter 2, where I summarize the current electrokinetic-based microfluidic platforms developed to address the surface reaction issue. Then we propose the new platform along with a theoretical model to characterize this design. An extensive comparison between available designs follows to demonstrate the advantages of this new platform, including the comparison specifically focusing on surface reactions. A detailed fabrication process flow is demonstrated in the end, showing how to fabricate this new platform design using one -step photolithography. Then the thesis splits into two parallel blocks, corresponding to the two challenges of on-chip sample preparation. The continuity challenge is addressed on the first block, chapter 3, where free flow electrophoresis device is presented and followed by two demonstrations of on-chip sample pretreatment functions: mixture separation and molecule enrichment. The second block of this thesis discusses the importance of on-chip flow control and the main obstacles that current technologies struggle with. Essential modules for on-chip flow control, such as electro-osmotic pumps, fluid regulation, sample injection techniques, pressure and flow meters, will be demonstrated in chapter 4-6, respectively. In conclusion, I will summarize all my previous research work and how to sketch the big picture of on-chip sample preparation with this platform. The results shall provide guidelines and inspirations for future on-chip sample preparation research.

Advisor

Zachary R. Gagnon, Ph.D.

Assistant Professor of Chemical & Biomolecular Engineering, Johns Hopkins University

Committee Members

Michael A. Bevan, Ph.D.

Professor of Chemical & Biomolecular Engineering, Johns Hopkins University

Joelle Frechette, Ph.D.

Associate Professor of Chemical & Biomolecular Engineering, Johns Hopkins University

Chao Wang, Ph.D.

Assistant Professor of Chemical & Biomolecular Engineering, Johns Hopkins University

Jordan J. Green, Ph.D

Associate Professor of Biomedical Engineering, Johns Hopkins University

Sung Hoon Kang, Ph.D.

Assistant Professor of Mechanical Engineering, Johns Hopkins University

Margarita Herrera-Alonso, Ph.D.

Assistant Professor of Materials Science & Engineering, Johns Hopkins University

Acknowledgements

I would not have been possible to complete my Ph.D. study without the incredible support and help from the following individuals. I sincerely appreciate their contributions to this thesis, as well as my Ph.D. study.

Foremost, I would like to thank my advisor Prof. Zachary Gagnon for the continuous support and guidance throughout the course of my Ph.D. program. He has provided me with innumerable opportunities to fly with my imagination and draw the big picture of my own research story. When I needed, he led me by hand and guided me through the difficult time. He devoted ample time towards educating me and provided me the freedom to learn. The way he solves a research problem and the creativity he stimulates inside our group will influence me throughout my entire life. He reached me when I was aimless about my future and pointed me the right direction to go. He is not only my research advisor, also a mentor of my life. He showed me another possible future and guided me through this adventure. Without him, my life in the past five years would be much different. I feel privileged to be the first Ph.D. student graduating from Prof. Gagnon's group and very proud of the work we have done.

I own my thanks to Prof. Michael Sano of the University of Stanford for guiding me through the initial stage of my Ph.D. research and providing valuable training sessions. His previous work and ideas significantly affected my original experiment design. I also want to acknowledge Dr. An Goffin of Johns Hopkins University. I appreciate her trustfulness and letting me lead the lab session of her course. This education experience significantly enhanced my understanding of my research.

I am very grateful to my GBO committee members, Prof. Joelle Frechette, Prof. Michael Bevan, Prof. Chao Wang from our department and Prof. Jordan J. Green from Biomedical engineering, Prof. Sung Hoon Kang from Mechanical engineering, Prof. Margarita Herrera-Alonso, from Material science. I am grateful to their time, patience and their intellectual contributions to my research development that inspiring me to further explore the field. I would like to express my sincere gratitude to their participation and kindness during my Ph.D. program.

I was very fortunate to be part of Gagnon's lab and met such a wonderful group of colleagues. Specifically, I want to thank Markela for the initial training when I first joined the lab. Nick is a great colleague to work with. We managed to complete many fantastic research work and publications together. I received many supports from Francesca and Mitch, who inspired me a lot during my Ph.D. research. Steven and Rob were the most impressive undergrads I ever worked with. I want to thank them for bringing all the supports and kindness, not only as a research colleague but also as a friend, to my five-year life at the US. Thanks for making me feel welcomed when the first time I came to this country.

I also own my thanks to all the friends I made at Hopkins. Yumo, Qianli, Dominic, Zhilin, Ning, Mike, Mengshu, Minglei, Xiaoqing, Leo, Jianli, I truly appreciate your selfless care and support during the past five years. We are roommates, close friends, classmates, and colleagues. Without you, my life at the US would be very difficult. I will remember all the happiness we had together and sincerely wish our path will cross again in the future.

Last, but not least, I want to express my most heartfelt thanks to my family. I am in debt to my parents and my parents-in-law. They always stand behind me and be my solid supporters. They are the strength encouraging me through my entire Ph.D. study and I really owe them my gratitude. I also want to give my greatest thankfulness to my loved wife. Any words I write here will fall short to express my gratefulness. You have been with me since the beginning and has always been my strength and motivation to move forward. You accompanied me during my darkest time and led me to the bright future. Without you, my whole Ph.D. life would be impossible and meaningless. Thank you.

Table of Contents

List of Figures

1. Introduction

1.1 History of micro-total-analysis-system (uTAS)

The concept of micro-total-analysis-system (uTAS) branched out from general microfluidic technology. uTAS is also referred as Lab-on-a-chip, a set of devices can miniaturize the entire sample analysis process in microliter scale. A completed uTAS device typically has two main functions: one is sample preparation, like sample injection, mixing, separation or enrichment; detection is the other part, where processed sample can be analyzed by certain manners, for example, optical imaging or electric signal. However, when we track back to the early days, uTAS was very simple and less functional.

A couple of decades ago, a gas chromatographic analyzer, which is considered as the first miniaturized device fabricated on silicon, was reported by Stanford University (1). It remarked a milestone of uTAS as the reported chromatography showed a fast separation of samples, which represent the nature of uTAS. Later on, more research works focusing on the fabrication of microstructures were reported, for instance, micropumps(2, 3), valves(4, 5) and sensors(6). The actual concept of uTAS had not been proposed until the early 1990s, when Manz et al.(7) presented a silicon chip integrated with sample pretreatment and detector. The concept and chip composition laid a foundation for nowadays uTAS devices. In the subsequent years, the number of reported uTAS designs increased dramatically as this field drew more attentions from chemists and biologists. Thanks to the advances in microfabrication techniques, uTAS devices

with smaller and much more complex structures can be fabricated. As a result, a wide range of device functions was published during this period, for example mixing(8), separation(9, 10) or cell manipulation(11) etc. This also led to the emergence of a new commercial market for biotech products. Many uTAS devices became commercially available at this time, thus further boost the growth of uTAS technology. In the later years, serving as a miniaturization of bench scale process, the functionality of uTAS kept expanding as new techniques were published. In the meantime, the complexity of the miniaturized processes also increased abruptly. uTAS started to show the capability to mimic complicated biological processes, like capillary electrophoresis with sample injector(12), DNA polymer chain reaction on a silicon chip(13), or even immunological assay that can analyze blood serum(14).

This trend becomes more obvious in current research: current uTAS typically has multiple function units on a single chip to fit the sample-to-answer requirement. This type of highly integrated designs became particularly advantageous for several reasons. The integration of different modules not only can avoid human errors and contaminations during sample transfer, also speed up the entire analysis process. However, full integration of required modular components is not a trivial task. The connection designs, the interactions between each module, proper setup of supporting units (including sample injection, pumping, purification etc) all require numerous troubleshooting. Consequentially, more research efforts have been spent on improving the capability of

the core function module to achieve better efficiency or sensitivity, rather than the essentialness of the sample preparation modules.

1.2 Microfabrication techniques

One of the biggest factors that lead to uTAS growth is the development of microfabrication. The past few decades have generated a wealth of new materials and techniques for fabricating micro-scale devices. Here we introduce common microfabrication techniques through two blocks, materials and patterning methods and each block will be further explored in detail.

1.2.1 Fabrication materials

Taking advantage of existing micromachining and microelectronic techniques, early microfluidic systems utilized silicon as the main substrate for fabrication. Standard photolithography and etching techniques, which will be cover later in this chapter, were frequently utilized to build microfluidic channels and other micro-structures at that time. However, despite the technical convenience, one biggest drawback from using silicon is the transparency issue. It is difficult to integrate optical detector or microscopic observation when silicon wafer presents. Besides, silicon is fairly expensive for large scale fabrication, which is contradictory to uTAS concept.

On the other hand, glass, another commonly used fabrication material, offers a number of advantages over silicon. Most obviously, the good transparency allows better

visualization of the microfluidic channel and easy optical detection. In a fabrication standpoint, the capability of glass to bond to other substrates like silicon and polymer provides glass a wide range of potential applications. Besides, glass is more compatible with electrokinetic applications ((15)), such as electro-osmosis. Overall, glass was considered as most suitable fabrication material at that time.

Then the predomination of glass ended short after the appearance of polydimethylsiloxane (PDMS) in 1990's. PDMS is an elastomeric polymer can be used in many applications, including fabricating microfluidic devices. It was first presented by George M. Whitesides as an alternative material for constructing micro-structure(16, 17). Once cured, PDMS becomes an elastic layer and replicates any mold structure. Compared to silicon and glass, PDMS is preferable in several ways. The elastic nature makes it more suitable for moving parts, for instance, micro-valves or flexible membranes. It is biocompatible, which can be utilized in cell analysis or 3D cell culture. PDMS is also a perfect option in rapid prototyping due to the low cost and fast fabrication. Other polymers like polymethylmethacrylate (PMMA) and polycarbonate (PC) are also used for fabrication through injection or 3D printing methods, but these materials only fit certain circumstances due to lack of resolution.

Silicon has the best fabrication resolution and can easily go down to nano-scale. The possibility to integrate microelectronics is highly desired in digital microfluidics. Glass has better transparency and mechanical strength. The hydrophilic surface also

benefits many biological applications. Despite the low cost and fast prototyping capability, PDMS has light scattering issue that affects fluorescence detection; extremely high electric resistivity and thermal resistivity may be not suitable for certain applications. Casting PDMS also has a limited resolution below micron scale. In brief, each fabrication material has its unique advantages and disadvantages; there is no one-for-all solution. We shall choose proper fabrication materials based on specific requirement.

1.2.2 Common fabrication techniques

Most microfabrication techniques originated from semiconductor industry in order to construct the microelectronic structure. Similar strategies have been developed and combined to build microfluidic devices.

1.2.2.1 Photolithography

Patterning substrates into 3D structures typically involves removing certain parts of the given materials. Photolithography was originally created to pattern silicon wafer in semiconductor industries but now has been widely applied to many microfabrication techniques. This technique can selectively expose the substrate, a photosensitive material called photoresist, through a printed mask to UV light. Based on the polarity of the photoresist, substrates exposed to UV light will solidify or degrade upon heat. Then the unstable photoresist is etched away by a solvent. Using photolithography, researchers are able to transfer 2D patterns to substrates, and by controlling the substrate thickness, the desired 3D structure will be built.

1.2.2.2 Surface coating

Microfabrication generally includes some surface coating steps in order to build thin layers of substrates atop the fabrication material. The coated layer can be a mold layer, for example, SU-8 used for PDMS mold; it can be a protective layer to prevent material from being etched, or it can serve as a sacrificing layer during multi-layer fabrication. Spin coating is the most commonly used method for convenient surface coating. There are a large number of coating solutions, like a spinner, that are commercially available. Spinning materials with different viscosities at given speed can produce a thickness varying from submicron up to hundreds micron. But uneven thickness, trapped air bubble are common issues caused by human error and may lead to fabrication defects. The spin coating also requires liquid form solution with certain viscosity, which is inapplicable to solid materials. For solid metal, a method called vapor deposition can coat a thin layer of metal onto substrates. Electron beam turns metal into vapor in a sealed chamber and lets vapor form a metal layer once hit substrate surface. However, this method requires special instruments to evaporate solid metal and takes a long time to grow micron size layers.

1.2.2.3 Etching

Etching is the fabrication step used to remove the unwanted substrate. It can be divided into two categories, dry etching and wet etching. Dry etching mainly uses gas formed etchant to react with substrates, for example, SF_6. For anisotropic etching, (means

only etch in certain directions), the high-speed electron beam can remove substrate in the desired direction without etching the surroundings. Note that combining these two methods can further accelerate the process. Laser etching is a relatively new technique for fabricating microfluidic devices(18). The automated laser system directly etched the glass or plastic materials into designed shape in minutes. But the resolution of devices is limited by system setup. In summary, dry etching works great to create high-aspect-ratio structures, like deep wells(19). On the other hand, wet etching uses reactive chemical solutions to attack substrates. Commonly used wet etchants, for example, hydrofluoric acid or KOH can penetrate the surface layer of a substrate and react. Note that many commercial photoresist developers are etchant specifically designed for photoresist. In general, compared to dry etching, wet etching has an easier setup and cheaper to process. Nevertheless, the evenness largely depends on etchant local concentration. Lacking anisotropic etching method may become an issue when high-aspect-ratio structure is wanted.

1.2.2.4 Soft lithography

Soft lithography is actually a subject under photolithography. It gets its name because it is a technique to fabricate elastic materials. There are a couple of ways to fabricate elastic materials like PDMS. The most frequently used strategy is casting, reported by Whitesides(20). Starting with master mold, which can be built by standard photolithography, we pour liquid state polymer into the mold and let it cure. Then the

cured polymer is peeled off and bonded to glass, shown in Figure 1-1C. The benefit of implying such method is that we can replicate many identical devices in a short time. It is highly desirable for rapid prototyping and does not require expensive equipment setup. Injection molding is the most popular method used under industrial setting for large scale production. Similar to casting, injection molding also requires a cavity as master mold, shown in Figure 1-1A. Melted polymer is injected into the mold under high pressure and allowed to cool down to room temperature. The entire process is well established and fully automated, allowing quick construction of microfluidic devices and reducing the labor requirements on producing line. However, injecting such high viscosity liquid into confined cavity does demand high pressure. As a result, injection molding is typically applied to fabricate millimeter scale device and above. Micron-scale devices generate too much resistance, thus become difficult to process. Another method for soft lithography is stereo-lithography, a fabrication technique using focused lasers to cure polymer in a certain place, Figure 1-1D. The process starts from the bottom and builds device layer by layer. The entire process is computer controlled which eliminates the mold or mask during fabrication. However, the equipment setup is too expensive for simple microfluidic fabrication. A similar approach applies to 3D printing, another fast prototyping tool for constructing microfluidic devices. But the preciseness largely depends on the printer resolution and typically limited to millimeter scale.

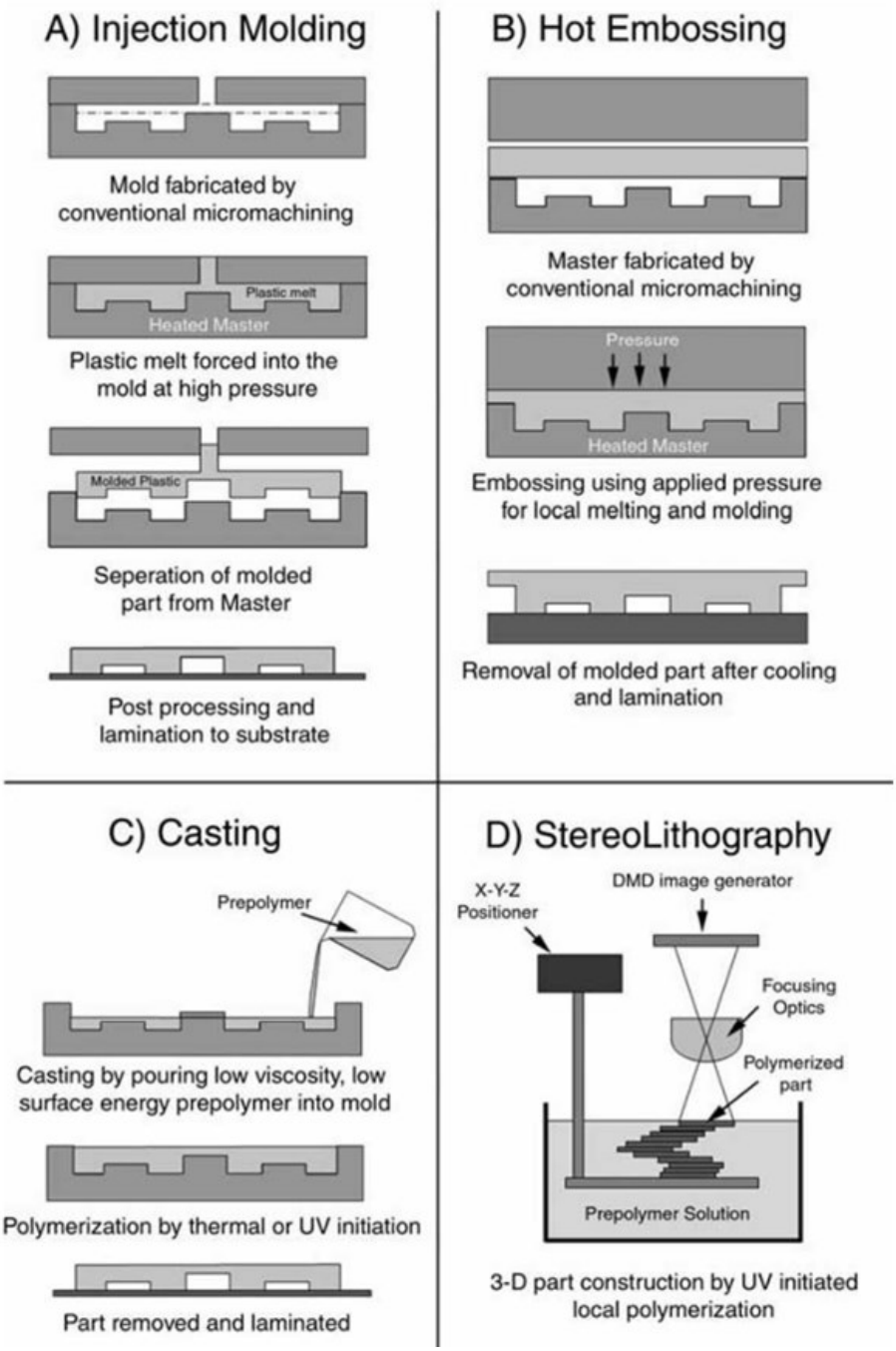

Figure 1-1. An illustration of common techniques for soft lithography. A) Injection molding B) Hot embossing C) Casting D) Stereo lithography. (15) [reprinted with permission]

1.3 On-chip sample preparation

To date, many microfluidic designs reported that optimized design could enhance the sensitivity of uTAS system or allow for faster operation. However, most published works were only focusing on improving the detection method of uTAS while the tested sample still required several pretreatments before loading in order to achieve such sensitivity. Thus, despite the fully automated sensing device, samples for uTAS remain low complexity and generally involve a series of benchtop process. The benchtop process usually consumes a sample volume that orders of magnitude large than the actual loading volume. It also takes longer time and requires more manual work that may introduce errors or contaminations. As a result, uTAS loses its own advantages such as low sample consumption and fast processing time.

A general strategy to overcome the sample preparation issue is integrating multiple components to the core sensor, which serves many purposes, including easier automation, shorter analyzing time, and fewer contaminations. Numerous sample preparation functions have been designed for on-chip sample processing.

1.3.1 On-chip sample separation/ purification

On-chip sample separation is a broad concept that includes sample purification, sorting, separation and clean up. The general purpose of on-chip separation is to remove unwanted components from loading sample in order to minimize fake results and signal interference. It is a necessary module for uTAS to achieve higher sensitivity and reliable

result, especially for raw sample analysis, for instance, whole blood(21) or water pollution sample(22). Many physic principles can be applied to sample separation. Most commonly, mass or density difference utilizes gravity to split sample mixture (23). But due to the low Reynolds number under uTAS setting, this separation technique typically needs a rotary design and centrifugal force. Size based separation is another popular strategy for uTAS. The parabolic flow profile in a micro channel can speed up large particles separating from the small ones (24). Alternatively, pinched flow fractionation works in a similar way to separate a mixture (25). Serving as a convenient tool, flow assisted separation gains its unique niche because the capability to separate sample mixture without additional force. However, the limitation is also obvious- separation really depends on a huge size difference and loses its efficiency when deals with nano-size particles or small molecules.

On the other hand, field based separation gains more attentions in favor of uTAS customized design. For example, electric field is the most frequently used field separator with huge potential to customize. The traditional electrophoresis separate sample mixture by the charge to mass ratio, called electrophoretic mobility (26). An upgraded version of on-chip electrophoresis is two-dimensional electrophoresis, which provides better separating resolution (27). Isoelectric focusing (IEF) serves to separate protein mixture based on their isoelectric point (28) and it is possible to further couple it with polyacrylamide gel electrophoresis (PAGE) for high throughput protein separation.

Isotachophoresis, a relatively new technique, drew huge attentions from biologist due to the capability of simultaneously sample separation and enrichment. Dielectrophoresis (DEP) is another powerful tool for manipulating samples because DEP incorporates frequency as an additional parameter, which enables polarization of neutral particles (29). But DEP force largely depends on dipole moment, thus can be rarely applied to proteins or other small molecules. Other fields have been explored for on-chip sample separation in the same time. Magnetic field is a very popular tool for separation with the possibility to integrate magnetic nano beads (30). Acoustic field also has been reported for on-chip separation, mainly restricted to large particles like silicon beads or cells (31). Temperature gradient created thermal field offers another possibility for analyte separation via thermal mobility difference(32). One issue associated with temperature gradient is sample stability. Biomolecules may denature or degrade under sharp temperature gradient if pursuing separation speed.

Meanwhile, traditional separation strategies have been scaled down for on-chip sample preparation, for example, solid phase extraction(SPE) or aqueous two-phase extraction(ATP). SPE originally serves as bench-top separation technique using bind-elute model. But it can be integrated into micro devices in a smaller scale for sample extraction, which is considered as sample clean up tools because only interested molecules can bind to the solid phase. On-chip SPE has been approved a useful tool for biological applications. Lander's group has reported several microfluidic designs with

integrated silicon beads for isolating DNA from protein inhibitors (33, 34). Harrisons group had demonstrated the capability to extract target fragment from protein digestion with on-chip SPE bed and coupled mass spectrum for detection (35, 36). ATP is an alternative system for extraction and separation. Unlike SPE, ATP system employs two immiscible fluids, typically polyethylene glycol (PEG) and dextran, and flow them next to each other. Reports have shown a great potential of ATP in bioseparation and liquid-liquid interface extraction (37, 38) due to the affinity difference for each molecule. With proper setup, target molecule with higher affinity to one phase tends to migrate across the interface while rest species remain in the original phase, thus achieve good separation.

Recent efforts have aimed at on-chip liquid chromatography with microfluidic designs. On-chip high performance liquid chromatography (HPLC) holds great potential to revolutionize many uTAS in several ways. While traditional HPLC features good separating resolution and robustness, the batch operation model really slows down the throughput. With parallel on-chip HPLC, multiple samples can be analyzed simultaneously with minute sample assumption(39, 40). Additionally, small volume allows easier integration with other detection methods, like mass spectrometry.

1.3.2 On-chip sample enrichment

During analysis of biological particles, as well as small molecules, under uTAS setting, a key feature that serves to expand the possible detection methods is sample

enrichment. All detection methods have their own detecting limits and many detecting options are inaccessible to diluted samples. Thus, a module can selectively concentrate target molecule is highly desired in order to achieve lower detection limits and allow additional detecting options.

There many on-chip sample preconcentration techniques, but a big part of it falls into the same category: electrophoresis. Field amplified sample stacking (FASS) is possibly the simplest preconcentration method utilizing the conductive difference between injected sample and background electrolyte. Lichtenberg et al reported a 65-fold improvement of signal magnitude during amino acid enrichment (41). But FASS requires injected sample must have a conductivity lower than the back ground electrolytes that may lead to additional sample dilution. Moving boundary stacking is another method to stack sample. It was first used to separate proteins from blood(42). The core physics behind moving boundary stacking is the ion difference between two sides of the interface that causes sample stacking and destacking when this interface migrates under the electric field. Another well-known sample enrichment method is isotachophoresis (ITP). ITP has been applied to both capillary and microfluidic based devices. Researchers reported that concentration of a variety of samples, for instance, bacteria, DNA and amino acid, with ITP technique (43-45). The reason that ITP is so popular for on-chip sample enrichment is the capability to concentrate target ions by several thousand-fold: Koenka et al reported 10,000-fold enrichment when purifying fish sperm DNA from the background (46).

During ITP, stacking is made possible by the presence of a leading and trailing electrolyte, also called terminating (LE and TE, respectively) in the system. Compared to target molecules, LE has higher electrophoretic mobility while TE has lower electrophoretic mobility. These two electrolytes migrate at different speeds and stack target molecules in the middle. Meanwhile, due to the conductivity difference, a secondary electric field is generated to further stack molecules near the interface. Isoelectric focusing is another powerful electrophoretic technique that serves both on-chip separation and preconcentration, especially for protein mixture. The design involves a pH gradient to adjust surface charge of target molecules. Each molecule in the sample has a dual ionic state in which it bears a point of neutral charge (pI). Molecules migrate under electric field until reach the neutral point and get stacked.

Meanwhile, non-electrophoretic enrichment strategies have been developed for on-chip sample preparation, for example, solid phase extraction(SPE) also serves as a sample enrichment tool due to a limited elute volume. Target molecule concentration can increase several folds as background molecules are washed away.

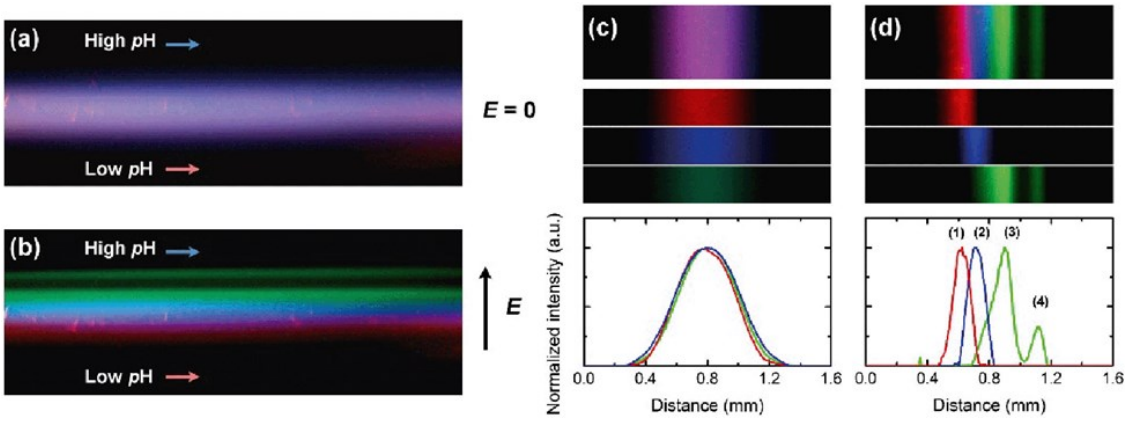

Figure 1-2. An example of isoelectric focusing of four different fluorophore-conjugated proteins. Fluorescence images at zero electric field (a) and 390 V cm^{-1} (b) show that the protein mixture focused into separated streamlines according to their pIs under the applied electric field. (c) and (d) present the corresponding fluorescence intensity profiles of the sample streams before and after separation, respectively. The numbers labelled on the separated peaks correspond to the fluorophore conjugated protein samples under test: (1) ovalbumin-Alexa 594 (pI 4.5–4.8, red), (2) neutravidin-Alexa 350 (pI ~6.3, blue), (3) wheat germ agglutinin-Alexa 488 (pI ~8.5, green) and (4) avidin-Alexa 488 (pI ~10, green). (47) [Reprinted with permission]

1.3.3 On-chip cell sorting

As whole samples are increasingly used in uTAS, on-chip cells sorting become more common with an aim to clean up undesired cells that that may impede detecting accuracy. Another main reason for cell sorting is to increase the concentration of a particular cell-type of interest, thus leads to a better detecting sensitivity. However, techniques that can process cell or bigger particles are quite different from those processing small molecules like protein and DNA. Many techniques originated from

small molecule area become inapplicable or less efficient due to the relatively large particle size. In the meantime, inertial force, shear stress and dielectrophoretic force become more effective when dealing with cell-based samples.

Cell and particles around micron size have a considerable volume and experience inertial force like gravity. This leads to the emergence of a large number of morphology-based sorting techniques that do not require external forces, also called passive sorting. Deterministic lateral displacement (DLD) provides a convenient way for sorting cells. The design contains arrays of micro-pillars such that cells smaller than a critical radius move freely through the pillars while cells larger than a critical radius move in a direction dictated by the arrays(48, 49). Similarly, micro-posts or other microarrays can work as micro-filters to separate cell mixture by size- small cells pass the micro-posts but large cells are trapped before entering the outlet(50, 51). Filtration can integrate cross flow or flow focusing as the secondary hydrodynamic force to facilitate cell sorting. Yobas group reported using cross flow and micro side arrays to separate small cells from the large ones (52, 53). Yamada et al also published several cell sorting designs with a secondary flow for hydrodynamic focusing(54, 55). In addition to the microstructures patterned inside flow channel, the inertial force also plays a critical role in size-based cell sorting. For example, Di Carlo et al reported a serpentine design that utilizes centrifugal force to lift and rearrange cell position by size difference (56). Similar idea with a spiral channel was also reported by and Russom et al(57). Meanwhile, pinched flow fractionation

applies a similar strategy to reorder position cells with inertial force (58, 59). Pinched flow fractionation occurs when a flow is pinched by a narrow channel such that all cells are pushed against the side wall and subsequently, due to the size variation, experience slightly different flow trajectory upon broadening of the channel. Thus, following the laminar flow profile, smaller cells align further from the center stream and separate from larger cells.

On the other hand, non-passive sorting techniques typically require an external force to initialize sorting. As described in the previous section, many external fields utilized for on-chip separation also work for cell sorting. Takahashi et al. reported a rapid electrostatic cell sorting device with integrated electrophoresis design (60). Puttaswamy et al. sorted cells with AC electroosmosis coupled with negative DEP force(61). Acoustic force also started to be employed in microfluidic designs as it offers a new strategy for on-chip sample separation, including cells(62). Adams et al. developed a multiplexed cell sorting device using magnetic field such that cells labeled with magnetic beads can be isolated from cell mixture(63). DEP force, a technique may not be suitable for small molecule separation, becomes a very powerful tool for cell or particle sorting because of the large dipole moment. For example, Wang et al. published a microdevice with embedded interdigitated electrodes that provide repulsive forces to organize cells by negative DEP(64).

1.4 Essential modules for on-chip sample preparation

Without modular integration, a completed on-chip analysis typically involves several sample transfer operations from one module to another. These sample transfer methods require conventional pipetting or manual collecting, which obviously degrades most of the advantages associated with the microchip. The actual lab-on-a-chip idea will not be fully realized without system integration. There are several reasons that researcher particularly interested in uTAS modular system integration. First, a fully integrated system can reduce necessary sample exposure to the environment such that preventing possible contamination. Besides, taking advantages of automation, integrated uTAS can collect reliable results by avoiding human operation errors. Another main reason for modular integration is to speed up the overall analysis by streaming required functions on a single chip. To further modular integration, Krisna et al. reported a polymer-based design with discrete 3D modules that allows quick assemble of desired chip functions(65). This stands for the new trend of modular integration: fast, simple and easy to use. However, completed integration of different modules will further complicate chip design and requires numerous troubleshooting, for example, micropumps that drive fluids, micro injectors for creating sample plugs, sensors that monitor flow and pressure information etc.

1.4.1 Micropumps

In order to make fluid transportation possible in a micro device, a certain driving force has to be implemented. Utilizing passive transportation mechanism that takes advantage of surface tension may be a straightforward strategy(66, 67). However, for uTAS with complex flow networks, the resulting hydrodynamic resistance requires more powerful mechanisms to remain continues fluid motion, such as pumps, pressure or vacuum. As traditional macro pumps are too bulky to be considered as portable, an on-chip active micropump with adequate pumping capability is highly desirable for uTAS.

We can largely divide current micropumps into two categories, a displacement pump and dynamic pump(68). Displacement pumps typically involve a moving part like rotor, piston or diaphragm and operate in a periodic manner which results in net fluid motion. Piston is widely employed in macro pumps rather than micropumps because mechanically constructing piston inside microfluidic channel is very challenging. Thus, instead of a mechanical piston, designs utilizing liquid phase piston, like ferrofluidic pistons, offer an alternative for piston micropump(69, 70). Rotary pump, on the other hand, applies a similar mechanism as piston pump by replacing piston with rotary gears. Dopper et al and other groups reported a couple of rotary pump designs powered by magnetic or electrostatic force(71). However, due to the large size of rotary gears, the true nature of the microfluidic device is greatly impeded, thus only a few rotary pump design have been actually implemented onto microchips. Most displacement pumps are

diaphragm-based reciprocating pumps, shown in Figure 1-3: a design features a deformable surface or membrane, an actuator with different driving mechanisms and a flow chamber with check valves. This serves as a basic design for diaphragm-based reciprocating pumps, which was first demonstrated by Harald van Lintel and coworkers((72). Later on, other micropump designs adapted from Lintel's were reported. Several groups have reported nozzle-diffuser structure to replace check valves and a maximum flow rate of 16ml/min was achieved with water as working fluid(73, 74). The driving mechanism also diversified from pure piezo-driven due to the extensively implementing of the electric field and thermal field in microfluidic devices(75-78). Other less common pump designs, like phase change pump(79), multiple-valve-based pump(80), electromagnetic pump(81) have been reported as well.

The dynamic pump continuously adds kinetic energy to the working fluid through external forces. The build-up of kinetic energy directly leads to momentum increases, such as centrifugal pumps, or pressure increases, like electroosmotic pumps. Centrifugal pump is a type of pump that developed long time ago utilizing centrifugal force to drive work fluid. Although many miniature centrifugal pumps are developed for certain biological applications (82), uTAS designs with such kind of pump are limited by its scaling capability and low efficiency. Electro-hydrodynamic micropump can exert an electrostatic force on ions in dielectric fluids. By sequentially activating electrodes arrays, electrohydrodynamic pump generates space charge across dielectric fluids and result in

net flow motion. The three mechanisms of charge generation are known as induction(11), conduction(83) and injection(84). Electroosmotic (EO) pump is a well-known dynamic pump with capability for high-pressure output. When the solid material is exposed to a liquid, negative charges spontaneously build up at solid surface and attract counter-ions from bulk fluid. This ions accumulation is described as the electrical double layer. The counter-ions in bulk fluid experience electrostatic force under a parallel electric field and set in motion such that dragging bulk fluid in the same direction. The simplest EO pump is fabricated from capillary tubes with two electrodes submerged at both ends. It features a significant pumping pressure and very limited flow rate(85, 86). To improve the maximum flow output, a porous structure was fabricated into capillaries and each pore serves as a small capillary(87). Chen and Santiago explored an alternative design with a narrow slot and achieved a maximum flow rate of 15 ul/min at 1kV(88). EO pumps using AC field was also reported (89) with the efforts to avoid the common issues in DC EO pumps, such as Faradic reaction. A few designs with external forces other than electric force were also published, for example, magnetic field(90), ultrasound(91) and thermal transpiration(92) etc.

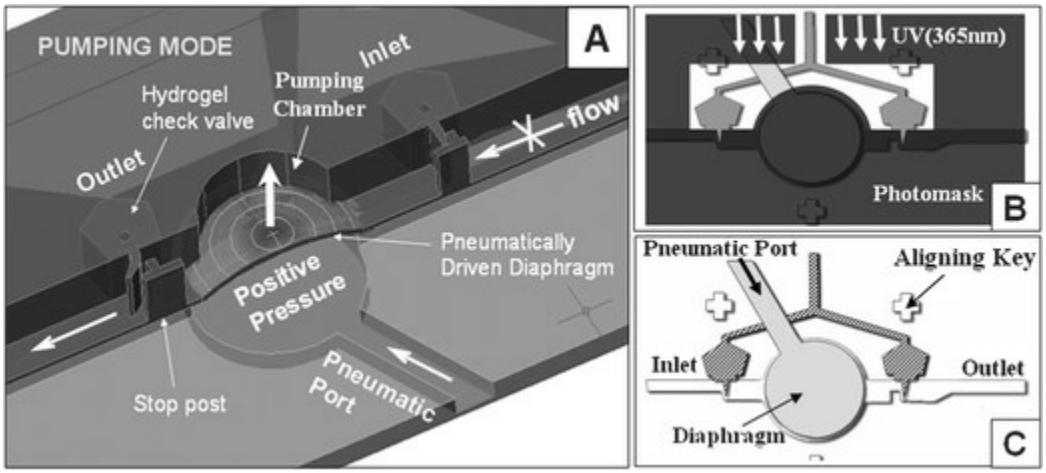

Figure 1-3. (A) The 3-D schematic view of the pumping system (the top is covered with cover glass); (B) Schematic diagram of alignment of photomask and UV radiation into the PDMS platform; the monomer solution was injected, and the photomask was aligned through use of an aligning key; (C) After, UV radiation, the unpolymerized monomer solution was rinsed, and the polymerized region (dashed area) remained. (93) [reprinted with permission]

1.4.2 On-chip sample injector

While most bench-top analytical equipment requires manual sample loading with pipettes, uTAS typically involves a series of on-chip fluid manipulation to create sample plugs for following separation or detection modules, such as capillary electrophoresis or PCR. One big advantage of uTAS is the possibility to integrate sample injection module and accomplish automatically injection. Due to the small channel dimension and short analyzing time, sample plug variation will be significantly enlarged and causes unstable results. Thus, reproducible sample introduction becomes a key factor to acquire reliable analysis. In the meantime, short sample plugs are higher desired in order to speed up

analysis and improve sensitivity. Although researchers presented many sample injection designs, these techniques can be mainly divided into two categories: Electrokinetic injection and pressure injection.

Electrokinetic injection is the most common used sample injection mechanism, shown in Figure 1-4. It has the superiority in shaping sample plugs based on cross section design while pressure injection cannot. Two fluid streams are electrokinetically controlled and cut into each other to generated small sample plugs. Several channel designs have been reported to facilitate plug generation. Harrison et al(94) reported a T shape design for sample injection (Figure 1-4). Later, updated versions with double-T and cross-T devices were published by Effenhauser et al and Jacobson et al (95, 96). In Jacobson's work, they also demonstrated the floating injection technique, a technique taking advantage of the special flow profile of EO flow to minimize sample tailing, which is a common issue in pressure injection. Other less common designs like pinched injection and gate injection were also reported (97, 98). An issue associated with electrokinetic injection is the injection bias. Anionic, neutral and cationic analytes have different electrophoretic mobility. This difference may lead to changes of sample composition and unreliable results. Another problem mentioned during electrokinetic injection is sample leaking. Due to a purely EOF-driven mechanism, sample stream that floats near the cross section may diffuse into the buffer channel and causes peak noise in capillary electrophoresis.

Pressure injection, on the contrary, does not experience these issues. Pressure injection is based on the hydrophobicity and wettability of channel surface. Sample plug is generated by alternatively pulsing two streams with the pressure source(99, 100). Backofen et al also reported similar design with hydrodynamic injection(101). However, the biggest issue for pressure injection is the tailing effect caused by parabolic flow. Sample plugs created from pressure injection generally have long tails on both sides that may interference with peak analysis. The pressure injection module also suffers portability issue as external pressure source or pumps are required to operate periodically.

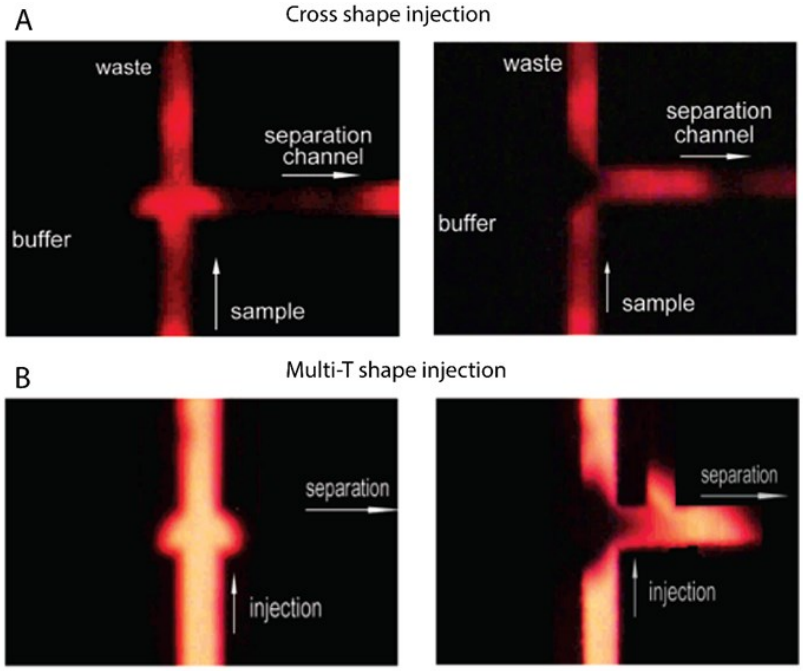

Figure 1-4. Demonstration of sample injection models. A) Cross shape injection channel and B) multiple-T channel injection. (102) [Reprinted with permission]

1.4.3 Microsensors for flow monitoring

As a consequence of the increased demands of automation and precise control in uTAS, microsensors that pick up a variety of physical signals and convert to readable data draw great attentions in the past decades. When detection volume scales down to microliters under uTAS setting, researchers expect much higher sensitivity and reliability of microsensors compared to traditional sensors. In the meantime, other integrated uTAS modules may impede microsensor performance by introducing additional interferences, which makes integration of microsensors one of the most challenging fields in uTAS. Based on the general purposes, microsensors can be classified as physical sensors, chemical sensors and biological sensors. For flow monitoring modules in uTAS, most modules fall into the physical sensor category, which is briefly introduced here. Chemical and biological sensors are not covered here.

As a primary driving force of microfluidic devices, pressure serves a very important role to deliver flow velocity and parabolic flow profile, a flow pattern required for many hydrodynamic separation mechanisms. The earliest effort to monitoring pressure information is the pressure gauge, but even the smallest gauge is orders of magnitude larger than microfluidic channels and impossible to be embedded onto a microchip. Currently, most on-chip pressure sensors utilize piezoresistive-based transistor, a transistor that relies on pressure induced electric property changes. This type of sensors typically involves an elastic structure such as a thin membrane(103), or soft beads(104).

Pressure causes deformation of elastic materials and alters their resistance. This resistance variation is linear related to pressure changes thus can measure local pressure after calibration. Similar strategies can be applied to the elastic chamber filled with conductive electrolyte(105). The pressure-induced distortion of the flexible chamber leads to conductance difference and variation in the electrical signal. Yukimitsu et al. reported a similar sensor design with separated diaphragms that converts pressure data to capacitance information(106).

Correlated to pressure sensors, flow sensor plays an important role in monitoring flow rate and providing feedback control. Flow sensors with sensitivity down to nanoliter are already commercially available. However, the size of commercial flow meter is typically much larger than microfluidic chips, which makes it impossible to measure local flow rate inside a microfluidic network. Many types of microfluidic flow sensors came into light in the past decades. Time-of-flight technique has a sensor with two separated sets of electrodes that can detect conductivity difference inside flow channel. The time gap between two conductivity changes can be used to calculate flow velocity(107). Heat transfer is the most common technique utilized in flow sensor design due to the capability to measure a flow rate down to nanoliter. Ferenc et al(108) report a flow sensor contains a center heat source with two thermal meters on both sides. This design takes advantage of heat convection caused by flow motion such that temperature difference between two meters can be measured to calculate flow rate. Mechanical flow

sensor is also available for microfluidic devices. For example, Wang et al. reported a cantilever flow sensor that correlates flow rate to microbeam deflection. But mechanical sensor quickly loses its accuracy when working fluid contains dust or other impurities that may affect deflection. Particle tracing is another frequently used strategy for flow measurement(109). Adding micro beads and tracking bead movement with high speed camera allows to measure linear velocity of the working fluid. However, requiring optical detection and post image processing clearly limits its portability and data acquiring speed. Additionally, ultrasonic and optical also haven been integrated with flow sensing by other groups and achieved good sensing accuracy(90, 110).

1.5 Thesis Overview

This thesis seeks to address the on-chip sample preparation issue in two aspects, continuity and integration, which represent two main challenges of on-chip sample preparation. Lacking of modular devices that can perform sample preparation in a continuous manner is a big obstacle for realizing the uTAS concept because sample collection or fractionation is required after each sample preparation module, thus, greatly undermines the processing time. Additional sample collection may also introduce contamination during sample transfer and risk the reliability of later detection. The second challenge is lacking of necessary on-chip flow control modules that can facilitate module connection and automation. In this thesis, the multifunctionality challenge is solved by developing a new membrane-based electrokinetic platform with capability to

realize multiple on-chip sample preparation techniques. This platform not only delivers uniformed three-dimensional electric field into microfluidic channels in an effective manner, also has superiorities in fabrication, portability and cost aspects. Meanwhile, multifunctioning capability was demonstrated by realizing two common on-chip sample processing techniques: parallel separation and enrichment. On the other hand, the second challenge is tackled by creating on-chip flow control modules that are essential for flow control. The new designed platform, once again, was transformed into several fluid control modules, including micro-pump, sample injector, fluid controller and flow sensor. More importantly, all these on-chip modules can be directly integrated into any sample processing modules without changing the original designs. In other words, researchers can easily integrate possible sample processing modules as needed while still allowed customizing each module function.

In the first chapter, a general background correlated to my research work was provided while addressing the two big challenges of on-chip sample preparation. This leads to Chapter 2, where I summarized the current microfluidic designs for electrokinetic applications and proposed new membrane structure. A simple electrocurrent model followed to demonstrate its working mechanism and characterize performance efficiency. An extensive comparison between this new platform and other reported devices then reviewed the advantages and drawbacks of this platform. In the end, I presented a detailed fabrication process for building this membrane structure. Then the

thesis splits into two parallel blocks, the module integration block and multi-functional block, which corresponding to the two obstacles mentioned previously. The first block is chapter 3. Two sample processing modules, charged molecule separation and enrichment are presented here. Chapters 3-5 stand for the second block, where micro electro-osmotic pump, fluid control and sample injection, micro flow sensor, will be demonstrated, respectively. In the last chapter, I will summarize all my previous research work and sketch the big picture of on-chip sample preparation with this newly created platform. The results shall provide guidelines and inspirations for future on-chip sample preparation research.

2 A New Platform Using Carbon Black Nano-composite PDMS Sidewall Membranes for Electrokinetic Applications

2.1 Overview

We present a new type of microfluidic device for on-chip electrokinetic applications. The new design consists of metal gallium electrodes, which are isolated from a main microfluidic channel using thin micron-scale polydimethylsiloxane/carbon black (PDMS/CB) composite membranes integrated directly into the sidewalls of the microfluidic channel. The thin membrane not only allows for better electric field penetration and uniform 3D field, also serves to prevent electrode degradation and electro-thermal flow near electrodes surface. Due to the small size and simple fabrication procedure, this PDMS/CB platform could be used as part of an on-chip upstream sample preparation toolkit for portable microfluidic diagnostic applications. We provide a comprehensive review of current designs that are involved in on-chip electrokinetic applications in order to demonstrate the benefits and drawbacks of this new proposed design. A detailed step process is also presented to show the device fabrication.

2.2 Background

Many electrophoretic methods are capable of performing preparative sample processing, such as preconcentration, mixing or separation. Among these techniques using electric field, free flow electrophoresis (FFE) holds a unique niche due to its

capability of continuously sample processing. In FFE, instead of applying an electric field parallel to flow direction, electric field perpendicularly travels across the sample stream. The field drives charged molecules in solution to electrophoretically migrate across the channel at a velocity based on their size and electric charge, known as electrophoretic separation. Separation and collection steps are performed continuously in FFE, making it an attractive candidate for high throughput sample processing. FFE, for example, can continuously isolate cellular components, proteins, peptides and enzymes from complex mixtures. But applications of FFE concept are not limited to electrophoretic separation. Many essential sample preparation techniques are evolved from basic FFE separation, such as isotachophoresis(111), isoelectric focusing(112) and dielectrophoresis(113). All these techniques are capable of manipulating small molecules or large particles by inducing electric field into flow channels.

Despite significant research and development, current methods for delivering electric field into microfluidic device still have several limitations. Because the electric field can often produce a high current in the electrolyte solution, electrokinetic systems often suffer from Joule heating, bubble generation, and unwanted electro-thermal flow, which can lead to several issues, for example, low detecting resolution, protein unfolding or flow distortion. Besides, current microfluidic devices employing electric field, however, are bulky, difficult to fabricate and can suffer from stability issue, which can limit their portability and molecular separation efficiency.

2.3 On-chip electric field delivery

Approaches have been reported in literature seeking to introduce electric field into microfluidic channels. To alleviate the challenges associated with using electric field, a membrane-liked structure is fabricated into microfluidic devices. The membrane structure serves to isolate electrodes from directly contacting with working fluid thus to prevent electro-thermal flow, cross contamination, and bubble generation. For designing membrane structures, generally, three aspects are thereby of main importance: a) capability to minimize bubble formation or other undesired side products caused by Faradic and other surface reactions; b) isolating electrodes from working fluid to avoid electrode degradation as well as preventing sample cross contamination introduced by electrode channels; c) delivering a stable electric field in an efficient manner, where efficiency is defined as effective voltage across the channel over total voltage applied. Different approaches have been published trying to fulfill the criteria mentioned above. Based on the membrane structure, we can roughly classify current designs into the following categories: 1) Micro side channel arrays serve as a membrane-like structure to isolate electrode channels. 2) Conductive polymer seals electrodes from main flow channels. 3) Mechanical insulator based membrane. 4) Directly integrated electrode without membrane structures. 5) Channel depth isolation. For each category, researchers developed additional electrode designs in order to further address some issues related to applying the electric field.

2.3.1 Direct integrated electrode design

The easiest strategy for delivering electric field is integrating electrode directly into the flow channel. Electrode utilized here is typically metal based, which allow easy setup and does not require additional flow control(114). The biggest obstacle of using such design is gas formation caused by direct contact between the metal surface and working fluid. One method is to simply reduce the voltage applied to the electrodes inside the flow channel to avoid buffer electrolysis. While effective, this places limits on efficiency due to the low electric field strength. Besides, diffusion becomes more significant under small flow rate, which adds additional time for sample processing. The reported (115) residence time can go up to several minutes before a good separation is achieved.

2.3.2 Micro side channel arrays

The earliest method trying to isolate electrode from working fluid is the micro side channel design, shown in Figure 2-1. The side channel arrays contain a series of micron size channels that can provide large flow resistance, such that samples in the flow chamber turn to not entering the side channel. In the meantime, this hydrodynamic resistance also serves to prevent air bubbles from entering the main flow channel. Micro side channel array design commonly uses liquid electrodes with continuously refreshed electrolyte to remove generated gas bubbles. Electrode channels in this design can either be sealed or remain open. Zhang and Manz reported a micro side channel device with

open electrode channels(116)) Open electrode channel allows for easy ventilation and higher electrolyte refreshing rate. Raymond et al demonstrated a uTAS device with closed liquid electrodes, which can be fabricated by a single etching step(117). However, the micro side channels also possess a large electric resistance and significantly reduce chip efficiency. According to the estimation, more than 95% of applied voltage is lost across side channel arrays. Another significant issue associated with side channel is fluid leakage. Although high flow resistance serves to prevent cross flow, electrolyte does leak into main flow channel when a pressure gradient is built up, especially for closed electrode channel. Besides, setting up a pH gradient under the presence of side channel is very difficult, which makes it unlikely to be applied in IEF.

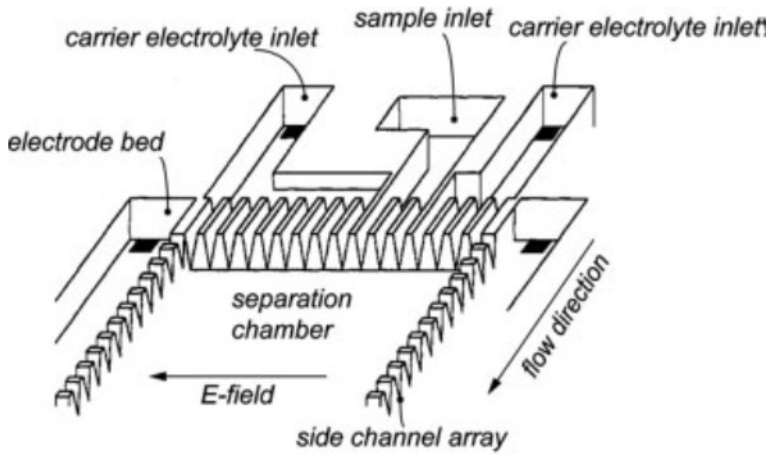

Figure 2-1. A micro side channel array reported by Raymond. (117)[reprinted with permission]

2.3.3 Mechanical insulator membrane

Using insulator as membrane structure is a new angle to address electric field delivery. The electric field is generated by electrostatic induction, proposed by Janasek and co-workers(118). The idea of this device is similar to an ideal DC capacitor, shown in Figure 2-2, where the charge is introduced by ion rearrangement. After sufficient charging time, an electric field will present inside flow channel due to the accumulation of opposite charges on sidewalls(119). The approximate efficiency reported by the author is around 50%. However, the potential screening effect, a phenomenon caused by attracting counter ions to the solid surface and neutralizing surface charge, is not clearly explained. According to our experiment observation, most electrostatic induced surface charges will be neutralized by counter ions in bulk fluid, thus the net electric field becomes zero inside a flow channel. This charge balance only breaks when both a high voltage and low conductive fluid are applied. In that case, bulk fluid does not have enough counter ions to shield surface charge such that an electric field can be observed.

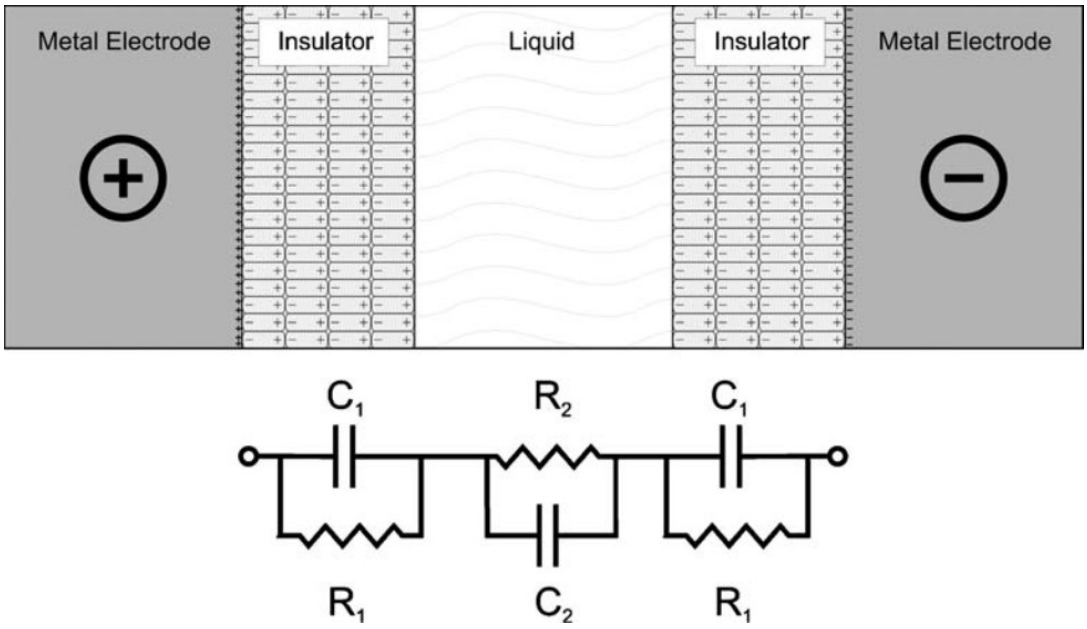

Figure 2-2. A figure of electrostatic induction device illustrating the principle of charge displacement and dipole orientation. Lower panel: equivalent circuit diagram. Copy right from Royal Society of Chemistry.(118) [reprinted with permission]

2.3.4 Chanel depth isolation

Very similar to micro side channel design, Fonslow et al. and Kobayashi et al. (120, 121) proposed to use channel depth variation to isolate electrode bed instead of channel arrays. The idea utilizes high flow resistance created by shallow channel dimension to prevent gas from getting into the main channel and then flushes bubble away with electrolyte. This design successfully increases the chip efficiency to 90%, which is much higher than micro side channel design. Channel depth variation can be achieved by minimizing main flow chamber's height or fabricating shallow banks between electrode bed and main channel. Neither method reported buffer electrolysis problem. However, the drawbacks for such type of design are obvious. Depth variation

not only requires multiple fabrication steps, also a more complex buffer pump scheme, which undermines its portability.

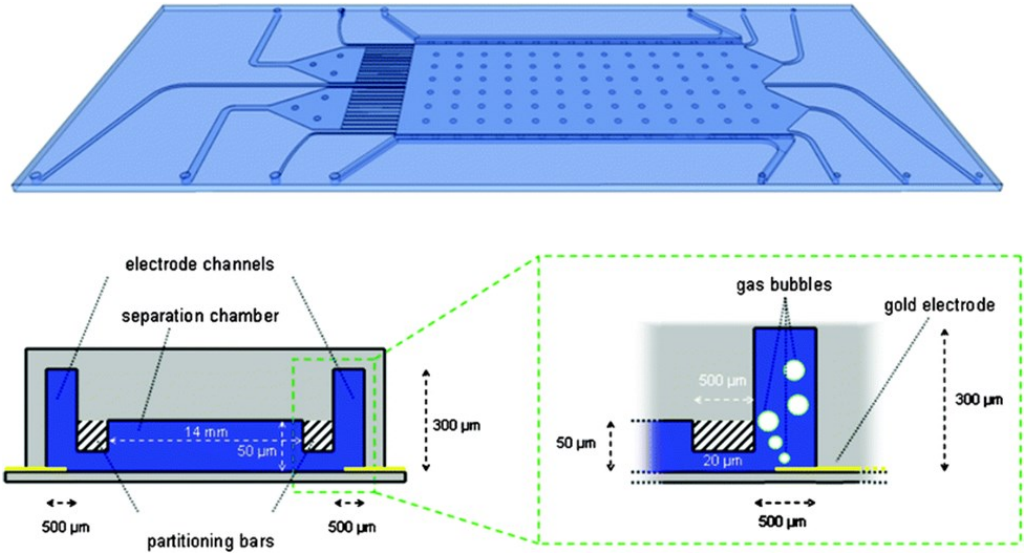

Figure 2-3. Chip layout and cross-sectional diagram of the separation chamber with depth isolation. Gas bubbles retention through electrode channel(122) [reprinted with permission]

2.3.5 Conductive polymer membrane

Gels made from cross-linked acrylamide monomer can be integrated as conductive membranes for delivering electric field, known as the salt bridge. Kohlheyer et al.(123) presented a device with photopolymerized acrylamide membranes, offered chip efficiency around 50%. Other materials like PDMS or laser printed glass have been demonstrated with embedded acrylamide membranes as well(124, 125), however, one issue associated it is the mechanical stability. Gel based membranes suffer from poor mechanical stability under high pressure or dehydration. Photo patterning of selected

region also leads to additional photolithography steps. Recently, Song et al. reported the ability to tune the electrical conductivity of sidewall membranes using microbeads (126). This method was successful in producing stable electric field while remain tunable, but requires significant fabrication and is currently not capable of being mass produced for wide scale use.

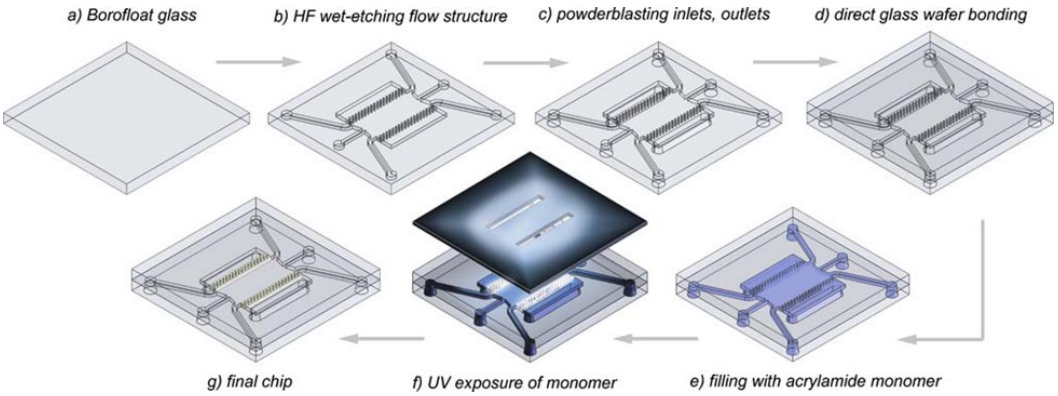

Figure 2-4. Fabrication process of photo-patterned ion-exchange membranes designed by Kohlheyer et al. Copy right the Royal Society of Chemistry.(123) [reprinted with permission]

2.4 A new conductive PDMS membrane for electric field delivery

In this thesis, we proposed a new microfluidic platform for performing on-chip electrokinetic applications. Like conventional methods we introduced above, the strategy described here uses electrodes integrated within a separation channel to deliver an electric field into the flow channel. Unlike other methods, however, we uses electrically conductive PDMS with mixed carbon power (PDMS/CB) as membranes to isolate

electrodes from the analyte stream. The membranes are activated using adjoining electrodes fabricated from gallium metal. The combined CB/PDMS-gallium system is simple to fabricate and can deliver a stable and uniform direct current (DC) electric field across the channel.

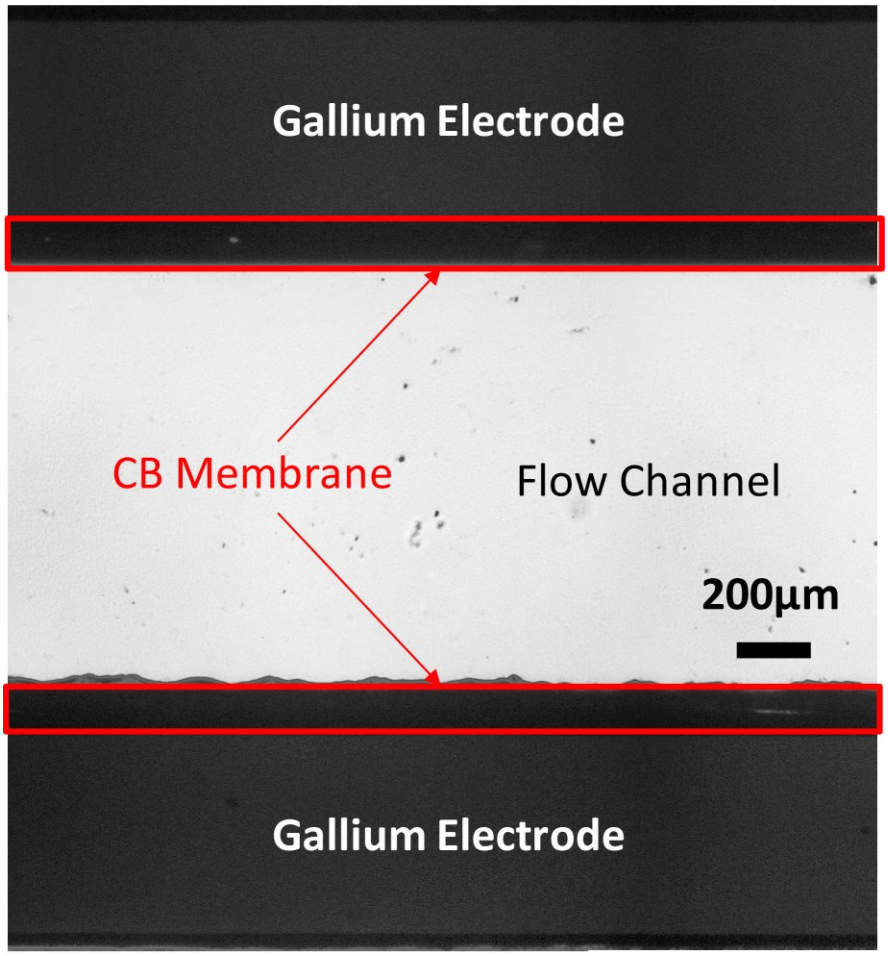

Figure 2-5. A bright field image shows the platform design. Two gallium electrodes were fabricated in parallel next to the main flow channel to deliver electric field into the flow channel. The sidewalls of the main flow channel were replaced with carbon-PDMS membrane and isolate metal gallium from contacting with working fluids. The membrane thickness can vary from 20um to 100um, depending on the required mechanical strength.

Note that increasing membrane thickness will lead to higher resistance and lower chip efficiency.

In order to demonstrate the benefits and drawbacks of this new design, we first performed experiments to determine if PDMS/CB membranes with adjacent gallium electrodes improve the performance by compared to systems without these features. Gallium is a low melting point metal that is capable of being injected into a microfluidic channel in liquid form and solidified to create 3D electrode structures. A major issue associated with solid metal electrodes is the surface reactions occurring at the electrode-buffer interface can generate gas bubbles, disturb the flow streams, and lead to an unstable electric field. Reactions can also lead to electrode corrosion and further sample contamination. Thus, FFE devices with solid metal electrodes are typically limited to the low conductive buffers and small voltages.

To determine if PDMS/CB membrane can minimize undesired surface reactions, we further characterized system performance using cyclic voltammetry (CV), a common technique utilized in battery and other electrochemical systems study. During CV study, electrochemical station applies an oscillating potential within the setting range meanwhile records the corresponding current. Without surface reactions, applied potential and current remain linear with constant system resistance. Any type of surface reactions can change overall resistance and result in non-linear CV curves. Surface reactions can be also detected by current variation under same voltage, showing a gap between two CV

curves. Typical electrochemistry study requires three electrodes, a working electrode, a counter electrode and a reference electrode. For current device design, we combined counter, reference electrodes, and built a two electrodes system. We performed CV study both on contact metal electrode design and the carbon membrane design in order to determine if carbon membrane is able to minimize surface reactions. For contact metal electrode design, both gold and gallium as electrode materials were tested. Applied potential range is assigned from -1V to +1V with start point at 0V, which means the applied voltage will ramp up to +1V from 0V, and decrease to -1V, then return to 0V. The corresponding CV curves of gallium and gold are shown in Figure 2-6(a), with gallium electrode colored in green and gold electrode color in blue. For gallium electrodes directly contact with working fluid, current scaled linearly within a voltage of first 0.5V, then started an exponential growth with increasing voltage. During voltage decreasing, significant current variations were observed, representing surface reaction has changed electrode conditions. The second half cycle of gallium electrode CV showed another type of surface reaction occurred when a negative voltage was applied because the current increased logarithmically with voltage instead of exponentially and a much lower current was reached. For gold electrodes with direct contact design, the non-linear relation was once again observed from 0.5V to 1V, meaning surface reactions started to occur around 0.5V. Unlike the gallium electrode system, the second half cycle of gold electrode CV curve is symmetrical to the first half. One possible explanation for this phenomenon is the reaction type happened near two gold electrodes surfaces are same.

The overall current variations are smaller than gallium system, which means reactions near the gold surface are not as strong as gallium surface. This observation also agrees with the metal redox potential, a parameter characterizes metal's tendency to lose electrons. Figure 2-6(a) also plots the CV curve acquired with carbon-PDMS membrane design, shown in red. In this case, carbon-PDMS membrane serves as a secondary electrode next to gallium metal. It transfers electrons like other electrodes but possesses much a higher resistance than metallic materials. Thus, the current level recorded in Figure 2-6(a) is almost zero compared to gallium or gold electrodes. We need to increase the current level to a similar range by applying a higher voltage to compare the actual performance of carbon-PDMS membrane to other designs, shown in Figure 2-6(b). We achieved a similar current range when 10V was applied to the carbon-PDMS system. Two CV curves collapse to one demonstrating the resistance of the system remains unchanged, in other words, no surface reactions have happened. We believe carbon-PDMS membrane maintains the inert nature of carbon and PDMS, unlikely to react with bulk fluid, thus reduce the possibility of surface reactions. One issue worth noting is the non-linear relation observed in carbon-PDMS CV curve. Although no surface reactions were detected, but the current pass through the carbon-PDMS membrane does not rise linearly as we expected. We assume this nano-composite polymer material behaves slight differently than normal conductive metal, which need further investigation to determine the actual mechanism.

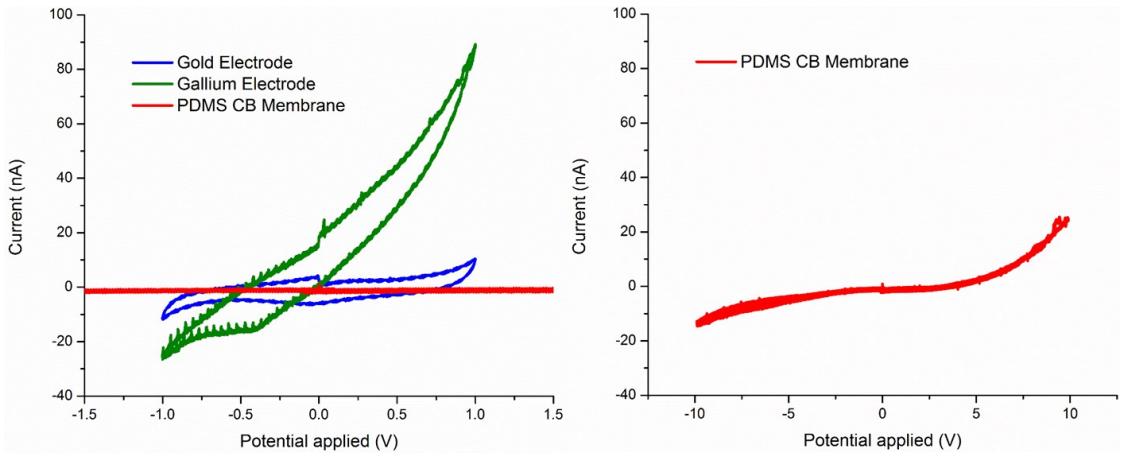

Figure 2-6. Detect surface reactions with cyclic voltammetry. The left graph shows CV studies of three electrode materials under a same potential range. All three electrodes directly contact with 1X PBS, which serves as a working fluid. CV curves continuously record current with given voltages. Current variations under the same potential indicate if any surface reactions occur and how much the system is altered by surface reactions. Green curve, represents gallium electrode, has the biggest current variation, meaning the strongest surface reactions. Followed by blue curve (gold), and red curve (carbon-PDMS). Current under carbon-PDMS setting was significantly reduced in this voltage range. Right graph) A higher potential was applied to the carbon-PDMS system in order to raise current to a comparable level. No current variation was detected under similar current range, which proved the inert electrochemical property of the carbon-PDMS material.

We proved adding carbon-PDMS membrane does minimize undesired surface reactions. To evaluate its actual performance during electrokinetic applications, we performed the free flow electrophoresis experiments with three different types of microfluidic devices: (1) a device without sidewall PDMS membranes, which represents the direct integrated design (2) a device with PDMS sidewall membranes but no carbon powders, representing the insulator-based design and (3) a device with PDMS sidewall

membranes and carbon powder. We conducted basic free flow electrophoresis (FFE) separation experiments here in order to determine the effective electric field. For each of these experiments we flow-focused a fluorescent sample stream in the center of the microchannel and then an electric field perpendicular to the flow stream was applied. Fluorescent molecules experienced electrostatic force and start to separate. Thus, we evaluated how electrode design can impact device stability and efficiency. Note that only solid electrode designs were considered during this study for the sake of pursuing good portability.

We first used a device with integrated gallium electrodes separated by micro channel arrays, shown in Figure 2-7A. The microchannel arrays provide hydrodynamic resistance in order to prevent gallium from flowing into the main chamber during fabrication. To perform free flow electrophoresis separation, HEPES buffer with an electrical conductivity of 120μS/cm and sample mixture of two fluorescent marker were directed into the chip through device inlets. When a 30V was applied to the electrodes, gallium began react with the buffer and electrode degradation was clearly observed Figure 2-7(A1). Electro-thermal flow was also noticeable near electrodes, which lead to non-linear flow profile. Meanwhile, another big issue associated was the Faradaic reaction that produced gas bubbles. When we replaced HEPES with high conductivity PBS buffer (16mS/cm) under the same voltage, a significant amount of gas bubbles were generated and blocked the entire flow chamber Figure 2-7(A2). Next, we investigated the

influence of a 100μm wide PDMS membrane integrated between the gallium electrodes and the main flow channel Figure 2-7(B). No electro-thermal flow or buffer electrolysis was observed for voltages below 1800V Figure 2-7(B1). However, the fluorescent sample stream remained at the same position when the electric field was on, demonstrating that the field strength inside the separation channel was not strong enough to produce effective FFE separation Figure 2-7(B2). We attribute this to the extremely large resistivity of the PDMS membrane, which can go up to 10^13 Ωcm. To overcome the high resistive nature of PDMS, we investigated the influence of carbon black nano-powder patterned into PDMS Figure 2-7(C). A voltage of 80V was applied across the electrodes and we observed effective separation of the two fluorescent dyes Figure 2-7(C1) without any observable electro-thermal flow or bubble generation Figure 2-7(C2). In comparing all three demonstrated designs, the PDMS/CBs membranes prevent electrode surface reaction while delivering a sufficient electric field for FFE. Based on our experiments, we can subject the current PDMS/CBs design up to 160V-200V without producing Faradaic reactions, which is a significant improvement compared to the direct-contact design. Furthermore, in case that stronger electric field is necessary, adding quinhydrone, an oxidization-reduction chemical couple that can adsorb extra free electrons, can bring the maximum applied voltage to 320V- 400V with a stable electric field. The chip efficiency was calculated as we previously described. Briefly, we filled up the main fluid channel with deionized water(DI), which conductivity was measured to be 1μS/cm with a conductivity meter. A high range ohmmeter(AlphaLab, Inc, UT)

connected to both sides of the electrode channels can measure the total resistance between two gallium electrode. We described a simple electro current model to characterize the electric properties of this device. We established an analogue to represents the electrical setup we used to determine the resistance of PDMS/CB membrane. Resistance of gallium electrodes can be ignored because of the good conductance. Rest parts, two PDMS/CB membranes and bulk fluid in flow chamber, are treated as resistors in series. We can simply calculate the resistance of bulk fluid using equation.1,

$$R = \rho \frac{L}{A} \quad \text{Eq.1}$$

where ρ is the resistivity of deionized water, L is the width of fluid chamber and A is the contact surface area of PDMS/CB and bulk fluid. We determined deionized water resistivity by taking inverse of the measured conductivity (σ).

$$\rho = \frac{1}{\sigma} \quad \text{Eq.2}$$

Chip efficiency can be then calculated with Eq.3,

$$\eta = \frac{R_b}{R_{mem}+R_b} \quad \text{Eq.3}$$

where R_{mem} represents resistance of PDMS/CB membrane and R_b is the resistance of Deionized water or other potential working fluid. Note that compared to membrane resistance, resistance of bulk fluid is relatively small, thus using high resistive fluid, such as deionized water can significantly improving calculation accuracy by minimizing

measurement errors. The measured chip efficiency with filled DI water is around 40-50%, which is comparable to other reported designs. However, we do expect low chip efficiency when using conductive buffer as working fluid due to a much smaller R_b in Eq.3.

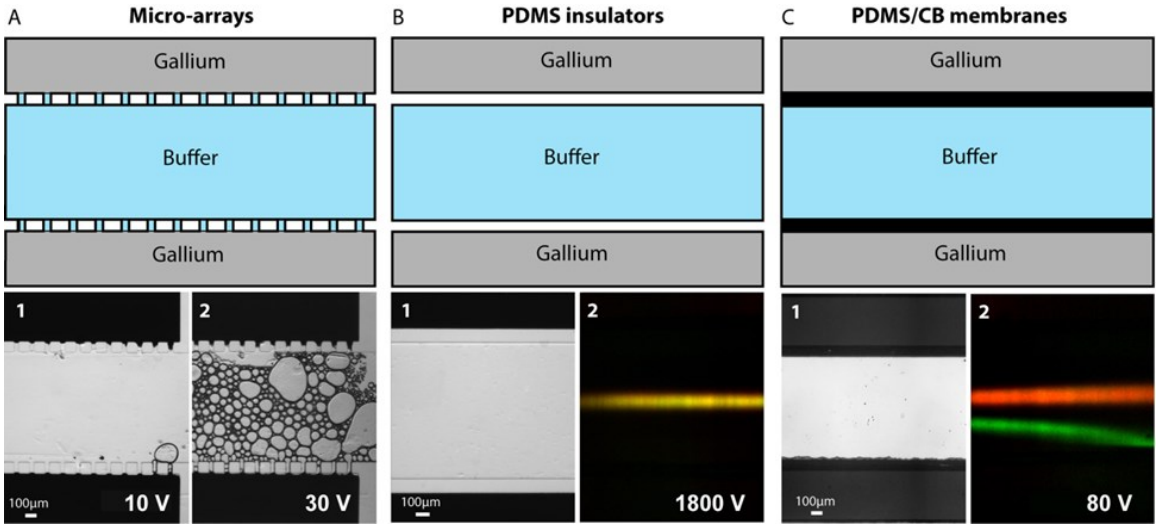

Figure 2-7. PDMS/CB membranes improve the performance of microfluidic FFE devices compared to systems without these features. (A) A device using micro side-channel arrays to isolate metal gallium electrode. (A-1) Due to the direct contact between the gallium electrode and the working buffer, electrode degradation and gas bubble were noticed under 30 V. (A-2) A much stronger Faradaic reaction occurred when more conductive buffer (PBS) was used under the same voltage. (B) 100μm wide PDMS membranes were placed between the gallium electrodes and the main flow channel. (B-1) No noticeable electro-thermal flow or buffer electrolysis below 1800 V. (B-2) No FFE was observed with PDMS insulators: the position of the fluorescent sample stream remained in the same position when 1800 V was applied. (C) A device with carbon black nano-powder patterned PDMS membranes. (C-1) No observable electro-thermal flow or bubble generation at 80V. (C-2) Effective FFE separation of the two fluorescent dyes was achieved under the same voltage. Reprinted with permission

2.5 Fabrication of a new conductive polymer membrane

While liquid electrodes with continuously electrolyte refreshing are very popular in designing on-chip field delivery system due to the superiorities in ventilation and cooling, liquid electrodes can suffer from evaporation and require extra pumping units to maintain stable electrical properties. On the contrary, metal electrodes such as gallium or gold can easily integrate into microfluidic systems and alleviate these issues. For portability purposes, we used gallium, a low melting point metal, and directly injected into a microfluidic channel in liquid form and solidified. As such, they can create 3D electrode structures with minimal fabrication costs. In this section, we describe how to integrate these 3D gallium electrodes into PDMS microchannels with conductive sidewalls for electric field delivery.

2.5.1 Gallium electrodes

Gallium has a low melting point and low viscosity, which makes it a good candidate for micro electrode. To fabricate each metal electrode, solid gallium metal was melted and injected into the electrode channels of the microdevice. Briefly, solid gallium metal (Sigma-Aldrich, 263265) and the PDMS chip were heated on a hot plate at 40 °C. With a melting temperature of 29.7 °C, the newly melted liquid gallium was loaded into a 1 mL plastic syringe and immediately injected into the electrode side channels. Liquid gallium has a low viscosity (1.37mPa-s) and therefore no PDMS surface treatment was

required prior to injection. Gallium solidified once cools down to room temperature. In case that air bubbles are trapped inside electrode channel and cause bad electrical connections, simply reheat the chip and pressurize the side channel until bubbles disappear. For circumstances that deadened electrodes are required, gallium filling can be accomplished by continuously pressurizing the electrode channel with melted gallium. Electrical connection was made using 0.75 mm diameter copper wire leads inserted into each electrode injection hole. This method sealed the electrodes into each channel and created an electrical connection for an external power source.

2.5.2 Prepare carbon blacks nano-composite PDMS

PDMS is an inert polymer that inherently lacks significant conductive properties. However, conductivity can be increased by combining the elastomer with a conducting powder, such as carbon black or silver nanoparticles, to create conductive polymer composites ((127)). When combined with standard soft lithographic techniques, composites can be patterned into specific structures that are suitable for on-chip applications (128). For example, Landa et al. (129) created conductive elastomer using PDMS/nickel powder composites to create a sensitive on-chip pressure sensor and Niu et al. (130) utilized soft lithography and PDMS/silver nanoparticles to fabricate arrays of conductive composite-based on-chip circuits. One benefit of this approach is that PDMS composites inherit increased electrical conductivity, but still retain the elastomeric

characteristics of PDMS, which allows them to be integrated into microfluidic systems using soft lithography.

To create conductive PDMS composite membranes, carbon nanopowder (Sigma-Aldrich, 633100) was combined with PDMS elastomer and mechanically mixed in a centrifugal mixer (Thinky, ARM 310) at 2000 RPM for 2 minutes. The carbon powder was added at different wt%, ranging between 5% - 20%, in order to study the influence of PDMS composite resistivity on device performance. Note that adding carbon powder not only enhances PDMS conductivity, it also influences physical properties of PDMS, such as transparency and viscosity. We only added maximum of 20 wt% carbon powder because PDMS starts to behave like solid material with more than 20% carbon powder and becomes extremely hard to pattern.

2.5.3 Fabricate device

The electric field delivery design consists of a main flow channel and two separate electrode-containing channels. The electrode channels are filled with gallium metal, each of which is fabricated directly against a patterned region of micron-thick PDMS/CB composite membrane as we previously described. To fabricate the composite membranes at specific regions within a microfluidic channel sidewall, we employed a novel multistage soft lithographic process, shown in the process flow diagram in Figure 2-8. First, a negative photoresist, SU-8 3050 (Microchip Corp.), was used to fabricate a soft lithographic mold with a main flow channel and gallium electrode channels. The

conductive PDMS composite are prepared following protocol in section 2.5.2. The nano-composite PDMS gel with different weight percent (wt%) of carbon powder, ranging between 5% - 20%, was injected into each gap between the electrode channel and the main flow channel using a 1 mL plastic syringe. Excess gel was immediately removed from the SU-8 mold using a razor blade and a 1:10 mixture of PDMS elastomer and curing agent was poured atop the mold and allowed to cure for half hour at 80℃. The cured PDMS with integrated composite membranes was peeled off the mold. Fluid ports were punched into each channel inlet and outlet using a 0.75 mm biopsy punch (Ted Pella, Inc). The microchannel and a glass coverslip (Fisher Scientific, 12-548-5R) were exposed to oxygen plasma (Jelight, Model 42A), and immediately aligned and sealed under an inverted microscope. The microfluidic chip was baked for 24 hours at 80℃. This post-bond baking step improved the PDMS bond strength and prevented membrane leakage and rupture during operation.

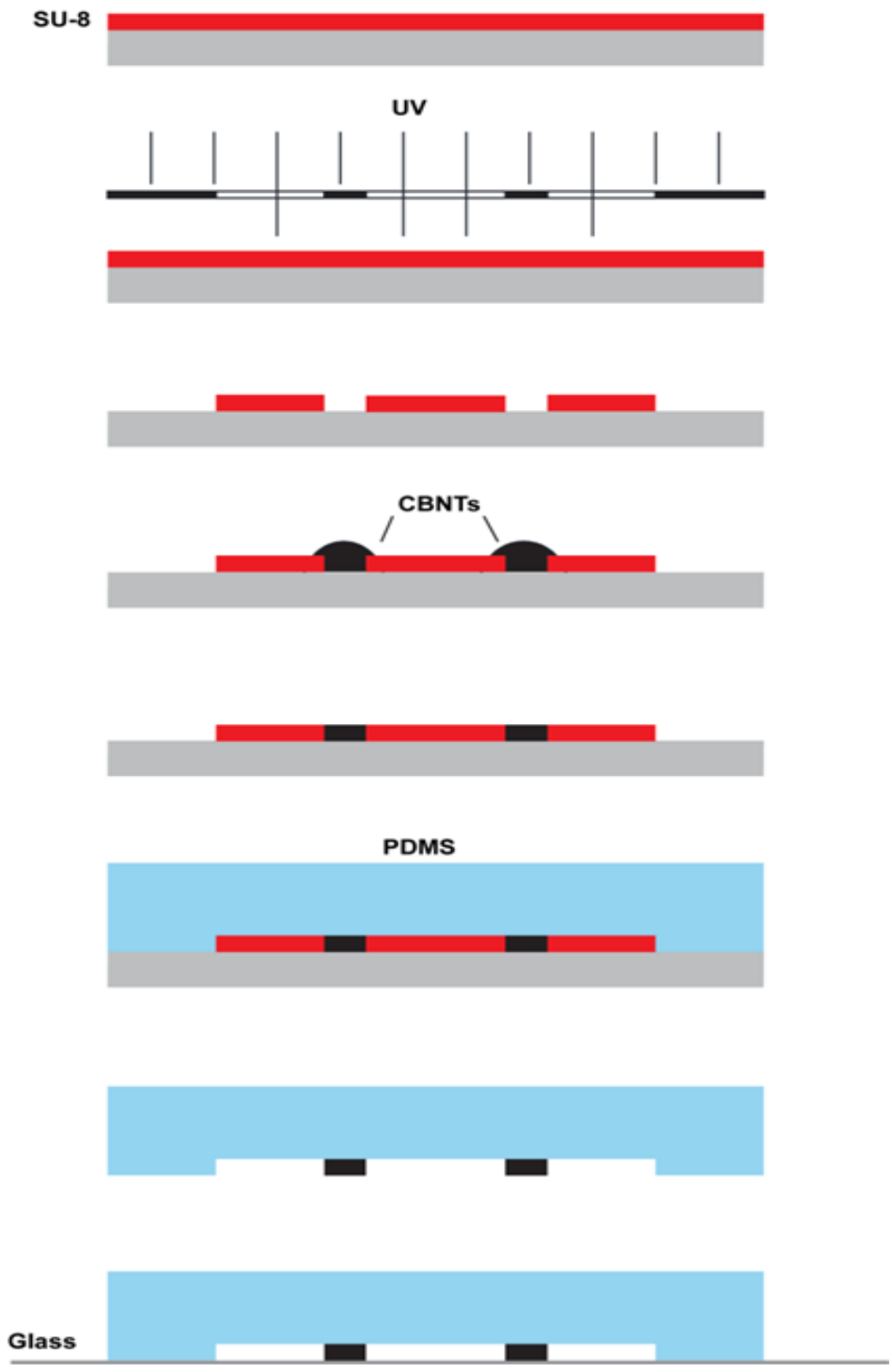

Figure 2-8. A demonstration of fabricating the conductive membrane and microfluidic chip. Negative photoresist, SU-8 3050 was spin-coated on a silicon wafer with 50um height. Then a photo mask covered the SU-8 photoresist before UV exposure. Uncovered photoresist solidified and remained on the silicon wafer to create a mold for casting. The

conductive PDMS composite gel was injected into each gap between the electrode channel and the main flow channel. The excess gel was immediately removed from the SU-8 mold using a razor blade. A 1:10 mixture of PDMS elastomer and curing agent was poured atop the mold and allowed to cure for half hour at 80℃. The cured PDMS with integrated composite membranes was peeled off the mold. The PDMS slab and a glass coverslip were exposed to oxygen plasma, and immediately aligned and sealed under an inverted microscope. The microfluidic chip was baked for 24 hours at 80℃.

References

1. S. C. Terry, J. H. Jerman, J. B. Angell. A gas chromatographic air analyzer fabricated on a silicon wafer. IEEE Transactions on Electron Devices. 1979;26(12):1880-6.

2. M. Esashi, S. Shoji, A. Nakano. Normally close microvalve and micropump fabricated on a silicon wafer. Micro Electro Mechanical Systems, 1989, Proceedings, An Investigation of Micro Structures, Sensors, Actuators, Machines and Robots. IEEE; ; 1989.

3. van dP, Wonnink DGJ, Elwenspoek M, Fluitman JHJ. A thermo-pneumatic actuation principle for a microminiature pump and other micromechanical devices. Sensors and Actuators. 1989;17(1):139-43.

4. Shoji S, Esashi M, Matsuo T. Prototype miniature blood gas analyser fabricated on a silicon wafer. Sensors and Actuators. 1988;14(2):101-7.

5. Esashi M. Integrated micro flow control systems. Sensors and Actuators A: Physical. 1990;21(1):161-7.

6. van der Schoot B, Bergveld P. An ISFET-based microlitre titrator: integration of a chemical sensor—actuator system. Sensors and Actuators. 1985;8(1):11-22.

7. Manz A, Graber N, Widmer HM. Miniaturized total chemical analysis systems: A novel concept for chemical sensing. Sensors Actuators B: Chem. 1990;1(1–6):244-8.

8. Branebjerg J, Fabius B, Gravesen P. Application of Miniature Analyzers: from Microfluidic Components to μTAS. In: Van den Berg A, Bergveld P, editors. Micro Total Analysis Systems: Proceedings of the μTAS ’94 Workshop, held at MESA Research

Institute, University of Twente, The Netherlands, 21–22 November 1994. Dordrecht: Springer Netherlands; 1995. p. 141-51.

9. Woolley AT, Mathies RA. Ultra-high-speed DNA fragment separations using microfabricated capillary array electrophoresis chips. Proc Natl Acad Sci U S A. 1994;91(24):11348-52.

10. Fan ZH, Harrison DJ. Micromachining of capillary electrophoresis injectors and separators on glass chips and evaluation of flow at capillary intersections. Anal Chem. 1994;66(1):177-84.

11. G Fuhr and T Schnelle and, B Wagner. Travelling wave-driven microfabricated electrohydrodynamic pumps for liquids. J Micromech Microengineering. 1994;4(4):217.

12. L. Bousse, A. Kopf-Sill, J. W. Parce. An electrophoretic serial to parallel converter. Solid State Sensors and Actuators, 1997. TRANSDUCERS '97 Chicago., 1997 International Conference on; ; 1997.

13. Shoffner MA, Cheng J, Hvichia GE, Kricka LJ, Wilding P. Chip PCR. I. Surface passivation of microfabricated silicon-glass chips for PCR. Nucleic Acids Res. 1996;24(2):375-9.

14. Koutny LB, Schmalzing D, Taylor TA, Fuchs M. Microchip Electrophoretic Immunoassay for Serum Cortisol. Anal Chem. 1996;68(1):18-22.

15. Tian W, Finehout E, SpringerLink. Microfluidics for biological applications. New York: Springer Science + Business Media; 2008.

16. Xia Y, Kim E, Zhao X, Rogers JA, Prentiss M, Whitesides GM. Complex Optical Surfaces Formed by Replica Molding Against Elastomeric Masters. Science. 1996;273(5273):347.

17. Kim E, Xia Y, Whitesides GM. Polymer microstructures formed by moulding in capillaries. Nature. 1995;376(6541):581-4.

18. Yi X, Kodzius R, Gong X, Xiao K, Wen W. A simple method of fabricating mask-free microfluidic devices for biological analysis. Biomicrofluidics. 2010;4(3):036503.

19. Li S, Day JC, Park JJ, Cadou CP, Ghodssi R. A fast-response microfluidic gas concentrating device for environmental sensing. Sensors and Actuators A: Physical. 2007;136(1):69-79.

20. Xia Y, Whitesides GM. Soft Lithography. Angewandte Chemie International Edition. 1998;37(5):550-75.

21. Chen X. On-Chip Pretreatment of Whole Blood by Using MEMS Technology. Sharjah: Bentham Science Publishers; 2012.

22. Abdul Karim N', Wan Ibrahim WA, Sanagi MM, Abdul Keyon AS. Online preconcentration by electrokinetic supercharging for separation of endocrine disrupting chemical and phenolic pollutants in water samples. Electrophoresis. 2016;37(20):2649-56.

23. Winkleman A, Perez-Castillejos R, Gudiksen KL, Phillips ST, Prentiss M, Whitesides GM. Density-Based Diamagnetic Separation: Devices for Detecting Binding Events and

for Collecting Unlabeled Diamagnetic Particles in Paramagnetic Solutions. Anal Chem. 2007;79(17):6542-50.

24. - Pawell RS, - Barber TJ, - Inglis DW, - Taylor RA. - Limits of Parabolic Flow Theory in Microfluidic Particle Separation: A Computational Study. 2013 -;-(-36154):V001T10A002.

25. Yamada M, Nakashima M, Seki M. Pinched Flow Fractionation: Continuous Size Separation of Particles Utilizing a Laminar Flow Profile in a Pinched Microchannel. Anal Chem. 2004;76(18):5465-71.

26. Zhu Z, Lu JJ, Liu S. Protein Separation by Capillary Gel Electrophoresis: A Review. Anal Chim Acta. 2011;709:21-31.

27. Tia S, Herr AE. On-chip technologies for multidimensional separations. Lab Chip. 2009;9(17):2524-36.

28. Herr AE, Molho JI, Drouvalakis KA, Mikkelsen JC, Utz PJ, Santiago JG, et al. On-Chip Coupling of Isoelectric Focusing and Free Solution Electrophoresis for Multidimensional Separations. Anal Chem. 2003;75(5):1180-7.

29. Yang J, Vykoukal J, Noshari J, Becker F, Gascoyne P, Krulevitch P, et al. DIELECTROPHORESIS-BASED MICROFLUIDIC SEPARATION AND DETECTION SYSTEMS. International journal of advanced manufacturing systems. 2000;3(2):1-12.

30. Rampini S, Kilinc D, Li P, Monteil C, Gandhi D, Lee GU. Micromagnet arrays for on-chip focusing, switching, and separation of superparamagnetic beads and single cells. Lab Chip. 2015;15(16):3370-9.

31. Skotis GD, Cumming DRS, Roberts JN, Riehle MO, Bernassau AL. Dynamic acoustic field activated cell separation (DAFACS). Lab Chip. 2015;15(3):802-10.

32. Kim SM, Sommer GJ, Burns MA, Hasselbrink EF. Low-Power Concentration and Separation Using Temperature Gradient Focusing via Joule Heating. Anal Chem. 2006;78(23):8028-35.

33. Wu Q, Bienvenue JM, Hassan BJ, Kwok YC, Giordano BC, Norris PM, et al. Microchip-Based Macroporous Silica Sol−Gel Monolith for Efficient Isolation of DNA from Clinical Samples. Anal Chem. 2006;78(16):5704-10.

34. Reedy CR, Bienvenue JM, Coletta L, Strachan BC, Bhatri N, Greenspoon S, et al. Volume reduction solid phase extraction of DNA from dilute, large-volume biological samples. Forensic Science International: Genetics;4(3):206-12.

35. Hua Y, Jemere AB, Harrison DJ. On-chip solid phase extraction and enzyme digestion using cationic PolyE-323 coatings and porous polymer monoliths coupled to electrospray mass spectrometry. Journal of Chromatography A. 2011;1218(26):4039-44.

36. Wang C, Jemere AB, Harrison DJ. Multifunctional protein processing chip with integrated digestion, solid-phase extraction, separation and electrospray. Electrophoresis. 2010;31(22):3703-10.

37. Asenjo JA, Andrews BA. Aqueous two-phase systems for protein separation: A perspective. Journal of Chromatography A. 2011;1218(49):8826-35.

38. Gonzlez-Gonzlez M, Rito-Palomares M. Aqueous two-phase systems strategies to establish novel bioprocesses for stem cells recovery. Crit Rev Biotechnol. 2014;34(4):318.

39. Thurmann S, Lotter C, Heiland JJ, Chankvetadze B, Belder D. Chip-Based High-Performance Liquid Chromatography for High-Speed Enantioseparations. Anal Chem. 2015;87(11):5568-76.

40. Thurmann S, Mauritz L, Heck C, Belder D. High-performance liquid chromatography on glass chips using precisely defined porous polymer monoliths as particle retaining elements. Journal of Chromatography A. 2014;1370:33-9.

41. Lichtenberg J, Verpoorte E, de Rooij NF. Sample preconcentration by field amplification stacking for microchip-based capillary electrophoresis. Electrophoresis. 2001;22(2):258-71.

42. Tiselius A. Electrophoresis of serum globulin. Biochem J. 1937;31(9):1464-77.

43. Prest JE, Baldock SJ, Fielden PR, Goddard NJ, Goodacre R, O'Connor R, et al. Miniaturised free flow isotachophoresis of bacteria using an injection moulded separation device. Journal of Chromatography B. 2012;903:53-9.

44. Stegehuis DS, Irth H, Tjaden UR, Van dG. Isotachophoresis as an on-line concentration pretreatment technique in capillary electrophoresis. J Chromatogr. 1991;538(2):393-402.

45. Wang J, Zhang Y, Okamoto Y, Kaji N, Tokeshi M, Baba Y. Online transient isotachophoresis concentration by the pseudo-terminating electrolyte buffer for the separation of DNA-aptamer and its thrombin complex in poly(methyl methacrylate) microchip. Analyst. 2011;136(6):1142-7.

46. Koenka IJ, Sáiz J, Rempel P, Hauser PC. Microfluidic Breadboard Approach to Capillary Electrophoresis. Anal Chem. 2016;88(7):3761-7.

47. Cheng LJ, Chang HC. Switchable pH actuators and 3D integrated salt bridges as new strategies for reconfigurable microfluidic free-flow electrophoretic separation. Lab On A Chip. 2014;14(5):979.

48. Huang LR, Cox EC, Austin RH, Sturm JC. Continuous Particle Separation Through Deterministic Lateral Displacement. Science. 2004;304(5673):987-90.

49. Inglis DW, Davis JA, Austin RH, Sturm JC. Critical particle size for fractionation by deterministic lateral displacement. Lab Chip. 2006;6(5):655-8.

50. Mohamed H, Turner JN, Caggana M. Biochip for separating fetal cells from maternal circulation. Journal of Chromatography A. 2007;1162(2):187-92.

51. McFaul SM, Lin BK, Ma H. Cell separation based on size and deformability using microfluidic funnel ratchets. Lab Chip. 2012;12(13):2369-76.

52. Ji HM, Samper V, Chen Y, Heng CK, Lim TM, Yobas L. Silicon-based microfilters for whole blood cell separation. Biomed Microdevices. 2008;10(2):251-7.

53. Murthy SK, Sethu P, Vunjak-Novakovic G, Toner M, Radisic M. Size-based microfluidic enrichment of neonatal rat cardiac cell populations. Biomed Microdevices. 2006;8(3):231-7.

54. Yamada M, Kano K, Tsuda Y, Kobayashi J, Yamato M, Seki M, et al. Microfluidic devices for size-dependent separation of liver cells. Biomed Microdevices. 2007;9(5):637-45.

55. Yamada M, Seki M. Hydrodynamic filtration for on-chip particle concentration and classification utilizing microfluidics. Lab Chip. 2005;5(11):1233-9.

56. Di Carlo D, Irimia D, Tompkins RG, Toner M. Continuous inertial focusing, ordering, and separation of particles in microchannels. Proceedings of the National Academy of Sciences. 2007 November 27;104(48):18892-7.

57. Russom A, Gupta AK, Nagrath S, Di Carlo D, Edd JF, Toner M. Differential inertial focusing of particles in curved low-aspect-ratio microchannels. New journal of physics. 2009;11:075025.

58. Takagi J, Yamada M, Yasuda M, Seki M. Continuous particle separation in a microchannel having asymmetrically arranged multiple branches. Lab Chip. 2005;5(7):778-84.

59. Huh D, Bahng JH, Ling Y, Wei H, Kripfgans OD, Fowlkes JB, et al. Gravity-Driven Microfluidic Particle Sorting Device with Hydrodynamic Separation Amplification. Anal Chem. 2007;79(4):1369-76.

60. Takahashi K, Hattori A, Suzuki I, Ichiki T, Yasuda K. Non-destructive on-chip cell sorting system with real-time microscopic image processing. Journal of Nanobiotechnology. 2004;2:5.

61. Valagerahally Puttaswamy S, Sivashankar S, Yeh C, Chen R, Liu CH. Electrodynamically actuated on-chip flow cytometry with low shear stress for electro-osmosis based sorting using low conductive medium. Microelectronic Engineering. 2010;87(12):2582-91.

62. Austin Suthanthiraraj PP, Piyasena ME, Woods TA, Naivar MA, López GP, Graves SW. One-dimensional acoustic standing waves in rectangular channels for flow cytometry. Methods. 2012;57(3):259-71.

63. Adams JD, Kim U, Soh HT. Multitarget magnetic activated cell sorter. Proc Natl Acad Sci U S A. 2008;105(47):18165-70.

64. Wang L, Flanagan LA, Jeon NL, Monuki E, Lee AP. Dielectrophoresis switching with vertical sidewall electrodes for microfluidic flow cytometry. Lab on a chip. 2007;7(9):1114-20.

65. Bhargava KC, Thompson B, Malmstadt N. Discrete elements for 3D microfluidics. Proceedings of the National Academy of Sciences. 2014 October 21;111(42):15013-8.

66. Gong J, Kim C"J. Direct-referencing Two-dimensional-array Digital Microfluidics Using Multi-layer Printed Circuit Board. Journal of microelectromechanical systems : a joint IEEE and ASME publication on microstructures, microactuators, microsensors, and microsystems. 2008;17(2):257-64.

67. E. D. Hobbs, A. P. Pisano. Micro capillary-force driven fluidic accumulator/pressure source. TRANSDUCERS, Solid-State Sensors, Actuators and Microsystems, 12th International Conference on, 2003; ; 2003.

68. D J Laser and, J G Santiago. A review of micropumps. J Micromech Microengineering. 2004;14(6):R35.

69. Hartshorne H, Backhouse CJ, Lee WE. Ferrofluid-based microchip pump and valve. Sensors & Actuators B: Chemical. 2004;99(2):592.

70. C. Yamahata, M. Chastellain, V. K. Parashar, A. Petri, H. Hofmann, M. A. M. Gijs. Plastic micropump with ferrofluidic actuation. Journal of Microelectromechanical Systems. 2005;14(1):96-102.

71. Micro gear pump with internal electromagnetic drive. Microsystem Technologies. 2010.

72. van Lintel, H T G, van De Pol, F C M, Bouwstra S. A piezoelectric micropump based on micromachining of silicon. Sensors and Actuators. 1988;15(2):153-67.

73. Anders Olsson and Peter Enoksson and Göran Stemme and, Erik Stemme. A valve-less planar pump isotropically etched in silicon. J Micromech Microengineering. 1996;6(1):87.

74. C G J Schabmueller and M Koch and M E Mokhtari and A G R Evans and A Brunnschweiler and, H Sehr. Self-aligning gas/liquid micropump. J Micromech Microengineering. 2002;12(4):420.

75. Stehr M, Messner S, Sandmaier H, Zengerle R. The VAMP — a new device for handling liquids or gases. Sensors and Actuators A: Physical. 1996;57(2):153-7.

76. M Elwenspoek and T S J Lammerink and R Miyake and, J H J Fluitman. Towards integrated microliquid handling systems. J Micromech Microengineering. 1994;4(4):227.

77. W K Schomburg and D Maas and W Bacher and B Bustgens and J Fahrenberg and W Menz and, D Seidel. Assembly for micromechanics and LIGA. J Micromech Microengineering. 1995;5(2):57.

78. Tang WC, Nguyen TH, Howe RT. Laterally Driven Polysilicon Resonant Microstructures. Sensors and Actuators. 1989;20(1):25-32.

79. Jr-Hung Tsai, Liwei Lin. A thermal-bubble-actuated micronozzle-diffuser pump. Journal of Microelectromechanical Systems. 2002;11(6):665-71.

80. Unger MA, Chou H, Thorsen T, Scherer A, Quake SR. Monolithic Microfabricated Valves and Pumps by Multilayer Soft Lithography. Science. 2000;288(5463):113-6.

81. Bohm S, Olthuis W, Bergveld P. A plastic micropump constructed with conventional techniques and materials. Sensors and actuators A: Physical. 1999;77(3):223-8.

82. Marseille O, Habib N, Reul H, Rau G. Implantable Micropump System for Augmented Liver Perfusion. Artificial Organs. 1998;22(6):458-60.

83. Jeong S, Seyed-Yagoobi J. Experimental study of electrohydrodynamic pumping through conduction phenomenon. J Electrostatics. 2002;56(2):123-33.

84. Richter A, Plettner A, Hofmann KA, Sandmaier H. A micromachined electrohydrodynamic (EHD) pump. Sensors and Actuators A: Physical. 1991;29(2):159-68.

85. Ramsey RS, Ramsey JM. Generating Electrospray from Microchip Devices Using Electroosmotic Pumping. Anal Chem. 1997;69(6):1174-8.

86. Paul PH, Arnold DW, Rakestraw DJ. Electrokinetic Generation of High Pressures using Porous Microstructures. In: Harrison DJ, van den Berg A, editors. Micro Total Analysis Systems '98: Proceedings of the uTAS '98 Workshop, held in Banff, Canada, 13–16 October 1998. Dordrecht: Springer Netherlands; 1998. p. 49-52.

87. Yao S, Santiago JG. Porous glass electroosmotic pumps: theory. Journal of Colloid & Interface Science. 2003;268(1):133.

88. Chuan-Hua Chen, Santiago JG. A Planar Electroosmotic Micropump. J Microelectromech Syst. 2002;11(6):672.

89. ac electroosmotic pumping induced by noncontact external electrodes. Biomicrofluidics. 2007;1(3):034106.

90. Jang J, Lee SS. Theoretical and experimental study of MHD (magnetohydrodynamic) micropump. Sensors and Actuators A: Physical. 2000;80(1):84-9.

91. Luginbuhl P, Collins SD. Microfabricated lamb wave device based on PZT sol-gel thin film for mechanical transport of solid.. J Microelectromech Syst. 1997;6(4):337.

92. Analysis of a micromachine based vacuum pump on a chip actuated by the thermal transpiration effect. Journal of Vacuum Science & Technology B: Microelectronics and Nanometer Structures Processing, Measurement, and Phenomena. 1999;17(2):280-7.

93. Kim J, Baek J, Lee K, Park Y, Sun K, Lee T, et al. Photopolymerized check valve and its integration into a pneumatic pumping system for biocompatible sample delivery. Lab On A Chip. 2006;6(8):1091.

94. Harrison DJ, Fluri K, Seiler K, Fan Z, Effenhauser CS, Manz A. Micromachining a miniaturized capillary electrophoresis-based chemical analysis system on a chip. Science (New York, N.Y.). 1993;261(5123):895.

95. Effenhauser CS, Manz A. Glass chips for high-speed capillary electrophoresis separations with submicrometer plate heights. Anal Chem. 1993;65(19):2637.

96. Jacobson SC, Hergenroder R. Effects of injection schemes and column geometry on the performance of microchip electrophoresis.. Anal Chem. 1994;66(7):1107.

97. Lapos JA, Ewing AG. Injection of fluorescently labeled analytes into microfabricated chips using optically gated electrophoresis. Anal Chem. 2000;72(19):4598.

98. Slentz BE, Penner NA, Regnier F. Sampling BIAS at channel junctions in gated flow injection on chips. Anal Chem. 2002;74(18):4835.

99. Lee NY, Yamada M, Seki M. Pressure-driven sample injection with quantitative liquid dispensing for on-chip electrophoresis. Analytical Sciences: The International Journal Of The Japan Society For Analytical Chemistry. 2004;20(3):483.

100. Cho SI, Lee SH, Chung DS, Kim YK. Bias-free pneumatic sample injection in microchip electrophoresis. Journal Of Chromatography.A. 2005;1063(1-2):253.

101. - Microchip electrophoresis with hydrodynamic injection and waste-removing function for quantitative analysis. - Journal of Chromatography A. (- 1–2):69.

102. Fu L-, Yang R-, Lee G-, Liu H-. Electrokinetic Injection Techniques in Microfluidic Chips. Anal Chem. 2002;74(19):5084.

103. Roh E, Hwang BU, Kim D, Kim BY, Lee NE. Stretchable, Transparent, Ultrasensitive, and Patchable Strain Sensor for Human-Machine Interfaces Comprising a Nanohybrid of Carbon Nanotubes and Conductive Elastomers. ACS Nano. 2015;9(6):6252.

104. H. S. Shin, Y. L. Park. Improved pressure response with embedded solid microbeads in microfluidic soft sensors. IEEE SENSORS 2014 Proceedings; ; 2014.

105. J. Lichtenberg, A. Hierlemann. Liquid-core, piezoresistive, fully polymer-based pressure sensor. The 13th International Conference on Solid-State Sensors, Actuators and Microsystems, 2005. Digest of Technical Papers. TRANSDUCERS '05. ; 2005.

106. Y. Sekimori, Y. Yoshida, T. Kitamori. Pressure sensor for micro chemical system on a chip. Proceedings of IEEE Sensors, 2004. ; 2004.

107. Berthet H, Jundt J, Durivault J, Mercier B, Angelescu D. Time-of-flight thermal flowrate sensor for lab-on-chip applications. Lab Chip. 2011;11(2):215-23.

108. F. Ender, H. Santha, V. Szekely. Flow sensor for microfluidic applications Based on standard PWB technology. 2009 32nd International Spring Seminar on Electronics Technology; ; 2009.

109. Lima R, Wada S, Takeda M, Tsubota K, Yamaguchi T. In vitro confocal micro-PIV measurements of blood flow in a square microchannel: The effect of the haematocrit on instantaneous velocity profiles. J Biomech. 2007;40(12):2752.

110. Lien V, Vollmer F. Microfluidic flow rate detection based on integrated optical fiber cantilever. Lab Chip. 2007;7(10):1352-6.

111. Janasek D, Schilling M, Franzke J, Manz A. Isotachophoresis in Free-Flow Using a Miniaturized Device. Anal Chem. 2006;78(11):3815.

112. Islinger M, Weber G. Free flow isoelectric focusing : a method for the separation of both hydrophilic and hydrophobic proteins of rat liver peroxisomes. Methods Mol Biol. 2008;432:199.

113. Nascimento EM, Nogueira N, Silva T, Braschler T, Demierre N, Renaud P, et al. Dielectrophoretic sorting on a microfabricated flow cytometer: label free separation of Babesia bovis infected erythrocytes. Bioelectrochemistry. 2008;73(2):123.

114. Macounová K, Cabrera CR, Holl MR, Yager P. Generation of Natural pH Gradients in Microfluidic Channels for Use in Isoelectric Focusing. Anal Chem. 2000;72(16):3745-51.

115. Lu H, Gaudet S, Schmidt MA, Jensen KF. A Microfabricated Device for Subcellular Organelle Sorting. Anal Chem. 2004;76(19):5705-12.

116. Zhang C, Manz A. High-speed free-flow electrophoresis on chip. Anal Chem. 2003;75(21):5759-66.

117. Raymond DE, Manz A, Widmer HM. Continuous sample pretreatment using a free-flow electrophoresis device integrated onto a silicon chip. Anal Chem. 1994;66:2858.

118. Janasek D, Schilling M, Manz A, Franzke J. Electrostatic induction of the electric field into free-flow electrophoresis devices. Lab On A Chip. 2006;6(6):710.

119. Schasfoort RBM, Schlautmann S, Hendrikse J, van den Berg A. Field-Effect Flow Control for Microfabricated Fluidic Networks. Science. 1999;286(5441):942-5.

120. Fonslow BR, Barocas VH, Bowser MT. Using Channel Depth To Isolate and Control Flow in a Micro Free-Flow Electrophoresis Device. Anal Chem. 2006;78(15):5369-74.

121. Kobayashi H, Shimamura K, Akaida T, Sakano K, Tajima N, Funazaki J, et al. Free-flow electrophoresis in a microfabricated chamber with a micromodule fraction separator: Continuous separation of proteins. Journal of Chromatography A. 2003;990(1–2):169-78.

122. Kohler S, Benz C, Becker H, Beckert E, Beushausen V, Belder D. Micro free-flow electrophoresis with injection molded chips. RSC Adv. 2012;2(2):520-5.

123. Kohlheyer D, Besselink GA, Schlautmann S, Schasfoort RB. Free-flow zone electrophoresis and isoelectric focusing using a microfabricated glass device with ion permeable membranes. Lab on a Chip. 2006;6(3):374-80.

124. Albrecht JW, Jensen KF. Micro freef-low IEF enhanced by active cooling and functionalized gels. Electrophoresis. 2006;27(24):4960-9.

125. de Jesus DP, Blanes L, do Lago CL. Microchip free-flow electrophoresis on glass substrate using laser-printing toner as structural material. Electrophoresis. 2006;27(24):4935-42.

126. Song Y, Wu L, Tannenbaum SR, Wishnok JS, Han J. Tunable Membranes for Free-Flow Zone Electrophoresis in PDMS Microchip using Guided Self-Assembly of Silica Microbeads. Anal Chem. 2013;85(24):11695-9.

127. Han-Sheng Chuang and, Steven Wereley. Design, fabrication and characterization of a conducting PDMS for microheaters and temperature sensors. J Micromech Microengineering. 2009;19(4):045010.

128. Chao-Xuan Liu aJ. Patterning conductive PDMS nanocomposite in an elastomer using microcontact printing. J Micromech Microengineering. 2009;19(8):085019.

129. Landa RA, Soledad Antonel P, Ruiz MM, Perez OE, Butera A, Jorge G, et al. Magnetic and elastic anisotropy in magnetorheological elastomers using nickel-based nanoparticles and nanochains. J Appl Phys. 2013;114(21):213912.

130. Niu X , Peng S , Liu L , Wen W , Sheng P. Characterizing and Patterning of PDMS-Based Conducting Composites. Adv Mater. 2007;19(18):2682-6.

3 Microfluidic Free-Flow Zone Electrophoresis And Isotachophoresis Using Carbon Black Nano-Composite PDMS Sidewall Membranes[a]

3.1 Overview

We present a new type of free-flow electrophoresis (FFE) device for performing on-chip microfluidic isotachophoresis (ITP) and zone electrophoresis (ZE). FFE is performed using metal gallium electrodes, which are isolated from a main microfluidic flow channel using thin micron-scale polydimethylsiloxane/carbon black (PDMS/CB) composite membranes integrated directly into the sidewalls of the microfluidic channel. The thin membrane allows for field penetration and effective electrophoresis, but serves to prevent bubble generation at the electrodes from electrolysis. We experimentally demonstrate the ability to use this platform to perform on-chip free-flow electrophoretic separation and isotachophoretic concentration. Due to the small size and simple fabrication procedure, this PDMS/CB platform could be used as part of an on-chip upstream sample preparation toolkit for portable microfluidic diagnostic applications.

[a]Reprinted with permission from Fu, X; Fu, X., Mavrogiannis, N., Ibo, M., Crivellari, F. and Gagnon, Z. R. (2016), ELECTROPHORESIS. doi:10.1002/elps.201600104

3.2 Introduction

Micro-total analysis (μTAS) platforms that can perform complex fluidic routing, sample processing and conventional laboratory assays have attracted significant interest as automated solutions for use in biomolecular and chemical analysis applications. Due to small scale fluid flows, short residence times and rapid sample processing, μTAS systems are used in a broad range of applications, including point of care diagnostics [1-3], metabolic profiling [4,5], cell analysis [6], drug screening [7,8], and environmental monitoring [9]. Despite significant advances in downstream sample detection technology, few lab-on-a-chip devices exist that can perform analysis on a raw unprepared sample [10]. The lack of methods available for on-chip upstream processing and sample preparation places a large bottleneck to the successful development of fully automated μTAS systems.

Free flow electrophoresis (FFE) methods are capable of performing preparative sample preconcentration and separation. In FFE, an electric field is applied across a flowing sample stream. The field drives charged molecules in solution to electrophoretically migrate across the channel at a velocity based on their size and electric charge. Molecules are then continuously collected in distinct separation streams at downstream microchannel outlets. Unlike classical capillary electrophoresis, which batch processes discrete plugs of analyte, the sample injection, separation and collection steps are performed continuously in FFE, making it an attractive candidate for high

throughput sample processing. FFE, for example, can continuously isolate cellular components, proteins, peptides and enzymes from complex mixtures [11-13]. Current microfluidic devices employing FFE, however, are bulky, difficult to fabricate and can suffer from Joule heating and bubble generation, which can limit their portability and molecular separation efficiency.

In this work, we demonstrate a new microfluidic platform for performing microfluidic FFE. Like conventional methods for producing FFE, the strategy described here uses electrodes integrated within a separation channel to deliver an electric field perpendicular to the direction of flow. Unlike other methods, however, we use electrically conductive PDMS/CB composite membranes to isolate electrodes from the analyte stream. The membranes are activated using adjoining electrodes fabricated from gallium metal. The combined CB/PDMS-gallium system is simple to fabricate and can deliver a stable and uniform direct current (DC) electric field across the channel. Using our proof of concept device we demonstrate the ability to perform on-chip molecular separation with free-flow zone electrophoresis (FFZE) and preparative sample separation and concentration using free-flow isotachophoresis (FFITP).

In the first part of this paper, we describe the fundamental electric field and electrolyte conditions required to produce FFZE and FFITP. We then demonstrate the benefits of our PDMS/CB membrane and gallium metal electrode design by comparing FFE performance to designs without insulating membranes and without PDMS integrated

with carbon black. Finally, we illustrate the capability to drive FFE by presenting experimental results for manipulating charged fluorescent dyes using FFZE and FFITP.

3.3 Background

Free-flow zone electrophoresis is an FFE method that combines fluid flow with DC electric fields in order to drive separation of proteins and charged biomolecules in flowing solution. In FFE, a sample is driven continuously into a separation channel and an electric field is applied perpendicular to the direction of flow. The combination of hydrodynamic molecular advection and perpendicular electrical fields produces a combined force vector that drives charged molecules to migrate at an angle dependent on both the magnitude of the flow velocity and the molecule electrophoretic mobility. When two molecular species have different mobilities, the resulting analyte vectors are at different angles and each species is separated continuously at the outlet of the separation channel.

Isotachophoresis is another well-established electrophoresis technique that serves as a method for charged molecular separation and concentration. In ITP, a sample containing one or more species of charged molecules is placed within a terminating electrolyte (TE) solution, which has a low electrophoretic mobility relative to the species in the sample. Separation is performed by placing the sample solution adjacent to a leading electrolyte (LE), which has ions with greater mobility than the TE and the sample molecules. When an electric field is applied, target molecules with an intermediate

mobility between the LE and TE electrophoretically migrate and stack into concentrated bands in the order of their mobility at the TE/LE interface. ITP has been used both as a batch method in capillary electrophoresis and continuously [14] using FFE to drive the separation of many types of charged molecules including nucleic acids from whole blood [15, 16], protein separation [17], and analysis of pathogenic bacteria [18, 19].

Despite significant research and development, current FFE methods still have several limitations. Because the electric field can often produce a high current in the electrolyte solution, FFE systems often suffer from Joule heating, bubble generation and unwanted electro-osmotic flow, which can lead to band broadening and reduced separation resolution. Several approaches have been reported in literature seeking to alleviate these challenges. One method is to simply reduce the voltage applied to the electrodes inside the separation channel to avoid buffer electrolysis. While effective, this places limits on separation efficiency [20]. Others have used chemical additives such as quinhydrone to alleviate electrolysis and gas bubble generation [31]. Another method is to use conductive liquid electrodes. To allow for large voltages, but prevent bubbles from entering the main flow channel, liquid electrodes are isolated using a large series of microscale channels [21-23] or acrylamide gel membranes [24-26]. However, gel membranes have poor mechanical strength and drying problems, while microchannel networks require precise flow control to prevent the electrode solution from leaking into the main flow channel.

Another strategy is to use solid electrical insulators, such as thin glass sidewall membranes, to separate electrodes from the main separation channel [27]. When a voltage is applied, a stable electric field forms inside the channel without producing bubble generation or Joule heating. However, a significant portion of the applied voltage is dropped across the insulating membranes, and limits the efficiency of the device. Recently, Song et al. reported the ability to tune the electrical conductivity of sidewall membranes using microbeads [28]. This method was successful in producing stable FFE, but requires significant fabrication and is currently not capable of being mass produced for wide scale use.

While many FFE designs use liquid electrodes with mechanical isolation to prevent electrolytic products and Joule heating from impacting device performance, liquid electrodes can suffer from evaporation and require extra pumping units to maintain stable electrical properties. On the contrary, metal electrodes such as gallium or gold can easily integrate into microfluidic systems and alleviate these issues. Gallium, a low melting point metal, is capable of being injected into a microfluidic channel in liquid form and solidified. As such, they can create 3D electrode structures with minimal fabrication costs [29]. In the next section we describe how to integrate these 3D gallium electrodes into PDMS microchannels with conductive sidewalls for use as FFE electrodes.

3.4 Materials and Methods

3.4.1 Device Fabrication

Here, we show the fabrication and operation of our conductive membrane-based FFE microfluidic platform. Each microfluidic FFE device, as shown in Figure 3-1a, consists of a main flow channel and two separate electrode-containing channels. The electrode channels are fabricated directly against patterned regions of PDMS/CB membranes. To locally pattern each membrane, we used a multistage soft lithographic process we have reported previously [30]. Briefly, we fabricated a soft lithographic microchannel mold using a negative photoresist, SU-8 3050 (Microchem Corp). Each device consisted of a main flow channel 1 mm in width and two gallium electrode channels separated from the main flow channel by a 100 micron-thick gap (Figure 3-1b). To create local conductive CB membranes within these gaps, carbon nano-powder (Sigma-Aldrich, 633100) was combined at a 1:5 weight ratio with PDMS elastomer and mechanically mixed in a centrifugal mixer (Thinky, ARM 310) at 2000 rpm for 3 min. The resulting nano-composite gel was then injected into each gap using a 1ml syringe. After removing the excess gel using a razor blade, a 1:10 mixture of PDMS elastomer and curing agent was poured atop the mold and allowed to cure for an hour at 85°C. The cured PDMS slab was gently peeled off the mold and fluid ports at each channel inlet and outlet were punched using a 0.75 mm biopsy punch (Ted Pella, Inc.). The device and a glass coverslip were exposed to oxygen plasma (Jetlight, Model 42A) and immediately

aligned and sealed under an inverted microscope. Finally, the chip was baked for 24 hours at 85°C to improve PDMS bond strength and prevent membrane leakage during use. The resulting chip consisted of a main flow chamber 1 mm wide and 1 cm long integrated with CB sidewall membranes on each side. Each flow channel has five fluid inlets, five outlets and two side electrode channels. Fluid flow was driven into each inlet using a custom built constant pressure flow controller.

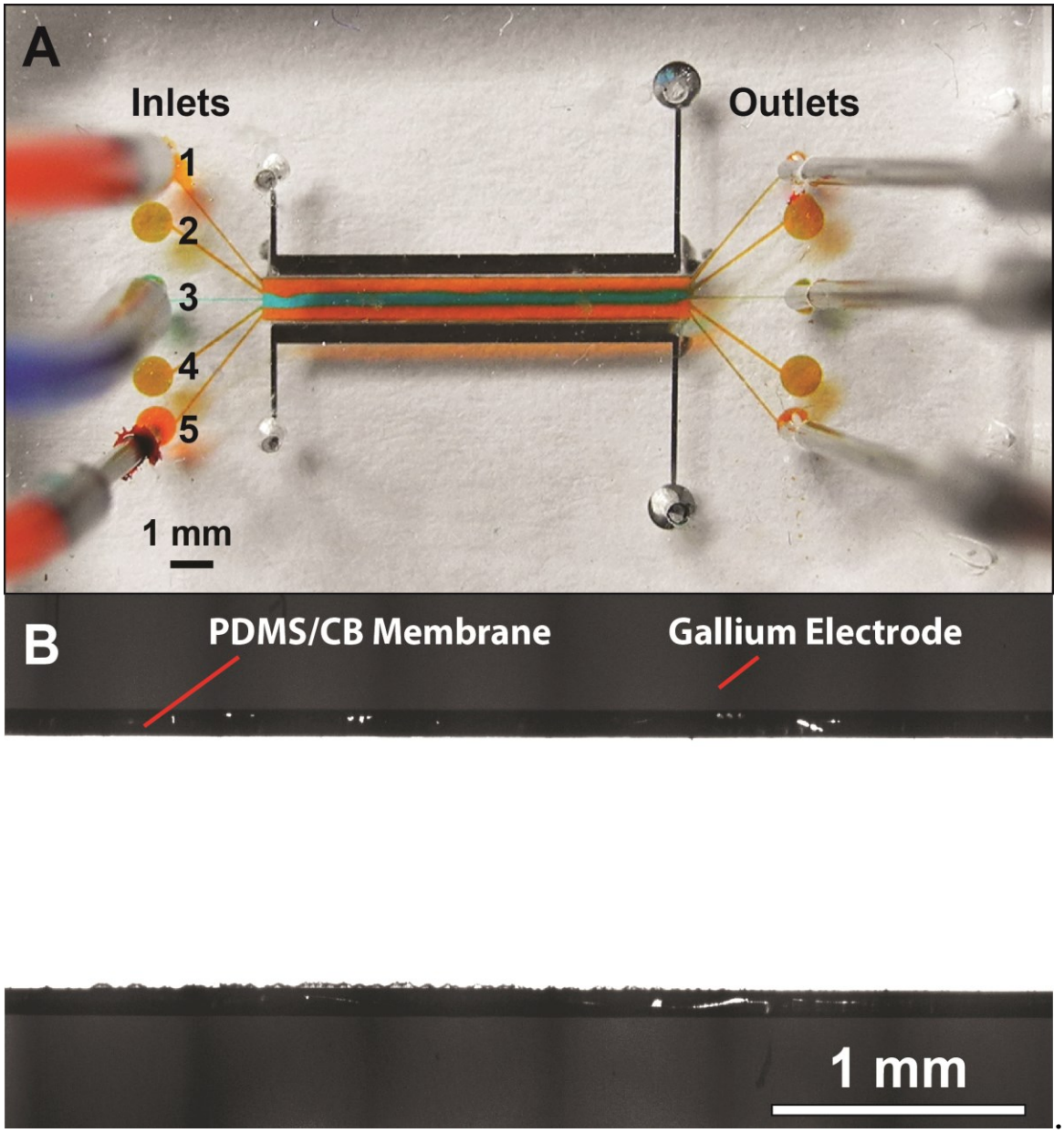

Figure 3-1. Microfluidic device used to perform microfluidic free-flow electrophoresis. (A) The FFE device contains five fluidic inlets and five outlets used to perform on-chip zone electrophoresis and isotachophoresis. Electrodes on each side of the separation channel are used to apply an electric field perpendicular to the flow direction. (B) A micrograph of the electrodes surrounding the microchannel. Each gallium electrode is isolated from the flow channel by a 100 micron-thick PDMS/CB composite membrane.

3.4.2 Chemicals and Reagents

All chemicals used in this work were purchased from Sigma-Aldrich unless otherwise stated. For the FFZE experiment, the working buffer solution contained 10 mM 4-(2-hydroxyethyl)-1-piperazineethanesulfonic acid (HEPES) with 20mM Bis-Tris, 1% Tween 20 and 0.1% hydroxypropylmethylcellulose (HPMC) (pH 6.8). HPMC is a soluble polymer that is added to the electrolyte to suppress electro-osmotic flow and Tween 20 serves as a surfactant to reduce adsorption of molecules to the microchannel surface. For the FFITP experiments, the leading electrolyte (LE) solution contained 10 mM HCl, 20mM Bis-Tris,1% Tween 20 and 0.1% HPMC. The terminating electrolyte (TE) solution was comprised of 10mM HEPES, 20mM Bis-Tris, 1% Tween 20 and 0.1% HPMC. FFE experiments were performed using charged fluorescent dyes - fluorescein, Alexa Fluor 591, Alexa Fluor 488 (Lifescience technology) and rhodamine B. Stock solutions (1 mg/mL) were prepared in advance and working buffers were prepared immediately prior to experiments by adding fluorescent dyes to the electrolyte solutions. 1 mg/mL p-benzoquinone and 1 mg/mL hydroquinone were added to the buffer solutions right before experiment to avoid bubble formation when large voltage (>200 V) was applied.

3.4.3 Free-Flow Zone Electrophoresis

To perform FFZE, the working electrolyte was driven into both inlet 2 and inlet 4 at a flow rate of 2 μL/min. The sample stream containing fluorescein and rhodamine B

was introduced between these two fluid streams using inlet 3, which was hydrodynamically focused at a flow rate of 0.5 μL/min (Figure 3-3a). The quinhydrone was introduced into inlets 1 and 5 at 2 μL/min. A high voltage power supply (PS325, Stanford Research System, CA) was wired to the electrode pair to create the necessary electric field in the main flow channel. When the power supply was turned on, the resulting potential difference created an electric field perpendicular to the direction of flow and forced fluorescent dye in solution to electrophoretically migrate across the microchannel.

3.4.4 Free-flow Isotachophoresis

FFITP concentrating experiments were conducted by adding Alexa 488 into the TE and co-flowing this solution with the LE. All fluids were driven into device inlets at 2 μL/min. The LE was directed into inlet 2 and the dyed TE was driven into the main flow chamber using inlet 4. The quinhydrone was mixed with the LE and TE and pumping continuously into inlet 1 and 5, respectively. The unused inlet 3 was blocked during experiment. Again, a positive voltage was applied to the electrode adjacent to the LE and the electrode near the TE was grounded. The electric field was used to drive the charged Alexa 488 to rearrange and stack at the interface between the LE and TE (Figure 3-5a). To demonstrate FFITP separation capability, a similar experimental procedure was performed by replacing Alexa Fluor 488 with Alexa Fluor 591 and fluorescein.

3.5 Results and Discussions

3.5.1 Free flow zone electrophoresis

We next used our PDMS/CB design to perform on-chip FFZE to separate fluorescein and rhodamine B (Figure 3-3a). The separation chamber was primed with HEPES buffer to purge air from the device. Sample mixture was flow-focused into a thin stream in the channel center (Figure 3-3b). When we applied a potential of 80V across the channel, fluorescein separated from the sample stream. Because fluorescein is negatively charged at a pH of 6.8, shown in green, it was driven towards the positively charged anode while rhodamine B, in red, was neutral at pH 6.8 and remained unaffected by the electrical field (Figure 3-3c). The separation distance between the two dyes increased as the solution flowed down the separation device. Due to a high electrophoretic mobility, the time required for fluorescein to reach a steady free-flow separation took less than one second. We reversed the field direction and observed the same result except with fluorescein migrating in the opposite direction. In both cases, no noticeable EO flow was observed. A plot of fluorescent intensity as a function of channel width is shown in Figure 3-4. When the field was applied, the green fluorescent peak (fluorescein) shifted to the right while the red peak (rhodamine B) remained fixed in its original position.

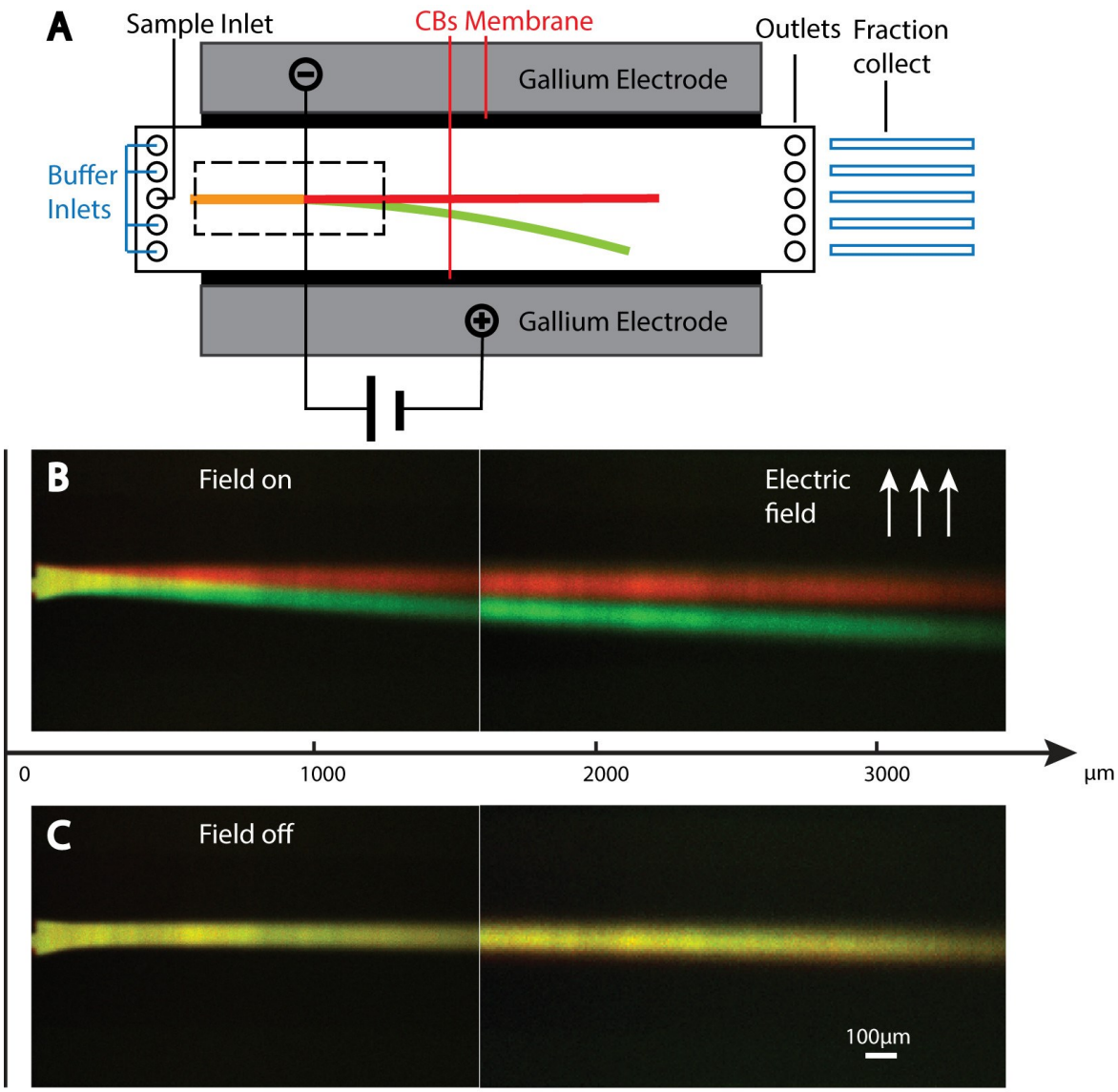

Figure 3-2. Microfluidic free-flow zone electrophoresis. (A) Schematic of the experiment used to separate two different fluorescent dyes. (B) A stream of fluorescein and rhodamine B are flow-focused in the center of the microfluidic separation channel. (C) An electric field is applied across the channel and negatively charged fluorescein electrophoretically migrates across the channel width, separating from the neutral rhodamine B.

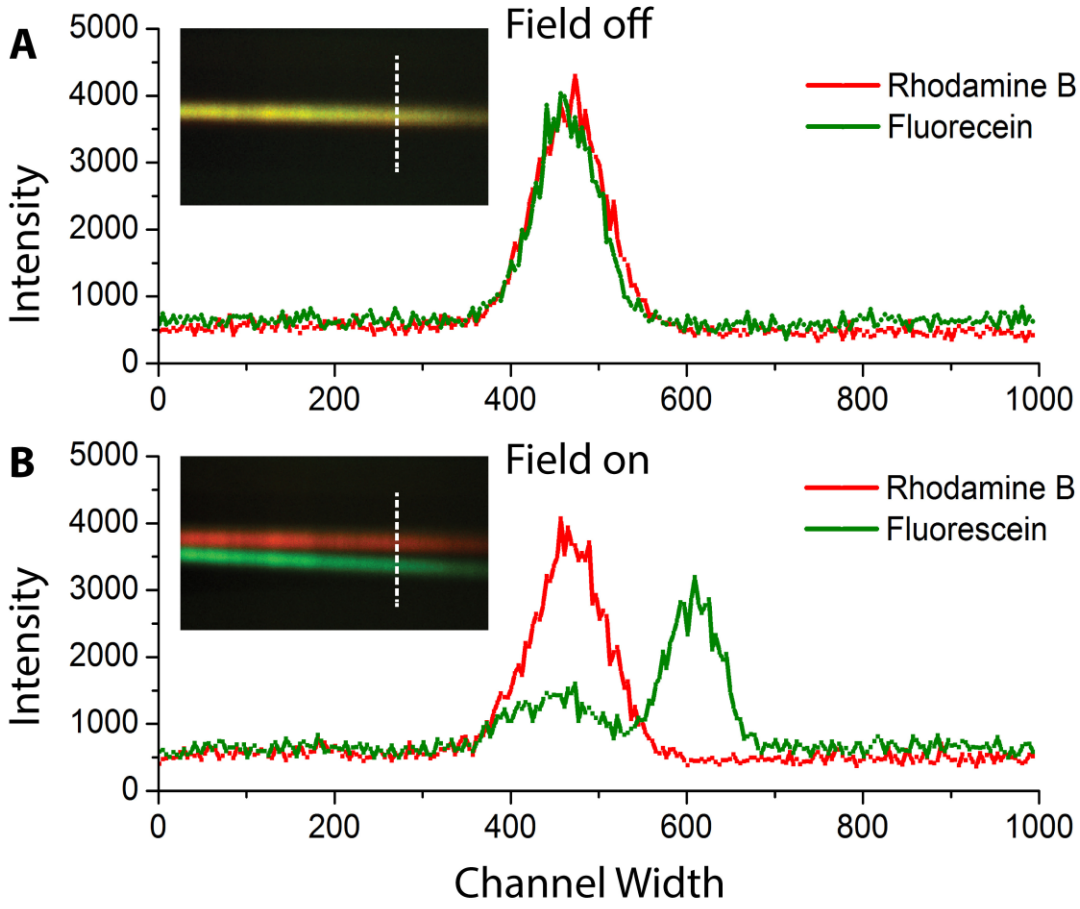

Figure 3-3. Comparison of the fluorescent intensity profile at the cross section of the microfluidic channel with (A) the electric field off and (B) the electric field on.

3.5.2 Free flow isotachophoresis

We also used our PDMS/CB platform to perform free flow isotachophoresis. FFITP is an effective FFE technique for the separation and concentration of charged molecules. We performed experiments using the negatively charged fluorescent molecule Alexa Flour

488. To perform ITP, the LE, TE and quinhydrone solutions were driven through the device. When an electric field was applied across the microchannel from the LE to the TE, Alexa Fluor 488 concentrated at the LE-TE interface (Figure 3-4). The width of the concentrated band decreased as the applied voltage was increased. A micrograph illustrating ITP concentration at 200, 300 and 400V is shown in Figure 3-4(b-d) with corresponding intensity plots in Figure 3-4e. As a control experiment, we replaced the LE and TE with deionized water. Under these conditions, Alexa Fluor 488 was observed to migrate across the entire channel to the opposite sidewall and no concentration was observed, demonstrating the mechanism responsible for interfacial concentration was ITP.

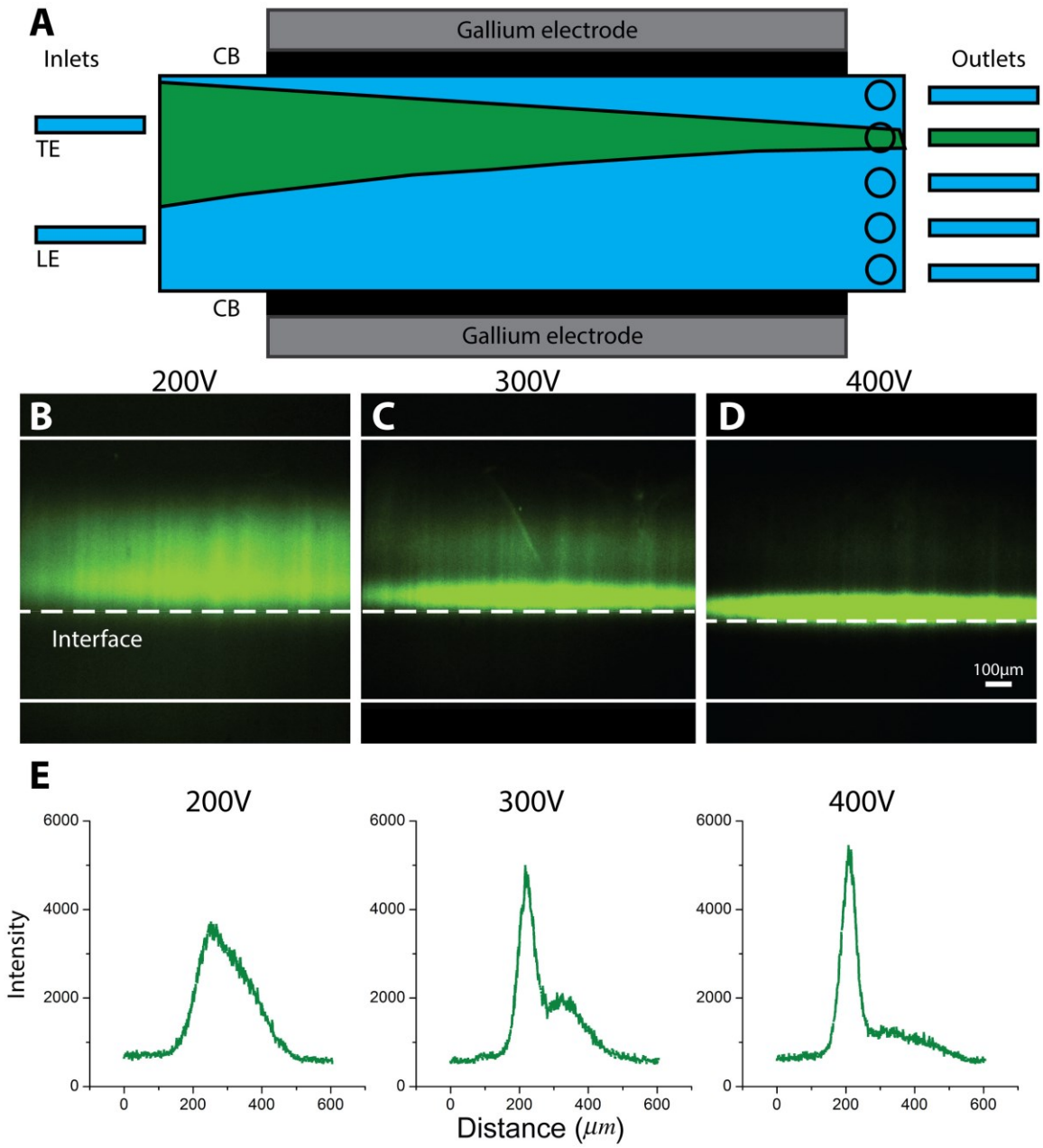

Figure 3-4. Concentration by microfluidic free-flow isotachophoresis. (A) Schematic of the experiment used to concentrate fluorescent Alexa Fluor 488 dye at the interface between the leading electrolyte (LE) and terminating electrolyte (TE). An electric field is applied across the channel and fluorescent micrographs were taken at the TE/LE interface at (B) 200 V, (C) 300 V, and (D) 400 V. (E) Comparison of the fluorescent intensity profile at the cross section of the microfluidic channel for each voltage applied.

We next investigated the ability to perform ITP separation using two different fluorescent molecules - Alexa Fluor 591 and fluorescein – to simulate two different charged biomolecules. Both markers were mixed into the TE, as previously described, and introduced into the separation chamber. Before an electric field was applied, the stream appeared orange under confocal microscopy, with a uniform mixture of Alexa Fluor 591 (red) and fluorescein (green) across the flow channel (Figure 3-5a). When 300 V was applied across the channel, both the fluorescein and Alexa Fluor 591 migrated towards the LE-TE interface (Figure 3-5b). Alexa Fluor 591 has a higher electrophoretic mobility than fluorescein, and was observed to migrate faster in the applied field. Thus, we observed two focused fluorescent bands formed in the center of the channel, with the red Alexa Fluor 591 forming against the interface and fluorescein stacking directly behind. Micrographs of the interface and the ITP stacking are shown in Figure 3-5c and 5d, respectively. The fluorescent intensity profiles before (Figure 3-5e) and after the field is applied (Figure 3-5f) illustrate the ability to use this device to perform ITP separations. Concentration enrichment was observed during separation, where the peak intensity of Alexa Fluor 591 and fluorescein were increased by 2 and 1.5 fold, respectively. The enrichment of FFITP may be limited due to the total amount of ions available inside separation chamber and the separation residence time. However, FFITP separation offers a means to perform molecule separation and enrichment simultaneously with a much higher sample processing rate, which makes it a potential candidate for on-chip sample pretreatment.

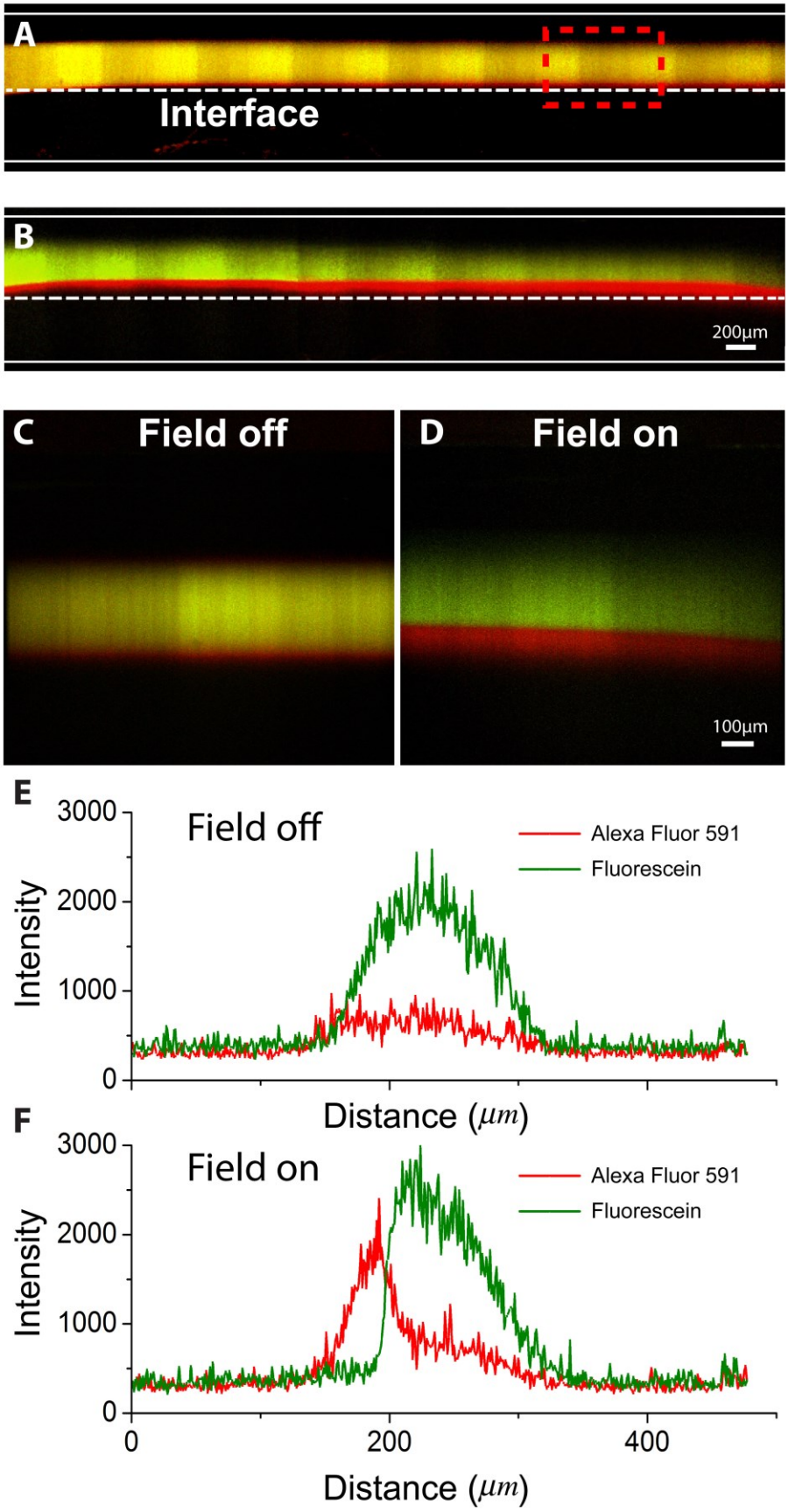
A
Interface
B
200μm
C
Field off
D
Field on
100μm
E
Field off
Alexa Fluor 591
Fluorescein
Intensity
3000
2000
1000
0
Distance (μm)
F
Field on
Alexa Fluor 591
Fluorescein
Intensity
3000
2000
1000
0
0
200
400
Distance (μm)

Figure 3-5. Isotachophoretic separation of Alexa 591 and fluorescein dyes. (A) A mixture of each dye in the TE flows adjacent to the LE. (B) An electric field is applied across the two fluid streams and the two fluorescent dyes stack against the LE/TE interface. (C) A micrograph of the interface with no electric field applied and (D) with the electric field applied. The fluorescent intensity profile of the TE/LE interface taken with the (E) field off and (F) the field on.

3.6 Conclusions

In this work, we have demonstrated an approach for using PDMS/CB membranes for performing free-flow electrophoresis in microfluidic channels. Typical microfluidic FFE methods use networks of resistive side-channels, conductive acrylamide gels, mechanical resistors, or shallow-deep channel banks, to improve separation efficiency and prevent bubble electrolysis from impacting separation performance. However, these designs can be bulky, suffer from electrode evaporation, and require significant fabrication steps to produce. Our FFE design uses metal gallium electrodes and patterned carbon black PDMS membranes to produce local, three dimensional DC electric fields without Faradaic reactions or electrothermal flow. We demonstrated this device's capability to suppress common FFE issues without inhibiting FFE separation efficiency, and used this electrode system to perform FFZE separation, FFITP concentration, and FFITP separation. This new platform has potential to provide a low-cost and portable method for on-chip sample preparation for portable diagnostics and environmental monitoring applications. Compared to previously reported FFE devices for on-chip

separation and concentration, the gallium-PDMS/CB membrane design offers an inexpensive and portable solution for performing microfluidic FFE. The devices are easy to fabricate compared to traditional methods that use resistive gels or glass membranes and the PDMS membrane can be tuned to a desired electrical and/or mechanical properties according to specific experimental requirements by adding different nano-materials to the elastomer. Future work will focus on using this platform for performing on-chip sample preparations in real-world samples including blood serum and urine.

Reference

[1] Tüdős, A. J., Besselink, G. A., Schasfoort, R. B. Lab on a Chip 2001, 1, 83-95.

[2] Ahn, C. H., Choi, J., Beaucage, G., Nevin, J. H. et al. Proc IEEE 2004, 92, 154-173.

[3] Kovarik, M. L., Ornoff, D. M., Melvin, A. T., Dobes, N. C. et al. Anal. Chem. 2013, 85, 451.

[4] Liu, B., Ozaki, M., Hisamoto, H., Luo, Q. et al. Anal. Chem. 2005, 77, 573-578.

[5] Kraly, J. R., Holcomb, R. E., Guan, Q., Henry, C. S. Anal. Chim. Acta 2009, 653, 23.

[6] Young, E. W., Berthier, E., Guckenberger, D. J., Sackmann, E. et al. Anal. Chem. 2011, 83, 1408.

[7] Neuži, P., Giselbrecht, S., Länge, K., Huang, T. J., Manz, A. Nature Reviews Drug Discovery 2012, 11, 620-632.

[8] Dittrich, P. S., Manz, A. Nature Reviews Drug Discovery 2006, 5, 210-218.

[9] Jokerst, J. C., Emory, J. M., Henry, C. S. Analyst 2012, 137, 24.

[10] Mariella Jr, R. Biomed. Microdevices 2008, 10, 777-784.

[11] Alrifaiy, A., Lindahl, O. A., Ramser, K. Polymers (20734360) 2012, 4, 1349.

[12] Hoffmann, P., Ji, H., Moritz, R. L., Connolly, L. M. et al. Proteomics 2001, 1, 807.

[13] Islinger, M., Eckerskorn, C., Völkl, A. Electrophoresis 2010, 31, 1754.

[14] Janasek, D., Schilling, M., Franzke, J., Manz, A. Anal. Chem. 2006, 78, 3815.

[15] Persat, A., Marshall, L. A., Santiago, J. G. Anal. Chem. 2009, 81, 9507.

[16] Rogacs, A., Qu, Y., Santiago, J. G. Anal. Chem. 2012, 84, 5858.

[17] Cui, H., Dutta, P., Ivory, C. F. Electrophoresis 2007, 28, 1138.

[18] Prest, J. E., Baldock, S. J., Fielden, P. R., Goddard, N. J. et al. Journal of Chromatography B: Analytical Technologies in the Biomedical & Life Sciences 2012, 903, 53.

[19] Schwartz, O., Bercovici, M. Anal. Chem. 2014, 86, 10106.

[20] Lu, H., Gaudet, S., Schmidt, M. A., Jensen, K. F. Anal. Chem. 2004, 76, 5705.

[21] Raymond, D. E., Manz, A., Widmer, H. M. Anal. Chem. 1996, 68, 2515-2522.

[22] Xu, Y., Zhang, C., Janasek, D., Manz, A. Lab on a Chip 2003, 3, 224-227.

[23] Zhang, C., Manz, A. Anal. Chem. 2003, 75, 5759-5766.

[24] Albrecht, J. W., Jensen, K. F. Electrophoresis 2006, 27, 4960-4969.

[25] de Jesus, D. P., Blanes, L., do Lago, C. L. Electrophoresis 2006, 27, 4935-4942.

[26] Kohlheyer, D., Eijkel, J. C., Schlautmann, S., Van Den Berg, A., Schasfoort, R. B. Anal. Chem. 2007, 79, 8190-8198.

[27] Janasek, D., Schilling, M., Manz, A., Franzke, J. Lab on a Chip 2006, 6, 710-713.

[28] Song, Y., Wu, L., Tannenbaum, S. R., Wishnok, J. S., Han, J. Anal. Chem. 2013, 85, 11695-11699.

[29] Fu, X., Mavrogiannis, N., Doria, S., Gagnon, Z. Lab Chip 2015, 15, 3600-3608.

[30] Fu, X., Gagnon, Z. Biomicrofluidics 2015, 9, 054122.

[31] Kohlheyer, D., Eijkel, J. C., Schlautmann, S., van den Berg, A., Schasfoort, R. B. Anal. Chem. 2008, 80, 4111-4118.

4 Microfluidic Pumping, Routing And Metering By Contactless Metal-Based Electro-Osmosis[b]

4.1 Overview

Over the past decade, many microfluidic platforms for fluid processing have been developed in order to perform on-chip fluidic manipulations. Many of these methods, however, require expensive and bulky external supporting equipment, which are not typically applicable for microsystems requiring portability. We have developed a new type of portable contactless metal electro-osmotic micropump capable of on-chip fluid pumping, routing and metering. The pump operates using two pairs of gallium metal electrodes, which are activated using an external voltage source, and separated from a main flow channel by a thin micron-scale PDMS membrane. The thin contactless membrane allows for field penetration and electro-osmotic (EO) flow within the microchannel, but eliminates electrode damage and sample contamination commonly associated with traditional DC electro-osmostic pumps that utilize electrodes in direct contact with the working fluid. The maximum flow rates and pressures generated by the pump using DI water as a working buffer are 10nL/min and 30 Pa, respectively. With our current design, the maximum operational conductivity where fluid flow is observed is 0.1mS/cm. We experimentally demonstrated the ability to quantify micropump electro-osmotic flow rate and pressure as a function of applied voltage, and developed a

[b] Reprinted with permission from Fu, X; Fu, X., Mavrogiannis N., Gagnon, Z., " Microfluidic Pumping, Routing, and Metering by Contactless Metal-Based Electro-osmosis", Lab on a Chip, (2015), 15, 3600-3608

mathematical model capable of predicting the performance of a micropump for a given external load and internal hydrodynamic microchannel resistance. Finally, we showed that by activating specific pumps within a microchannel network, our micropumps are capable of routing microchannel fluid flow and generating plugs of solute.

4.2 Introduction

The development of robust and portable microfluidic platforms capable of complex fluidic routing and handling operations without requiring external laboratory equipment is an important requirement for the next generation of portable micro total analysis systems (TAS, or lab-on-a-chip)[1]. Many microfluidic platforms have been developed that are capable of performing on-chip fluidic pumping[2], valving[3], mixing[4] and routing[5]. A popular method, known as microfluidic large-scale integration (LSI)[6], for example, utilizes thousands of integrated pressure-actuated elastomeric pumps and valves to handle fluidic operations. Another platform uses centrifugal forces to drive fluid flow within a network of microchannels valves situated atop a rotating microfluidic disk[7]. Others have used on-chip surface acoustic waves[8] and electrical forces[9] to perform on-chip fluidic operations. The past two decades in particular have demonstrated the effectiveness of these and other microfluidic platforms as enabling systems for performing fluid routing, mixing, and pumping for applications including nucleic acid extraction[10], protein crystallization[11], immunoassays[12], single cell analysis[13], and high throughput genetic screening[14]. The majority of these platforms, however, require large supporting equipment, which confine their usefulness to the laboratory, and are typically too large and expensive for use in portable environments, rural areas, and for general use by consumers. Applications suited for use in more portable settings (e.g. point-of-care

diagnostics) are limited due to the lack of robust and portable microfluidic platforms. The development of microfluidic lab-on-a-chip (LOC) systems that are portable, but still capable of performing a robust set of fluidic-based unit operations, is therefore an important aspect of microfluidic research. Progress in this area is largely limited due to inherent difficulties in performing desired tasks, such as fluid pumping and metering, without the need for large external driving systems. In terms of developing portable microfluidic systems for diagnostics, personalized medicine, and environmental monitoring, fluid manipulation technology is a central bottleneck in reaching this goal.

Micro-pumps can be generally divided into two categories: displacement pumps and kinetic pumps[15]. Displacement pumps, also known as mechanical pumps, utilize moving part such as membranes and valves to induce fluid flow. At the microscale, however, they often suffer from mechanical failure due to fouling or loss in membrane elasticity[16]. Kinetic pumps convert kinetic sources such as electromagnetic, thermal or chemical energy into fluid momentum to drive flow. Common types of kinetic pumps include electrohydrodynamic[17], electrokinetic[2], magnetohydrodynamic[18], thermomagnetic[19], electro wetting[20] and electrochemical[21].

Electrokinetic pumps in particular use electrical forces to induce electro-osmotic (EO) fluid flow and offer a popular alternative to mechanical displacement micropumps. Typically, however, EO pumps require direct contact between electric field-generating electrodes and a working fluid. When a direct current (DC) voltage is applied, Faradaic reactions occur at each electrode surface, which can lead to uncontrolled electrothermal fluid flow[22], electrode damage, and sample damage[23] from pH generation[24] and Joule heating[25].

Recently, a new type of contactless electrode device was developed for use in dielectrophoresis (DEP) by Sano et al[26]. In contactless DEP (cDEP), two conductive electrolyte channels serve as liquid electrodes, which are physically isolated from the main flow channel by a thin PDMS membrane. The application of an alternating current (AC) or DC voltage source across the liquid electrodes allows for electric field penetration through the membrane and into the main flow channel. This contactless approach eliminates Faradaic reactions and buffer contamination issues associated with traditional metal electrode systems, and has been successfully used for dielectrophoretic particle and cell sorting, and very recently demonstrated for microchannel electro-osmosis. Currently, however, these contactless devices have been based on external liquid electrodes. While effective, liquid electrodes lack the required features necessary for creating a portable microfluidic platform. First, liquid can suffer from liquid evaporation and cannot be reliably transported. Second, they require fluid injection ports and pipette tips to maintain electrical contact, and inherently possess a large operational footprint on-chip, which currently limits the number of active devices that can be effectively fabricated on a single chip.

Here, we present a new type of contactless direct current (DC) micropump for on-chip liquid pumping, routing, and metering that has the potential of being developed into a portable microfluidic fluid-handling platform. Instead of using liquid electrodes, our micropump design is based on 3D gallium metal electrodes fabricated directly into the sidewalls of microfluidic flow channels, and separated from the active flow region by a thin micron-scale PDMS polymer membrane (Figure 4-1a). To create an electric field within the main microchannel, two difference voltages are applied to each electrode pairs

(V1 and V2). The resulting electric field drives an electro-osmotic flow within the flow channel in the direction of the field applied. In terms of more portable fluid pumping and routing, the presented metal-based electrode design is a significant improvement over existing contactless electrokinetic devices that utilize liquid electrolyte electrodes. Most importantly, unlike liquid-based electrode designs, our metal-based contactless approach is scalable. Specifically, we demonstrate the ability to fabricate and independently operate multiple micropumps on a single microfluidic device for fluid pumping, routing, and metering. With the ability to activate and route fluid flow at different pumping locations on-chip independently over a microfluidic network, it is important to understand how to characterize and measure the contactless pump working capacity. With this in mind, we present two different microfluidic channel designs – a closed microfluidic circulating "loop" and a "T-shape" channel – with supporting theoretical pumping models to quantify the contactless pump working capacity under varying hydrodynamic loads. The closed circuit "Loop" is used to measure the flow rate in a fluid network with a known hydrodynamic resistance, which simulates microchannel systems solely driven by internal micropumps. Alternatively, the "T-shape" channel design is used to measure the pump working capability under pump maximum pressure, which characterizes the full pump working capability.

The first part of this chapter is an analysis of contactless electro-osmotic flow within a microchannel. The governing fluid transport equations are formulated and used to derive relations describing electro-osmotic flow rate in the presence of an arbitrary hydrodynamic resistance within a microfluidic network. These equations are then combined with an electrostatic model for our contactless electrode design, and utilized to

describe the relation between the applied voltage and the resulting induced electro-osmotic pressure. In the second part of this work, electro-osmotic flow rate experiments for two different microfluidic geometries are presented and combined with our contactless micropump model to quantitatively characterize the on-chip micropump. Finally, we demonstrate the usefulness of our gallium contactless micropumps by using them to perform microfluidic fluid routing and solute plug generation.

4.3 Theory

4.3.1 Electro-osmosis pump

In this section, we derive the theoretical formulation for electro-osmotic flow within a microfluidic channel and develop equations to relate the applied micropump voltage drop across a set of microchannel electrodes to that of the pressure gradient and flow rate produced by the electro-osmotic pump.

Electro-osmosis is an electrokinetic technique for pumping fluids in microfluidic channels.31 Solid-liquid surfaces tend to develop surface charge when in contact with aqueous liquids. This surface charge attracts counter-ions of opposite charge and repels co-ions of similar charge, and an electrical double layer (EDL) is formed. The resulting ionic double layer possesses a non-zero charge density and screens the solid surface charge over a characteristic Debye length. When an external electric potential, , is dropped parallel to the EDL, the ions suffer a Coulombic force and move towards the electrode of opposite polarity. This creates motion of the fluid near the wall and transfers momentum into the bulk fluid. Assuming the applied electric field is uniform inside the

EDL, the flow is unidirectional, and there is no external applied pressure gradient, the Stokes equations can be written as ,

$$0 = \mu \frac{\partial^2 u}{\partial y^2} - \varepsilon \frac{\partial^2 \phi}{\partial y^2} E_{wall} \quad (1)$$

where μ,ε, and E_{wall} are the fluid viscosity and electrolyte permittivity, and applied tangential electric field at the channel wall, respectively. In the absence of any external pressure gradient, the flow field within the EDL is adequately described though a balance between viscous stress and electric body force, and Eq. (1) can be integrated with a no slip condition at the wall (y=0) and a far-field condition that $\phi \to 0$ as $y \to \infty$ to give:

$$u_{slip} = \frac{\varepsilon E_{wall}}{\mu}(\phi - \phi_{wall}) \quad (2)$$

Here, the wall potential, $\phi_{wall} = \zeta e^{-y/\lambda_D}$, varies across the Debye length, λ_D , which exponentially approaches a Smoluchowski's slip velocity outside the diffuse layer,

$$u_{EO} = \frac{\varepsilon E_{wall} \zeta}{\mu} \quad (3)$$

where ζ is the zeta potential at the channel surface. For a channel of width, w, and height, d, the total electro-osmotic flow rate, QEO, is calculated by integrating Eq. (3) over the channel cross-section area:

$$Q_{EO} = -2wd \frac{\varepsilon E_{wall} \zeta}{\mu} \quad (4)$$

For the case where a micropump must drive fluid flow against a hydrodynamic load (e.g. within a network of microchannels), a backpressure is generated and the fluid

flow is reduced. A combination of EO flow and this counter backpressure is known as "frustrated" flow[9], and for a slot-shaped microchannel (i.e. the channel width is much larger than the height, w >> 2d) the total frustrated flow rate is a linear combination of EO and pressure driven back flow,

$$Q = \frac{2wd^3}{3\mu}\left[\frac{\partial P}{\partial x}\right] - 2wd\frac{\varepsilon E_{wall}\zeta}{\mu} \quad (5)$$

Illustrated in Figure 4-1a, for a given applied voltage drop, ΔV, dropped over an electrode separation length, L_E, the electric field at the wall is $\Delta V / L_E$. The back pressure gradient varies linearly along the micropump length, and can be written as $\Delta P / L_E$. The maximum pump pressure can be derived using Eq. (5). Setting Q=0, which is the case for a closed microchannel[32], the maximum EO-induced pump pressure can be written as:

$$\Delta P_{\max} = -\frac{3\mu u_{EO}}{d^2}\Delta V \quad (6)$$

In contrast, the maximum flow rate can be calculated by setting :

$$Q_{\max} = 2wdu_{EO}\frac{\Delta V}{L_E} \text{ . (7)}$$

Microfluidic channel designs that either of these two extreme cases are rare; neither the pressure nor net flow rate are zero. Combining Eqs. (5-7), a relation linking pumping flow rate and pressure is obtained:

$$\frac{\Delta P}{\Delta P_{\max}} + \frac{Q}{Q_{\max}} = 1 \text{ . (8)}$$

The induced flow rate, Q, is related to the pressure drop, ΔP, through the flow channel hydrodynamic resistance, Rh,

$$\Delta P = QR_h \quad .(9)$$

For a channel with a rectangular cross-section of height, h, width, w, and the condition that h > w, the hydrodynamic resistance over the total channel pumping length L is given by [33,34]

$$R_h = \frac{12\mu L}{wh^3(1-0.63h/w)} \quad . (10)$$

Eqs. (6-9) can be combined to derive the linear pump curve for the net flow rate and applied voltage of an EO pump,

$$Q = -\frac{6wd\mu u_{EO}}{2wd^3R_h - 3\mu L_E}\Delta V \, . \quad (11)$$

4.3.2 Voltage Drop Across a PDMS Membrane

Contactless micro pumps share similar electro-osmotic principles with traditional EO pumps, however, the high resistive PDMS membrane serves to reduce the potential drop within the microchannel (ΔV) from that of the total potential applied (ΔV_{total}). We apply a simple electro-current model to determine the relationship between the potential applied and the potential within the microchannel. The electrical resistance, R, of the PDMS membrane is related to the material resistivity (ρ), the membrane length (L_m), and cross-section area (A), as $R = \left(\rho L_m / A\right)$. In the absence of counter ion screening at the PDMS membrane surface, the electrical resistance of each PDMS membrane (R_{PDMS})

and bulk fluid (R_{fluid}) are calculated based on the equation above. By Ohm's law, the effective voltage drop across the working fluid is

$$\Delta V = \Delta V_{total} \frac{R_{fluid}}{R_{total}}, \qquad (12)$$

where $R_{total}=R_{PDMS} + R_{fluid}$.

When a DC voltage is dropped across the PDMS membrane, however, counter ions in the working electrolyte will accumulate at the PDMS-liquid interface, create an induced screening potential (ϕ_s) and reduce the magnitude of the electrostatic field in the main channel. The magnitude of this screening effect is a function to the applied electric field and counter ion concentration in the electrolyte solution. If the ion concentration is large enough, the applied field will be completely screened from the microchannel, and no electro-osmotic flow will be observed. If the applied voltage is large enough and able to exceed the screening potential, however, an electric field will penetrate into the bulk and impart an electro-osmotic slip velocity at the PDMS membrane surface.

A more general expression must take into account this screening potential, and link the total applied voltage to the voltage generated within the working flow channel,

$$\Delta V = \Delta V_{total} \frac{R_{fluid}}{R_{total}} - \phi_s . \qquad (13)$$

Eq. (13) can be combined with Eqs. (6) and (11) to give relationships between the applied voltage, the maximum pump pressure, and the net flow rate. We will use these expressions to quantify pump performance for each given microfluidic geometry. In this

work, we experimentally determine the screening potential from our experimental pump curves.

4.4 Materials and Methods

In this section, we describe the methods used to fabricate the microfluidic devices with integrated gallium metal electrodes, and how to operate these pumps with a high voltage external DC power supply.

4.4.1 Microfluidic Chip Fabrication

Each microfluidic pump consists of a flow channel, which is electrically isolated from four separate electrode channels by a thin PDMS membrane (Figure 4-1a). The entire device was fabricated using common soft lithographic techniques. Briefly, microchannels were fabricated in PDMS (Momentive, RTV 615A). A 1:10 mixture of PDMS elastomer and curing agent was poured atop a lithographically fabricated SU-8 3050 (Microchem Corp.) polymer mold, cured and gently peeled off. Fluid ports were punched into the PDMS using a 0.75 mm biopsy punch (Ted Pella, Inc.). The microchannel and coverslip were exposed to oxygen plasma (Jelight, Model 42A), immediately aligned and sealed under an inverted microscope, and baked for 24 hours at 80 ℃. This post-bond baking step improved the PDMS bond strength and prevented PDMS membrane leakage and rupture during pump operation. The completed device consisted of a main flow channel 300 m wide and 50 μm high with four galium electrode channels 900μm wide, each separated by a thin PDMS membrane, 45μm in thickness (Figure 4-1b).

To fabricate each metal electrode, solid gallium metal was melted and injected into the side channels of the microdevice. Briefly, solid gallium metal (Sigma-Aldrich, 263265) and the PDMS chip were heated to 40 ℃ on a hot plate. With a melting temperature of 29.7℃, the newly melted liquid gallium was loaded into a 1 mL plastic syringe and immediately injected into the electrode side channels. Liquid gallium has a low viscosity (1.37mPa-s)35 and therefore no PDMS surface treatment was required prior to injection. Electrical connection was made using 0.75 mm diameter copper wire leads inserted into each electrode injection hole. This method sealed the electrodes into each channel, and created an electrical connection for an external power source. With this fabrication process, multiple micropumps could be fabricated and utilized on a single microfluidic chip.

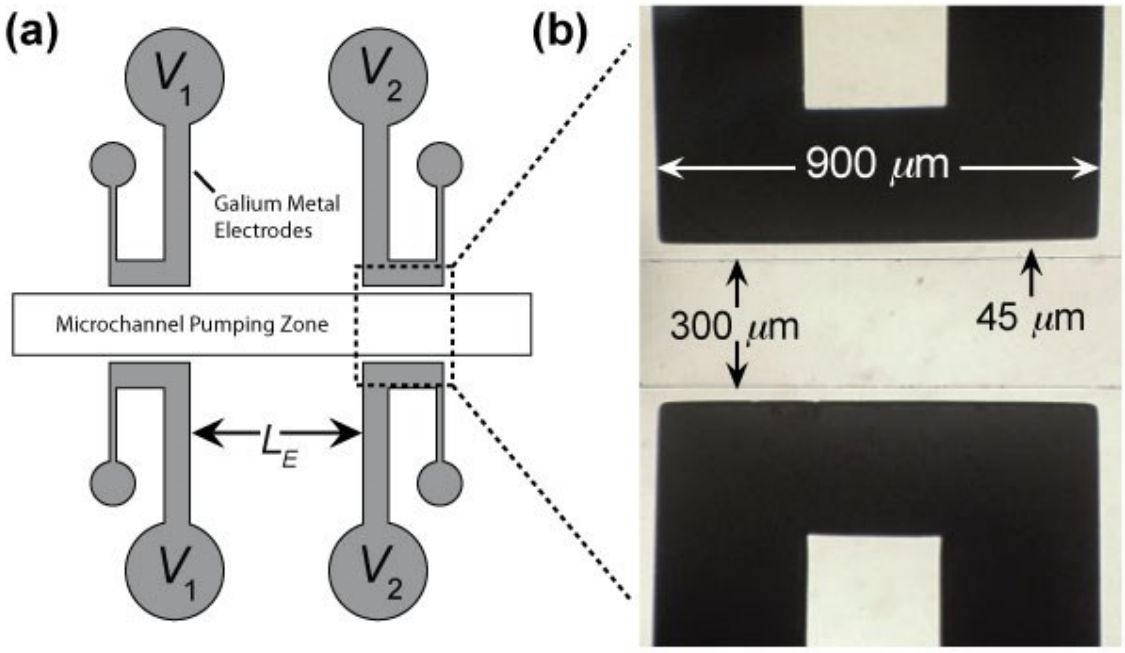

Figure 4-1. Schematic of a gallium metal contactless micropump. (a) A top view of a single pumping device. Each micropump contains four gallium electrodes separated from

the microchannel by a thin PDMS membrane. (b) A micrograph of a pair of electrodes surrounding a microchannel. Each electrode is 900 μm wide, separated from the main channel by a 45 μm thick PDMS membrane.

4.4.2 Reagents and Electrical Parameters

The pumping experiments were conducted using deionized water (DI). Silica particles and fluorescent dyes were used to image the induced electro-osmotic flow field and to quantify the fluid velocity. When using particles as flow tracers, 1.7 μm silica microparticles (Corpuscular Inc.) were diluted to 0.005% (w/v) in DI water. Zeta potential of the silica particles were measured to be -29.6 mV (Zetasizer , Malvern Instruments Ltd). Red and green fluorescent solutions were made by combining 100 μl stock solutions of Alexa Fluor 488 (green) and 594 (red) with 4 mL DI water. Both ionic fluorescent dyes and charged particle tracers can influence the electrical conductivity of the fluid, which could influence the accuracy of our theoretical calculations. Both ionic fluorescent dyes and charged particle tracers can influence the electrical conductivity of the fluid, which could influence the accuracy of our theoretical calculations. To take this into account, we based our pumping theory on the electrical conductivity of the fluorescent solutions and particle suspension used in this work. The electrical conductivity of fluorescent solutions and particle suspension used were 1μS/cm and -2μS/cm, respectively. The PDMS zeta potential used in our calculations was based on a low conductivity buffer at neutral pH: -30 mV.[31]

4.4.3 PDMS Membrane Resistivity

The electrical resistivity of PDMS is needed to calculate the effective voltage drop across the main flow channel (Eq. 13) and is an important parameter in determining

pump capability. The electrical resistivity of PDMS has been previously reported to be on the order of 10^{13} Ω-cm.[29] However, there is a wide range in reported values, and the electrical resistivity of a polymer can vary with temperature and mechanical stress.[36] After plasma bonding PDMS to a glass substrate and baking for 24 hours, we measured the resistivity of the PDMS membrane for each device using a high resistance ohmmeter (Alpha Labs Inc, Model HR2). The PDMS membrane resistivity in our loop device was 5.1×10^{10} Ω-cm and in the T-channel device it was 5.6×10^{10}. It is important to note, however, that we observed that PDMS post-bond baking time influences the PDMS resistivity. As baking time increases from 1 hour to more than 48 hours, the resistivity of PDMS membrane ascends from 10^{9} Ω-cm to 10^{13} Ω-cm, and approaches the reported value of PDMS resistivity.

Based on the measured fluid and PDMS resistivity, the resistance ratio given in Eq. (13), R_{fluid}/R_{total}, for the microfluidic loop and the T-channel used in this work were 1.2×10^{-3} and 2.2×10^{-3}, respectively.

4.4.4 Pump Operation

Each individual micropump was composed of four gallium electrodes, as shown in Figure 4-1a. To operate the pump, a high voltage power supply (PS325, Stanford Research System, CA) was wired to two separate electrode pairs – a high positive voltage (V1) was delivered to one pair, while the other two electrodes were connected to ground (V2). When the power supply was activated the two pairs of electrodes served to create a uniform electric field down the flow channel, which induced electro-osmotic flow in the

direction of the applied field. Reversing the polarity of the electrode array can therefore reverse the flow direction.

4.4.5 On-chip pump control

To automate the activation and operation of each micropump, a LabVIEW based interface was established to achieve independent control of each pumping module. A 24 channel DIO USB controller (24R Elexol, Australia) was used to send user-controlled 5V digital signals to a customized 12 volt PCB driver board. Each 12V signal was then used to activate a series of high voltage relays (Cynergy, DAT70510) that were connected to the high voltage DC power supply (PS325, Stanford Research System, CA). When a 12 volt signal was delivered to the relay, a DC high voltage (0.4 – 2.0 kV) was then delivered to a specific on-chip micropump.

4.5 Results and Discussions

4.5.1 Pump Characterization in a Closed Microfluidic Loop

First, experiments were performed on single pump within the microfluidic-closed loop with sealed inlet and outlet ports. In this microfluidic geometry, the back pressure within the loop is created by the pump, and the resulting flow rate is dictated by a combination of induced pump pressure and the microfluidic channel resistance, as described previously by Eq. (11). To quantify the total pump flow rate in terms of the applied voltage for a single device, flow experiments were performed using a single micro pump within the loop (Figure 4-2a). Fluid velocity was tracked by measuring the trajectories of individual microparticle tracers suspended within the working fluid. Because the particles are negatively charged and exhibit electrophoresis in a DC field, we

tracked particle motion on the opposing end of the loop to ensure that the electric field did not influence their motion. The fluid flow rate was calculated by equating the average fluid velocity with that of the channel cross-section area.

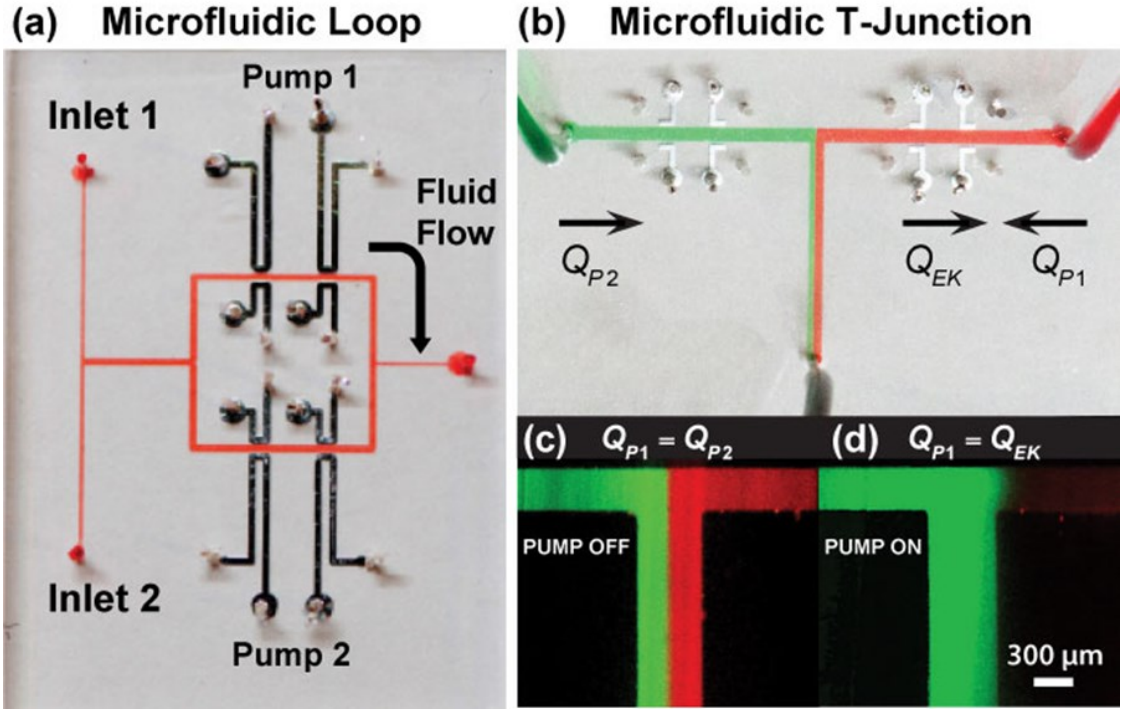

Figure 4-2. Microfluidic devices used to quantify the pumping flowrate vs voltage. (a) A microfluidic loop design with two integrated micropumps (1 and 2) is used to characterize pump performance under a fixed microchannel hydrodynamic resistance. (b) A microfluidic T-junction device is used to measure pump pressure under zero net flow rate. Two fluid streams are driven into the device using an external constant pressure source. (c) When the no pump is active and the flow rate of each stream is equal, the interface between the two fluid phases is centered within the main fluid channel. (d) The right-most pump is activated to completely cancel the pressure driven flow of the right-most fluid stream. When the pump flow rate is equal and opposite the pressure driven flow rate, the flow of this stream ceases and the interface position shifts towards the active pumping channel.

As is typical of traditional EO flow, shown in Figure 4-3, the experimentally measured flow rate is linearly proportional to the applied DC voltage. Unlike typical EO pumps, however, we observed an operational threshold voltage; below an applied voltage of 650 V no fluid motion was observed. We attribute this observation to double layer screening at the PDMS membrane surface. Because the DC electric field drives counter ion accumulation and the formation of an electric double layer at the microchannel sidewall, the electric field will be effectively screened from the main flow channel when the ion concentration is large enough to exceed the membrane surface potential. Above a critical value, however, there will not be enough counter ions in the bulk to screen the electric field and fluid flow will be observed.

Shown in Figure 4-3, the flow rate in the loop varies linearly from 2 - 10 nL/min as the applied potential increases from 1.2 kV to 2.3 kV. Using a screening potential of 650 V, the corresponding theoretical electro-osmotic flow rate from Eq. (11) is plotted against the experimental data in Figure 4-3. As shown, the mathematical model provides an accurate prediction of pumping performance against hydrodynamic resistance within a closed microfluidic loop over a range of applied voltage (.65 – 2.3 kV).

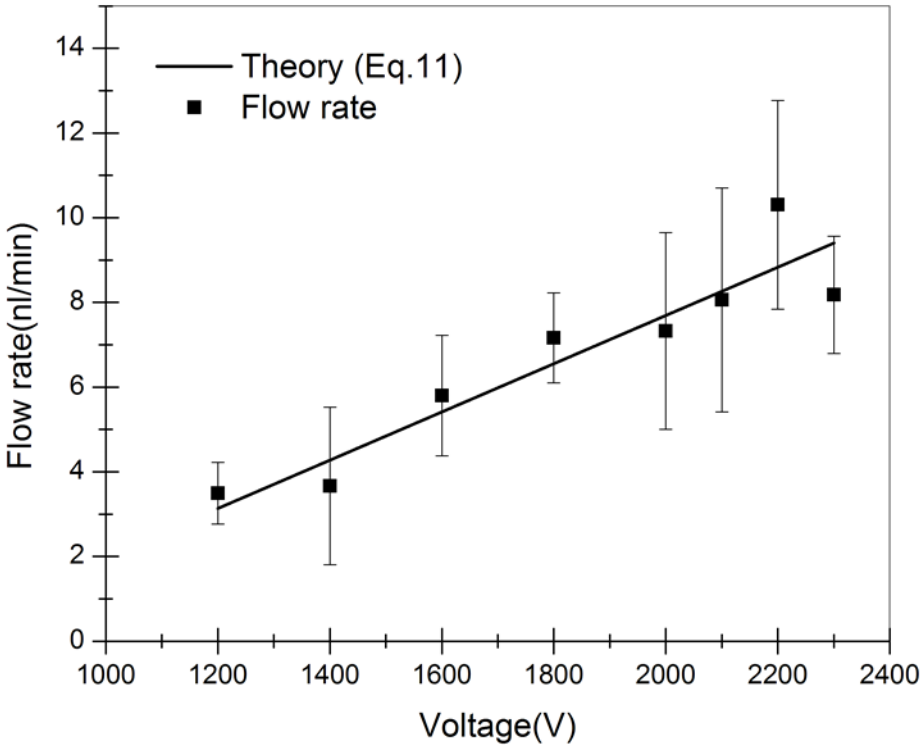

Figure 4-3. The microfluidic loop design was used to measure the micropump flow rate as a function of applied voltage under a known hydrodynamic resistance. The fluid flow rate varies linearly with the applied voltage and shows good agreement with the theoretical pump curve given by Eq. (11).

.

4.5.2 Pump Characterization: The T-Junction Design

To measure pump pressure, experiments were performed at the channel junction within a microfluidic T-channel (Figure 4-2b). A micropump was fabricated within each of the channel inlets. Two solutions of deionized water were labeled with different colored fluorescent dyes, and each was then driven into separate fluid inlets with a constant pressure source. When the applied pressures were equal, a liquid interface was

observed to form at the centerline within T-junction, shown in Figure 4-2c. Similar to the microfluidic loop, the total flow rate in the main channel was determined by computing the average velocity of suspended particles trajectories, and multiplying by the microchannel cross-section area. Each of the two fluid inlet stream then comprised 50% of the total flow rate within the main channel. With each fluid inlet flow rate known, a single micro pump was activated to induce fluid flow in the direction opposing the externally applied pressure driven flow. The resulting EO-induced counter flow acted against the external flow field, and reduced the total flow rate within the microchannel. Under a critical voltage, the micro pump flow rate completely balanced the externally applied flow rate. The interface position became fixed at the entrance of the active pumping channel and flow from this fluidic channel ceased (Figure 4-2d). Using Eq. 9, the experimentally determined flow rate was combined with the hydrodynamic resistance across the microchannel length (Eq. 10) to calculate the induced pressure drop between pumping area and outlet, which was equal to the pressure drop created by the micro pump. This process was then repeated over a range of applied pressures. Therefore, using a microchannel T-junction we are able to experimentally measure the maximum output pressure of the micropump as a function of voltage. The resulting pump pressure vs. voltage dataset is shown in Figure 4-4. The experimentally observed pumping pressure varies linearly from 16 Pa – 31 Pa for applied voltages ranging from 1.4 - 2.0 kV. Eq. (6) was used to predict pressure as a function of applied voltage. The theory is plotted in Figure 4-4 and shows good agreement with our experimental data. For this microchannel geometry, the threshold operation voltage (screening potential) was experimentally determined to be 600 V.

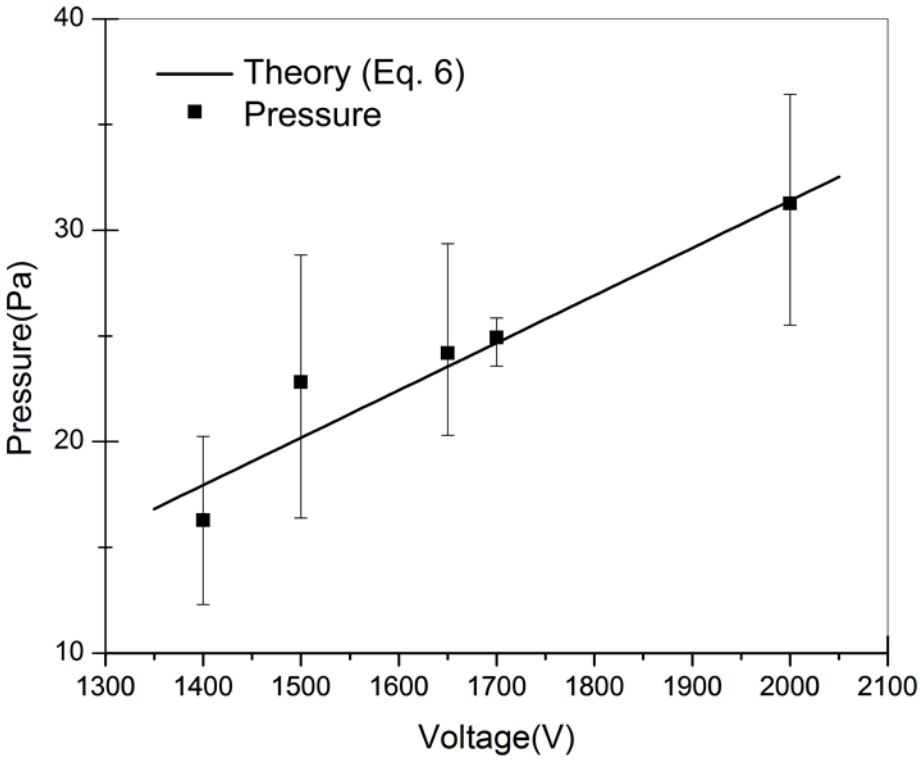

Figure 4-4. The T-junction was used to measure the maximum pressure generated by micropump when net fluid flow is ceased. The output pressure varies linearly with the applied voltage and matches the theoretical pump curve given by Eq. (6).

4.5.3 Microfluidic Liquid Manipulation

We have presented two different microfluidic devices capable of quantifying the working performance of on-chip electrokinetic micro pumps. In this section we demonstrate the fluidic processing capability of these gallium pumps. Specifically, we present results showing their capacity to route fluid flow within a microchannel network

and to create “plugs” of solute for fluid metering and on-chip electrophoresis applications.

4.5.3.1 Fluid Routing

The goal here is to demonstrate the ability to route fluid flow into a different path within the microfluidic network, and then deliver this flow to a specific outlet stream. To accomplish this objective, fluidic routing was performed using an open access microfluidic loop configuration with two inlets (IN1, IN2), three outlets (O1 – O3), and four integrated pumps (P1 – P4), as shown in Figure 4-5. Each loop corner is highlighted with a dotted box and imaged to demonstrate fluid routing. IN1 and IN2 were used to deliver separate fluid streams, each labeled with a different fluorescent dye (colored green or red), using an external constant pressure source. The device was primed and allowed to reach steady state. When no pumps were active, the two solutions split evenly within the fluidic network; red buffer was driven to O1, green buffer was sent to O2, and a combination of two colors flowed out of O3 (Figure 4-5b). To re-route flow, P1 was activated to work against the externally applied pressure. Shown in Figure 4-5c, red colored fluid reverses direction and is driven into O1, while the green stream flows out of O3.

This experiment simulates a fluid delivery and control unit, which can be applied to LOC systems, like sequential sample injection, buffer delivery or product collection. By introducing programmable control to each pumping unit on-chip, the flow direction in each stream can become controllable and predictable in LOC systems. We are able to deliver target streams into specific outlets, which can potentially be used to alter the fluid network to discharge waste or for delivering user-defined amounts of washing buffer to

different on-chip destinations. In the next section, we demonstrate the ability to use on-chip automated control with these micro pumps for microfluidic liquid metering.

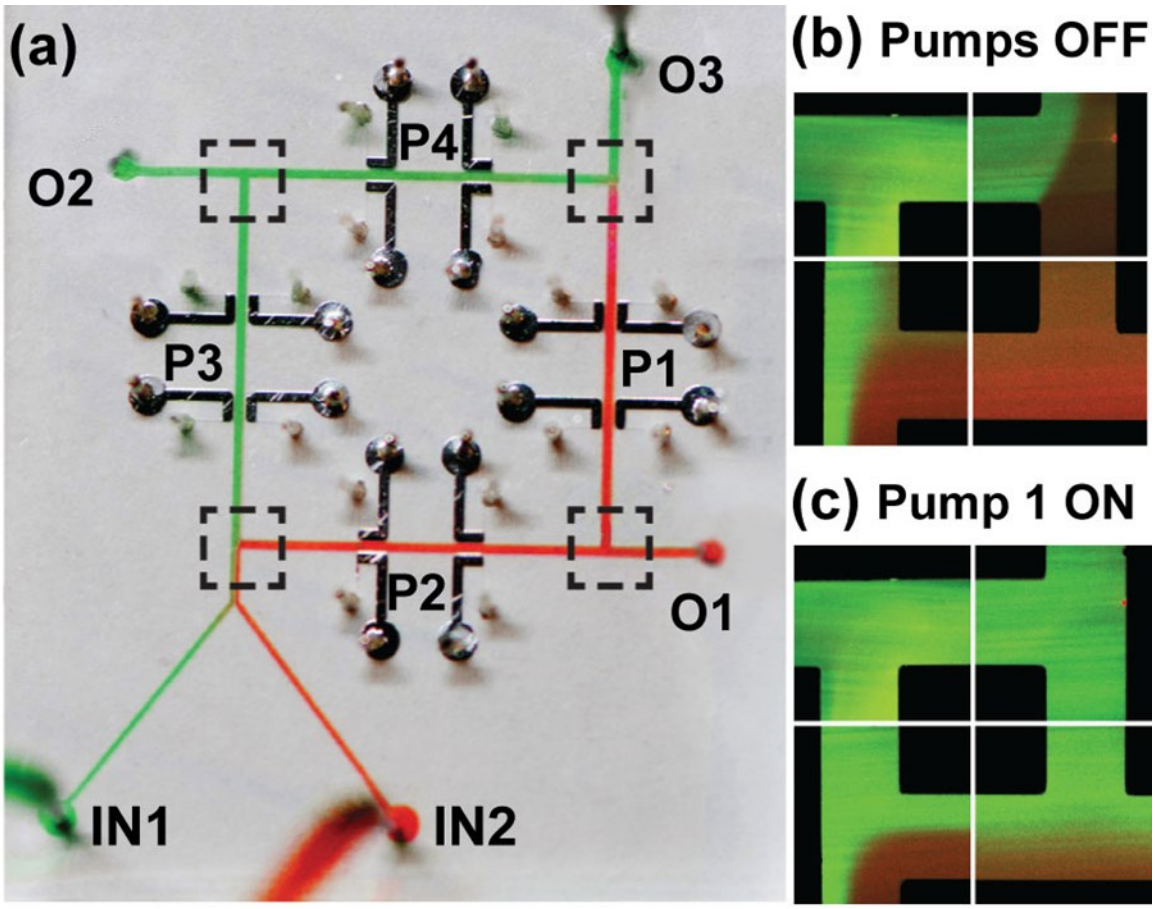

Figure 4-5. (a) A microfluidic loop with two inlets (IN1, IN2) and four integrated micropumps (P1-P4) is used to route fluid flow to different channel outlets (O1-O3). Each loop corner is highlighted with a dotted box and imaged to demonstrate fluid routing. (b) When no pumps are active fluid enters and exits the loop symmetrically. (c) The right-most pump is activated to eliminate the flow rate of red-dyed fluid at O3.

4.5.3.2 On-Chip Sample Injection

There has been recent interest in developing microfluidic methods to deliver sample plugs for microchip capillary electrophoresis (MCE).[37] Traditional small sample injection strategies are classified into two categories, electrokinetic[38] and hydrodynamic.[39] Electrokinetic injection is the most commonly used technique in microchip capillary electrophoresis (MCE) due to its independence of an external pressure source. The approach typically utilizes two different electro-osmotic fluid flows within a cross-shape microchannel device. First, EO flow is used to prime a sample solution across a single fluid channel. A second EO flow is then initiated perpendicular to the sample flow channel, which generates a small solute plug for further downstream analysis. Here, we demonstrate this process using a series of automated on-chip gallium-based micropumps. The plug generation device consists of a cross-shaped microchannel with three integrated on-chip micropumps (P1 – P3). The pumps are fabricated in each of the three arms of the cross, as shown in Figure 4-6. The left-most fluid stream was primed with a green fluorescent buffer, which we interpret here as the sample solution, while a red dyed fluid filled the buffer channel. To generate a controlled plug of solute, we activated P1 to drive buffer down the channel while P2 and P3 were simultaneously switched on and off periodically using a series of computer controlled high voltage relays. This impulse loaded a sample plug into the buffer stream. Shown in Figure 4-6b, the resulting off/on switching of the gallium micro pumps generates a series of solute plugs within the main flow channel. With the ability to automate the gallium micropump operation, this plug generator has the potential to serve as an upstream sample preparation unit for microfluidic capillary electrophoresis.

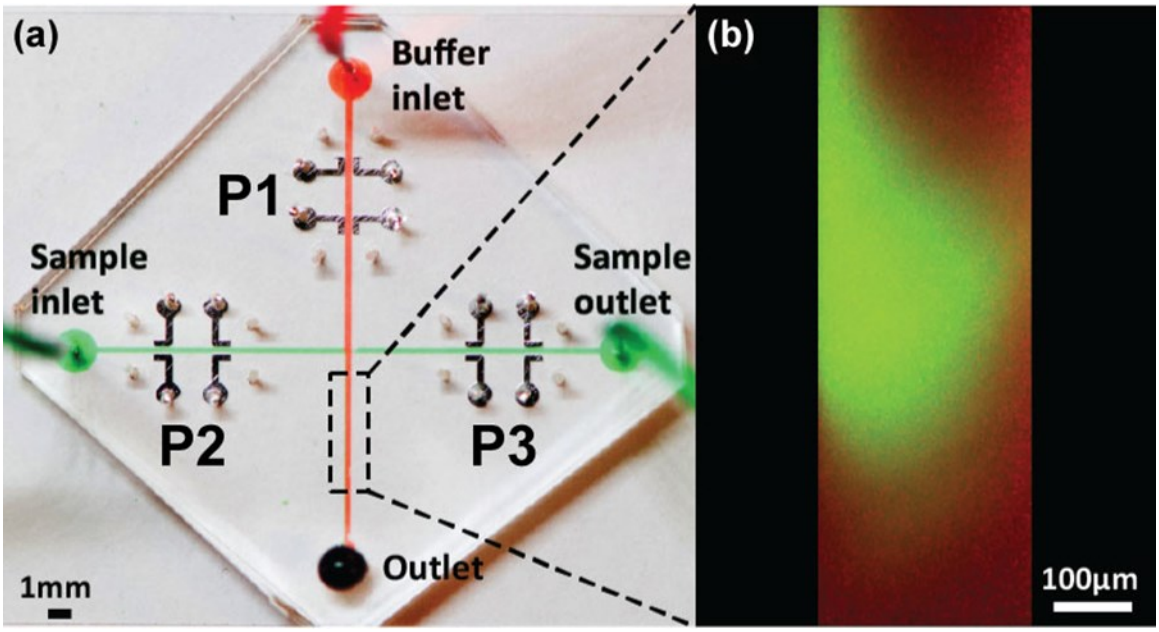

Figure 4-6. A cross-channel device with three integrated pumps (P1-P3) is used to generate plugs of solute. (a) Buffer is driven down a main channel from the channel inlet. Pumps P2 and P3 within the sample channel are pulsed on-off to generate a sample plug within the buffer channel.

4.6 Conclusions

In conclusion, we have demonstrated a new metal-based contactless DC electro-osmotic micro pump capable of on-chip microfluidic pumping, routing and metering. The pump is driven by gallium metal electrodes integrated directly into the sidewalls of the flow channel, separated by a thin micron-scale PDMS membrane. The PDMS membrane serves as an insulating barrier and prevents electrodes from being in direct contact with the working fluid. A high voltage (1.2 – 2.3 kV) DC electric field is utilized to overcome the induced ionic screening potential at the membrane, and drive a net fluid flow. The flow is electro-osmotic and scales linearly with the applied voltage. The maximum flow

rates and pressures generated by the pump using DI water as a working buffer are 10 nL/min and 30 Pa, respectively. We measured the pump pressure and flow rate as a function of voltage using two different microfluidic geometries – a microfluidic loop and a T-shape channel. The resulting pump curves agree well with the presented electro-osmotic flow model. Finally, we demonstrate the ability for these micro pumps to route fluid flow and generate controlled plugs of solute within a microfluidic channel network.

One limitation of this current contactless design is the potential for low efficiency operation due to the electrically resistive PDMS membranes. These pumps also suffer from counter ion screening, which currently limits their use to low conductivity buffers. With our current design, the maximum operational conductivity where fluid flow is observed is 0.1 mS/cm. This number still falls below typical values associated with physiological buffers. Current research is underway on integrating conductive additives into the PDMS membranes in order to overcome these limitations.

Reference:

1 S. J. Lee and S. Y. Lee, Applied Microbiology & Biotechnology, 2004, 64, 289.

2 K. Seiler, Z. H. Fan, K. Fluri and D. J. Harrison, Anal. Chem., 1994, 66, 3485-3491.

3 J. G. Smits, Sensors and Actuators A: Physical, 1990, 21, 203-206.

4 Friend,M.K.Tan and L.Y.Yeo and J.R., EPL (Europhysics Letters), 2009, 87, 47003.

5 J. W. Kwon and E. S. Kim, Sensors and Actuators A: Physical, 2002, 97–98, 729-733.

6 T. Thorsen, S. J. Maerkl and S. R. Quake, Science, 2002, 298, 580-584.

7 R. Gorkin, J. Park, J. Siegrist, M. Amasia, B. S. Lee, J. Park, J. Kim, H. Kim, M. Madou and Y. Cho, Lab Chip, 2010, 10, 1758-1773.

8 L. Y. Yeo and J. R. Friend, Annu. Rev. Fluid Mech., 2014, 46, 379-406.

9 C. L. Rice and R. Whitehead, J. Phys. Chem., 1965, 69, 4017-4024.

10 G. Garcia-Schwarz, A. Rogacs, S. S. Bahga and J. G. Santiago, Journal Of Visualized Experiments: Jove, 2012, , e3890.

11 M. O. A. Sommer and S. Larsen, Journal of Synchrotron Radiation (Wiley-Blackwell), 2005, 12, 779.

12 K. N. Han, C. A. Li and G. H. Seong, Annual Review of Analytical Chemistry, 2013, 6, 119-141.

13 Z. R. Gagnon, Electrophoresis, 2011, 32, 2466.

14 C. B. Rohde, C. Gilleland, C. Samara and M. F. Yanik, Life Science Systems and Applications Workshop, 2009. LiSSA 2009. IEEE/NIH, 2009, , 52-55.

15 J. G. S. D J Laser and, J Micromech Microengineering, 2004, 14, R35.

16 Brian D Iverson and Suresh,V.Garimella, J Micromech Microengineering, 2009, 19, 055015.

17 P. Foroughi, Y. Zhao, J. Lawler and M. M. Ohadi, AIP Conference Proceedings, 2005, 746, 46-54.

18 Z. Gagnon, J. Mazur and H. Chang, Lab Chip, 2010, 10, 718-726.

19 J. C. T. Eijkel, C. Dalton, C. J. Hayden, J. P. H. Burt and A. Manz, Sensors Actuators B: Chem., 2003, 92, 215-221.

20 S. Pal, A. Datta, S. Sen, A. Mukhopdhyay, K. Bandopadhyay and R. Ganguly, J Magn Magn Mater, 2011, 323, 2701-2709.

21 H. Moon, S. K. Cho, R. L. Garrell and C. ". J. Kim, J. Appl. Phys., 2002, 92, 4080.

22 Z. R. Gagnon and H. Chang, Appl. Phys. Lett., 2009, 94, 024101.

23 M. -. Nguyen, S. A. Grigoriev, A. A. Kalinnikov, A. A. Filippov, P. Millet and V. N. Fateev, J. Appl. Electrochem., 2011, 41, 1033-1042.

24 B. G. Hawkins and B. J. Kirby, Electrophoresis, 2010, 31, 3622.

25 H. Moncada-Hernandez, J. L. Baylon-Cardiel, V. H. Pérez-González and B. H. Lapizco-Encinas, Electrophoresis, 2011, 32, 2502.

26 A. Gencoglu, F. Camacho-Alanis, V. T. Nguyen, A. Nakano, A. Ros and A. R. Minerick, Electrophoresis, 2011, 32, 2436-2447.

27 S. Sridharan, J. Zhu, G. Hu and X. Xuan, Electrophoresis, 2011, 32, 2274.

28 J. P. Urbanski, T. Thorsen, J. A. Levitan and M. Z. Bazant, Appl. Phys. Lett., 2006, 89, 143508.

29 V. Studer, A. Pepin, Y. Chen and A. Ajdari, Analyst, 2004, 129, 944-949.

30 M. Sano, R. Gallo-Villanueva, B. Lapizco-Encinas and R. Davalos, Microfluidics and Nanofluidics, 2013, 1-11.

31 P. Wang, Z. Chen and H. Chang, Sensors & Actuators B: Chemical, 2006, 113, 500.

32 B. Kirby, Micro- and nanoscale fluid mechanics : transport in microfluidic devices, Cambridge University Press, New York, 2010.

33 J. Nguyen, Y. Wei, Y. Zheng, C. Wang and Y. Sun, Lab Chip, 2015, 15, 1533-1544.

34 C. Morris and F. Forster, Exp. Fluids, 2004, 36, 928-937.

35 M. J. Assael, I. J. Armyra, J. Brillo, S. V. Stankus, J. Wu and W. A. Wakeham, J. Phys. Chem. Ref. Data, 2012, 41, 033101-16.

36 L. Wang, M. Zhang, M. Yang, W. Zhu, J. Wu, X. Gong and W. Wen, Biomicrofluidics, 2009, 3, 034105.

37 L. Fu and C. Lin, Anal. Chem., 2003, 75, 5790-5796.

38 E. S. Roddy, H. Xu and A. G. Ewing, Electrophoresis, 2004, 25, 229-242.

39 C. Lin, C. Chen, C. Lin and S. Chen, Journal of Chromatography A, 2004, 1051, 69-74.

5 Contactless Microfluidic Pumping Using Microchannel Integrated Carbon Black Composite Membranes[c]

5.1 Overview

The ability to pump and manipulate fluid at the micron-scale is a basic requirement for microfluidic platforms. Many current manipulation methods, however, require expensive and bulky external supporting equipment, which are not typically compatibale for portable applications. We have developed a contactless metal electro-osmotic micropump capable of pumping conductive buffers. The pump operates using two pairs of gallium metal electrodes, which are activated using an external voltage source, and separated from a main flow channel by a thin micron-scale PDMS membrane. The thin contactless membrane allows for field penetration and electro-osmotic (EO) flow within the microchannel, but eliminates electrode damage and sample contamination commonly associated with traditional DC electro-osmostic pumps that utilize electrodes in direct contact with the working fluid. Our previous work has demonstrated the effectiveness of this method in pumping deionized water. However, due to the high resistivity of PDMS, this method proved difficult to apply towards manipulating conductive buffers. To overcome this limitation, we fabricated conductive carbon black (CB) powder directly into the contactless PDMS membranes. The increased

[c] Reprinted with permission from Fu, X; Fu, X., Gagnon, Z., "Contactless Microfluidic Pumping Using Microchannel-integrated Carbon Black Composite Membranes", Biomicrofluidics, (2015), 9, 054122.

electrical conductivity of the contactless PDMS membrane significantly increased micropump performance. Using a microfludic T-channel device and an electro-osmotic flow model we determined the influence that CB has on pump pressure for CB weight percents varying between 0 and 20. The results demonstate that the CB increases pump pressure by two orders of magnitude and enables effective operations with conductive buffers.

5.2 Introduction

Microfluidic pumps, that route and manipulate fluid flow in microchannels, are essential components for lab-on-a-chip systems.[1] On-chip, they are typically integrated with other critical components, such as microvalves, mixers, separators, sensors and detectors, to create complete micro total analysis systems (uTAS) for processing small volumes of fluid in applications including drug screening, medical diagnostics, chemical analysis, and environmental monitoring. To carry out complex on-chip experiments like these, microfluidic platforms are used to control control on-chip fluidic pumping, valving, mixing and routing.[2,3] For example, microfluidic large scale integration (LSI) uses microchannel networks with integrated pressure-actuated elasomeric pumps and valves to control, route and mix fluid in channels for on-chip fluidic processing.[4] Others have used centrifugal forces[5], surface acoustic waves[6], and electrical forces to perform fluidic metering mixing, and aliquoting for applications including DNA extraction, plasma separation[7], cell lysis[8], protein crystallization[9], immunoassays[10], and single cell analysis[11].

The majority of these microfluidic platforms, however, require large and often expensive external actuation equipment for operation, which can confine their usefulness

to the laboratory bench-top. The development of more portable platforms is therefore an important area of microfluidic research. LSI, for example, requires bulky external computer controlled vacuum or pressure sources for component actuation. Centrifugal-based microfluidics[5] can drive fluidic routing, mixing, and metering on rotating substrates with on-chip valves and channels, but the motor required for actuation is expensive, and this platform lacks flexibility; the spinning chip cannot be interfaced with external electrical readouts or sensors. Platforms based on surface acoustic waves (SAW)[12] and electrical forces[13] offer effective an means to transport liquid on-chip, but require expensive and often large electrical equipment. In terms of developing microfluidic systems for point-of-care diagnostics, personalized medicine, and environmental monitoring, developing more portable fluidic manipulation technology is an important step towards reaching this goal.

Improved methods for microfluidic pumping and valving are helping to increase the portability of these devices. In general, microfluidic pumps can be categorized based on the mechanism for driving fluid flow. Displacement pumps utilize moving parts such as membranes or valves to drive fluid motion.[14] At the microscale, however, they require complex fabrication processes and can suffer from mechanical failure. Kinetic pumps, on the other hand, do not require moving parts, and operate by converting kinetic sources into fluid momentum to drive flow. Common kinetic actuation methods include electrokinetic[15], magnetohydrodynamic[16], electrochemical[17], electrothermal[18],[19] and electrowetting [20].

Electrokinetic (EK) flows are a popular class of low-volume, low-power micropumps, and can serve as a useful alternative to mechanical micro pumps.[13] EK

pumps, however, typically require direct contact between electric field-generating electrodes and a working fluid. When a direct current (DC) voltage is applied, Faradaic reactions occur at each electrode surface, which can lead to uncontrolled electrothermal flow, electrode damage, and sample damage from pH generation and Joule heating. Alternating current electro-osmosis (ACEO) pumps can alleviate some of these drawbacks. ACEO pumps do not suffer from Faradaic reactions, and are capable of generating high velocities on-chip for low conductivity aqueous electrolytes. Typically, however, EO pumps require direct contact between electric field-generating electrodes and a working fluid. When a direct current (DC) voltage is applied, Faradaic reactions occur at each electrode surface, which can lead to uncontrolled electrothermal fluid flow, electrode damage, and sample damage from pH generation and Joule heating. As opposed to DC driven EO flow, alternating current (AC) electro-osmotic pumps can alleviate some of these drawbacks. ACEO pumps do not suffer from Faradaic reactions, and are capable of pumping low conductivity aqueous electrolytes in microchannels.[21,22] However, they require large microelectrode arrays, which can be expensive and time consuming to fabricate.

Recently, new types of contactless EK (cEK) devices have been developed by Sano et al.[23] In cEK, two conductive electrolyte-filled microchannels serve as liquid electrodes, which are physically isolated form a main flow channel by a thin PDMS membrane. An alternating current (AC) or DC voltage source can penetrate through the membrane and into the main channel without causing Faradaic reactions or buffer contamination issues associated with traditional non-contactless electrode systems. However, cEK liquid based designs lack the necessary features for portable operations

because the liquid electrodes can suffer from evaporation and cannot be reliably transported or stored longterm. Moreover, it is difficult to integrate many electrode devices on a single chip for complex processing; electrodes require fluid injection ports with pipette tips, and have large on-chip footprints. In previous work, we have presented a novel solid metal-based approach for contactless on-chip liquid pumping, routing, and metering. Instead of using liquid electrodes, our micro pump design is based on 3D gallium solid metal electrodes fabricated directly into the sidewalls of microfluidic flow channels, and separated from the active flow region by a thin micron-scale PDMS polymer membrane. In terms of portability, this metal-based design was a significant improvement over previous cEK devices that utilized liquid electrodes. We demonstrated that multiple micropumps could be fabricated and independently operated on a single microfluidic chip with a small external DC power supply and computer controlledler for fluid pumping, mixing, and metering.

One limitation of this contactless design, however, is the high electrical resistance of the PDMS membranes; pumping requires a large kilovolt potential and is limited to low conductivity fluids. In order to drive electro-osmotic (EO) flow, a large kilovolt potential is dropped across the main microchannel. However, due to the insulating PDMS membrane, only 0.2% of the applied potential and was actually delivered into the main channel. This low efficiency limited pumping to electrolytes with conductivities less than 0.1 mS/cm. Electrolytes with greater conductivity could not be pumped because the electric field was not large enough to overcome counter-ion screening at the PDMS membrane wall.

In this work, we present a novel method for integrating conductive PDMS composites directly in specific regions of microchannel sidewalls for significantly improved pumping efficiency. PDMS is an inert polymer that inherently lacks significant conductive properties. However, conductivity can be increased by combining the elastomer with a conducting powder, such as carbon black or silver nanoparticles, to create conductive polymer composites. [24,25] When combined with standard soft lithographic techniques, composites can be pattered into specific structures that are suitable for on-chip applications.[26] For example, Li et al. [27] created an array of conductive PDMS composite posts using PDMS/nickel powder composites to create a sensitive on-chip pressure sensor and Niu et al. [28]uilized soft lithography and PDMS/silver nanoparticles to fabricate arrays of conductive composite-based on-chip circuits. One benefit of this approach is that PDMS composites inherit increased electrical conductivity, but still retain the elastomeric characteristics of PDMS, which allows them to be integrated into microfluidic systems using soft lithography.

Using this approach, we demonstrate a new type of contactless direct current (DC) micro-pump with integrated conductive nanocomposite membranes for significantly improved operation with higher conductive electrolyte buffers. Our micro-pump design integrates carbon black doped conductive PDMS fabricated into the sidewalls of microfluidic flow channels with gallium metal electrodes (Figure 5-1a). Due to the electrical properties of CB, the conductivity of a PDMS membrane can be controlled by mixing PDMS polymer with different weight percents of CB. This technique allows us to customize our micro-pump membrane conductivity depending on the working buffer sample's conductivity.

In the first part of this paper, we present a theoretical model, which combines the governing fluid transport and electrokinetic equations that describe electro-osmotic flow with an electrostatic model for the applied voltage within the main microchannel. We then apply this model to predict the electro-osmotic pressure as a function of applied voltage in a microfluidic "T-shape" device, a design we previously developed and presented to characterize the maximum output pressure of our micropumps. Relations between pumping pressure and CB weight percent (wt%) are then investigated in the second part of this work. Finally, using this pump data, we demonstrate the impact that conductive PDMS composite has on improving pump performance for working with conductive buffers.

5.3 Theory

5.3.1 Electro-osmotic Micropump Pressure and Flowrate

In this section, we derive a theoretical model for relating electro-osmotic flow within a microchannel to the applied voltage drop and the pressure gradient produced by the electro-osmotic pump.[29]

Electro-osmosis is an EK technique for driving flows in microfluidic channels. Solid surfaces tend to develop surface charge when in contact with aqueous liquids. A diffuse electric double layer (EDL) forms to screen this charge, where counter-ions of opposite sign are attracted to the surface and co-ions are repelled. The resulting EDL possesses a non-zero charge density and its thickness depends on the ionic strength of the electrolyte; typical EDL thicknesses range from nanometers for mM electrolytes to microns for low conductive μM electrolytes. Because the EDL possess a non-zero charge

density, an external electric field applied tangential to the charged surface forces the EDL into electro-osmotic flow (EOF). Assuming that the electric field is uniform, the flow is unidirectional, and there is no applied pressure gradient, the Stokes equations can be written as

$$0 = \mu \frac{\partial^2 u}{\partial y^2} - \varepsilon \frac{\partial^2 \phi}{\partial y^2} E_{wall} \quad (1)$$

whereμ, ε, and E_{wall} are the fluid viscosity, electrolyte permittivity, and applied tangential electric field at the channel wall, respectively. Eq. (1) can be integrated with a no slip condition at the channel wall (y=0) and a far-field condition $\phi \to 0$ that as $y \to \infty$ to give:

$$u_{slip} = \frac{\varepsilon E_{wall}}{\mu}\left(\phi - \phi_{wall}\right) \quad (2)$$

Here, the wall potential, $\phi_{wall} = \zeta e^{-y/\lambda_D}$, exponentially decays over the Debye length, λ_D, and approaches a Smoluchowski slip velocity,

$$u_{EO} = \frac{\varepsilon E_{wall} \zeta}{\mu} \quad (3)$$

where ζ is the zeta potential at the surface of the microchannel. For the case where a micropump must drive a flow against a hydrodynamic load, a backpressure is generated and the net fluid flow is reduced. For a slot-shaped microchannel where the width is much larger than the height, the net flow rate is a linear combination of EO and pressure driven back flow,

$$Q = \frac{2wd^3}{3\mu}\left[\frac{\partial P}{\partial x}\right] - 2wd\frac{\varepsilon E_{wall}\zeta}{\mu} \quad (4)$$

For an applied voltage, ΔV , dropped over an electrode separation length L_E, the electric field at the wall is $\Delta V / L_E$. The back pressure gradient varies linearly and can be written as $\Delta P / L_E$. The maximum pressure produced by the EO pump (P_{max}) occurs when Q = 0, which is the case for a closed microchannel, and is:

$$\Delta P_{\max} = -\frac{3\mu u_{EO}}{d^2}\Delta V \quad (5)$$

5.3.2 Voltage Drop Across a Carbon Black PDMS Composite Membrane

Contactless micropumps follow the same electro-osmotic principles as traditional EO pumps with external metal electrodes, however, the high electrically resistive nature of the insulating PDMS membranes reduce the effective voltage (ΔV_{eff}) within the microchannel from that of the total potential applied (ΔV_{total}). We apply a simple Ohmic current model to determine this relationship. The effective voltage drop across the working fluid can be written as:

$$\Delta V_{eff} = \Delta V_{total}\frac{R_{fluid}}{R_{total}}, \quad (6)$$

where $R_{total} = R_{CB} + R_{fluid}$.

When a DC voltage is dropped across the contactless PDMS membrane, counter ions in the working electrolyte will accumulate at the PDMS-liquid interface, and create an induced screening potential (ϕ_s) which will reduce the magnitude of the electrostatic

field in the main channel. The magnitude of this screening effect is a function to the applied electric field and electrolyte counter ion concentration. If the ion concentration is large enough, the applied field will be completely screened from the microchannel, and no electro-osmotic flow will be observed. If the applied voltage is large enough and able to exceed the screening potential, however, an electric field will penetrate into the bulk and impart an electro-osmotic slip velocity at the PDMS membrane surface.[29]

A more general relation between effective and total potential applied must take into account this screening potential:

$$\Delta V_{eff} = \Delta V_{total} \frac{R_{fluid}}{R_{total}} - \phi_s \quad (7)$$

Under conditions where the net pump flowrate is zero, Eq. (7) can be combined with Eq. (5) to quantify the maximum pump pressure. In this work, we experimentally determine the screening potential from our experimental pump curves using a microfluidic T-channel device.

5.4 Materials and methods

Here, we describe the fabrication and operation of a contactless CB micro pump and present a novel process for patterning conductive PDMS composite membranes within microchannel sidewalls, and integrating these composites with 3D gallium metal electrodes. We then demonstrate how to use a microfluidic "T-shape" device for measuring the pressure generated by the pump.

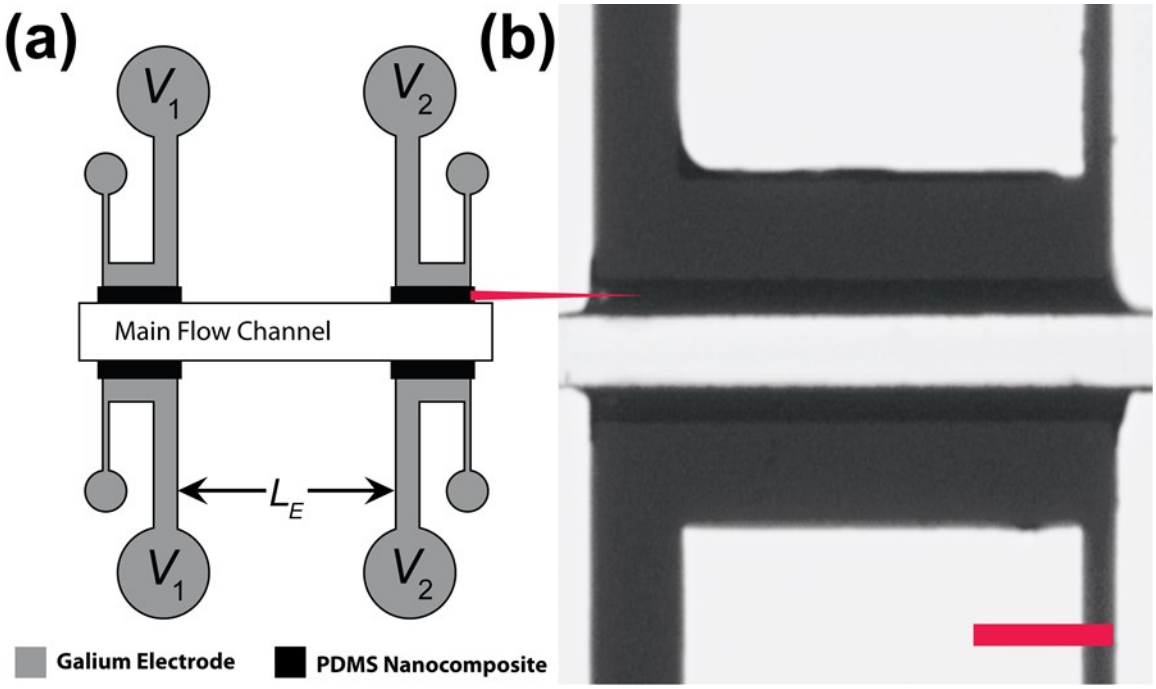

Figure 5-1. Schematic of a gallium metal contactless micropump with integrated PDMS carbon black membranes. (a) A top view of a single pumping device. Each micropump contains four gallium electrodes separated from the main channel by a thin PDMS-carbon black nanocomposite membrane. (b) A micrograph of a pair of electrodes surrounding a microchannel. The nanocomposite is directly integrated into the microchannel sidewalls. Scale bar, 200μm.

5.4.1 Microfluidic Chip

Each microfluidic pump, as shown in Figure 5-1(a), consists of a main flow channel and four separate electrode-containing channels. The electrode channels are filled with gallium metal, each of which are fabricated directly against a patterned region of micron-thick PDMS/CB composite membrane [Figure 5-1(b)]. To fabricate the composite membranes at specific regions within a microfluidic channel sidewall, we employed a novel multistage soft lithographic process, shown in the process flow diagram in Figure 5-2(a-d). First, a negative photoresist, SU-8 3050 (Microchip Corp.),

was used to fabricate a soft lithographic mold with a main flow channel (300 um wide and 50 um high) and four gallium electrode channel (900 um wide) [Figure 5-2(a)]. To create conductive PDMS composite membranes, carbon nanopowder (Sigma-Aldrich, 633100) was combined with a 1:10 weight ratio of PDMS elastomer and curing agent and mechanically mixed in a centrifugal mixer (Thinky, ARM 310) at 2000 RPM for 30 seconds. The carbon powder was added at different wt%, ranging between 5% - 20%, in order to study the influence of PDMS composite resistivity on device performance. The nanocomposite PDMS gel was injected into each gap between the electrode channel and the main flow channel using a 1 mL plastic syringe [Figure 5-2(b)]. Excess gel was immediately removed from the SU-8 mold using a razor blade and a 1:10 mixture of PDMS elastomer and curing agent was poured atop the mold and allowed to cure for hour hour at 80 C [Figure 5-2(c)]. The cured PDMS with integrated composite membranes was peeled off the mold. Fluid ports were punched into each channel inlet and outlet using a 0.75 mm biopsy punch (Ted Pella, Inc). The microchannel and a glass coverslip (Fisher Scientific, 12-548-5R) were exposed to oxygen plasma (Jelight, Model 42A), and immediately aligned and sealed under an inverted microscope. The microfluidic chip was baked for 24 hours at 80 C. This post-bond baking step improved the PDMS bond strength and prevented membrane leakage and rupture during pump operation.

To fabricate each 3D metal electrode for a low resistivity electrical connection to the composite membrane, solid gallium metal was melted and injected into the electrode channels of the micro device [Figure 5-2(d)]. First, solid gallium metal (Sigma-Aldrich, 263265) and the PDMS chip were heated to 40C on a hot plate. The melting temperature of gallium is 29.7C, and the newly melted liquid gallium was loaded into a 1 mL plastic

syringe and immediately injected into each electrode side channel. Liquid gallium has a low viscosity (1.37 mPa-s) 30 and the PDMS did not require surface treatment prior to injection. Finally, electrical connections for an external power source were created by inserting 0.75 mm diameter copper wire leads into each electrode injection hole. Figure 5-2(e) shows a micrograph of the final complete micropump after fabrication. An enlarged view highlighting the PDMS nano composite membranes and gallium electrode areas is illustrated in Figure 5-1(b).

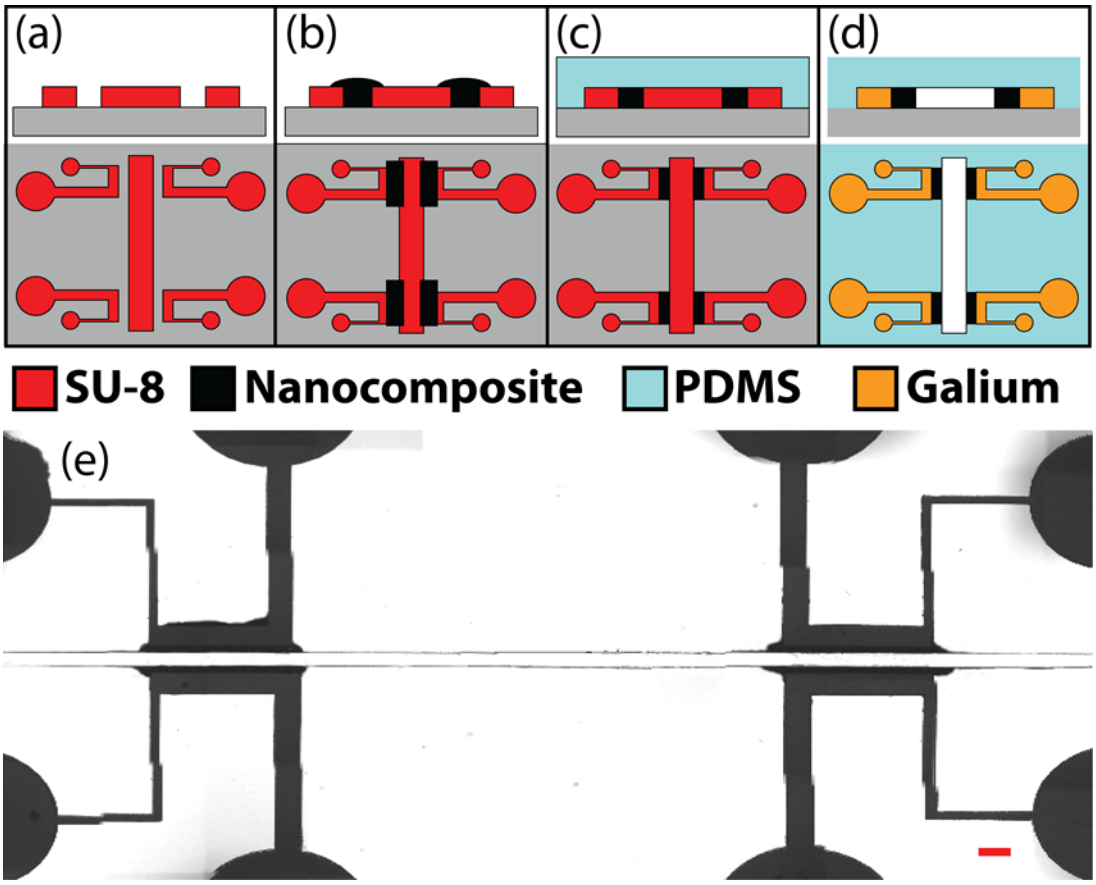

Figure 5-2. Process flow diagram of fabrication process for integrating patterned CB-PDMS membranes into the microchannel sidewalls. (a) Electrode channels and flow channel are defined with a thick film SU-8 photoresist mold. (b) A mixture of CB-PDMS is carefully injected into the gaps between the electrodes and main flow channel. (c)

PDMS elastomer is poured atop the SU-8 mold and allowed to cure. (d) The PDMS device is sealed against a glass substrate and hot liquid gallium metal is injected into the side channels and allowed to cool. (e) Completed device. Scale bar – 200 μm.

5.4.2 Experimental Setup: Measuring Pump Pressure

The final micro pump device, shown in Figure 5-2(e), is composed of four gallium electrodes, separated from the main microchannel by a thin nanocomposite PDMS membrane. To operate the pump, a high voltage power supply (PS325, Stanford Research System, CA) was wired to each electrode pair to create the necessary electric field in the main flow channel; a positive voltage (V1) was delivered to one pair and the other electrode pair was connected to ground (V2), as depicted in Figure 5-1(a). Voltages were applied between 0.80 and 2.5 kV. When the power supply was turned on, the resulting potential difference induced an electro-osmotic flow down the main channel in the direction of the applied electric field.

Using this pump design, we fabricated a microfluidic T-channel device to measure the pump pressure [Figure 5-3(a)]. A micropump was integrated within each of the channel inlets. Two solutions of 2.5mM PBS were labeled with different colored fluorescent dyes, and each was then driven into separate fluid inlets. Experiments were performed by precisely varying the flow rate of each T-junction inlet and observing the impact of the micropump on the flow profile at different applied voltages. This process is detailed below.

For channel flow, fluid velocity can be controlled by regulating either the applied pressure drop or the fluid flow rate. We used both of these methods simultaneously to obtain a precise measurement of the flow rate in the main pump channel. We used a

precision syringe pump (Cole-Parmer, 78-8200C) to deliver fluid into one channel inlet a constant flow rate. A constant pressure source was then applied to drive fluid flow into the second inlet. The pressure was slowly increased and the position of the liquid interface was monitored. When the inlet flow rates were equal, a liquid interface formed at the centerline within the T-junction, shown in Figure 5-3(b). With each fluid inlet flow rate known, a single micro pump was activated within the pressure driven inlet in the direction opposing fluid flow. The resulting EO-induced counter flow acted against the external flow field, and served to reduce the total flow rate within the microchannel. At a critical voltage, the micro pump flow rate completely balanced the externally applied flow rate, and flow from this fluidic inlet ceased [Figure 5-3(c)]. The pump flow rate was combined with the hydrodynamic resistance, R_h, across the microchannel length to calculate ($\Delta P = QR_h$), and used to calculate the induced pressure drop between the pumping area and T-channel outlet. This pressure is equal to the pressure drop created by the micropump. This process was repeated over a range of fluid flow rates and applied voltages. Therefore, using the microfluidic T-junction in combination with an external constant pressure and flow rate source, we are able to experimentally measure the maximum output pressure of the micropump as a function of applied voltage.

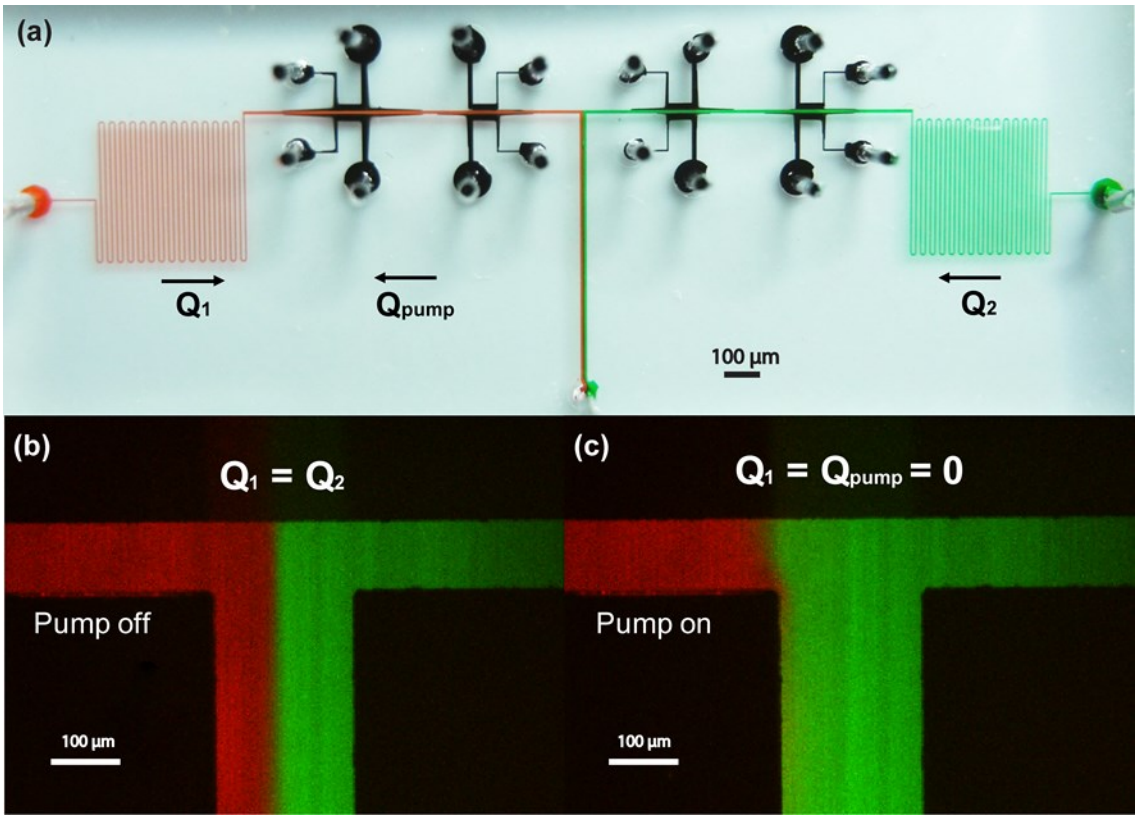

Figure 5-3. (a) Microfluidic T-channel device used to quantify pump pressure. (b) Two fluid streams are driven into the device at a known flowrate. The left-most stream is driven using a constant pressure source, while the right-most is delivered using a constant flowrate source. When no pump is active and the flowrate of each stream is equal, the interface between the two phases is centered within the main flow channel. (c) The left-most pump is activated to complete cancel the pressure driven flow. The flow of this stream ceases and the interface position shifts.

5.4.3 Reagents and Electrical Parameters

The micro pump experiments were conducted using dilute 2.5mM phosphate buffered saline (PBS) and deionized (DI) water as working solutions. Fluorescent dyes were used as convective tracers to the induced EO flow using fluorescent solutions of Alexa Fluor 488 (green) and 594 (red). Because fluorescent dyes are ionic and can influence the electrical conductivity of the fluid, we based our pumping theory on the

experimentally measured electrical conductivity of the fluorescent-labelled 2.5mM PBS (113 μS/cm) and DI water (2 μS/cm) solution. The PDMS zeta potential used in our calculations was based on a conductive buffer at neutral pH: -30 mV. 31

5.4.4 PDMS Composite Resistivity

The electrical resistivity of the PDMS composite membrane is needed to calculate the effective voltage drop across the main flow channel (Eq. 8), and is an important parameter in determining the influence of carbon nano power wt% on our EO pump performance. We measured the PDMS resistivity for each device using a high resistance ohmmeter (Alpha Labs Inc, Model HR2). The PDMS resistivity in our T-channel device was 5.32 x 1010 Ω-cm. The electrical resistivity of PDMS has been reported to be on the order of 10 x 1013 Ω-cm. 32 It is important to note, however, that we have previously observed that PDMS post-bond baking time influences this property; baking time increases from 1 hour - 48 hours, the resistivity of PDMS ascends from 109 to 1013 Ω-cm. Shown in Table 1, we report the electrical resistivity of the PDMS composite membrane at different carbon nano powder weight percent (wt%). We used these values for our theoretical calculations presented in the section below.

5.5 Results and Discussions

5.5.1 Nanocomposite Resistivity on Pump Performance

We first performed experiments using DI water and determined the influence of CB wt% on pump pressure. Figure 5-4 shows the micropump pressure plotted is a function of voltage for different CB wt%. At 20 wt%, the PDMS nanocomposite produced a 40-fold increase in the pump pressure over the PDMS membrane without CB,

leading to pressure results as high as 1200 Pa. Using Eq. (4), we predicted the maximum pump pressure as a function of the applied voltage. The theory, plotted in Figure 5-4, shows good agreement with our experimental data. For this microchannel geometry, the threshold operation voltage (screening potential) was 675 +/- 50 V. In terms of pump performance, CB wt% had very little influence on the micropump screening potential, but delivered significant improvements in pump pressure and efficiency. The pump efficiency, defined here as the ability for an electric potential to penetrate the PDMS membrane ($\Delta V_{eff} / \Delta V_{total}$) is summarized for different CB wt% in Table1. For a micro pump without nanocomposite (a weight ratio of 0%) less than 1% of the total potential applied penetrates into the main flow channel. The addition of 20% CB increases pump efficiency 40-fold, from 0.33% to 13%.

5.5.2 Pump Pressure and Conductive Buffer

Because contactless micro pumps do not require direct contact with working buffers, they have several advantages over traditional DC EK pumps since they do not suffer from Faradiac reactions and electrode decomposition. However, the required high resistivity PDMS membrane leads to low working efficiency, and a high kilovolt voltage is required for successful operation. One significant drawback from this feature is the inability of high resistive designs to to effectively pump conductive buffer. In previous work, we demonstrated successful pumping, routing and metering with contactless pumps without CB additives, but due to the low efficiency the working fluids were limited to low conductivity buffers. Many microfluidic applications, however, are suited for biological purposes and require the ability to process commonly used physiological buffers. Hence, in this section we demonstrate how integrated CB PDMS membranes

extend the contactless micro pump ability to pump buffers with higher electrical conductivity.

Microfluidic “T junction” experiments were repeated with a buffer dilute 2.5mM PBS buffer. Micropump pressure was calculated and plotted against the applied voltage, as shown in Figure 5-5. The theoretical model [Eq. (4)] was applied to the dataset, which agrees well for each working fluid. When chip geometry is fixed, the slopes of output pressure curve are solely determined by the pump efficiency that calculated by $\Delta V_{eff} / \Delta V_{total}$. Higher buffer conductivity (113 μS/cm) reduces the pump efficiency from 13% to 0.28% with 20 wt% CB. Therefore, a much higher potential is required to achieve the same output pressure when operating with more conductive buffers. While CB significantly enhances pump performance for manipulating more conductive buffers, interestingly the screening potential is not signifcantly influenced by the buffer electrical conductivity when we switched working fluids from DI water to PBS and similar screening potentials were experimentally observed even when increasing electrical conductivity by 50-fold. Base on this observation, we speculate that the steric hinderances limit the concentration of counter ions that can electro-migrate and accumulate at the microchannel wall, which leads to a finite screening potential.

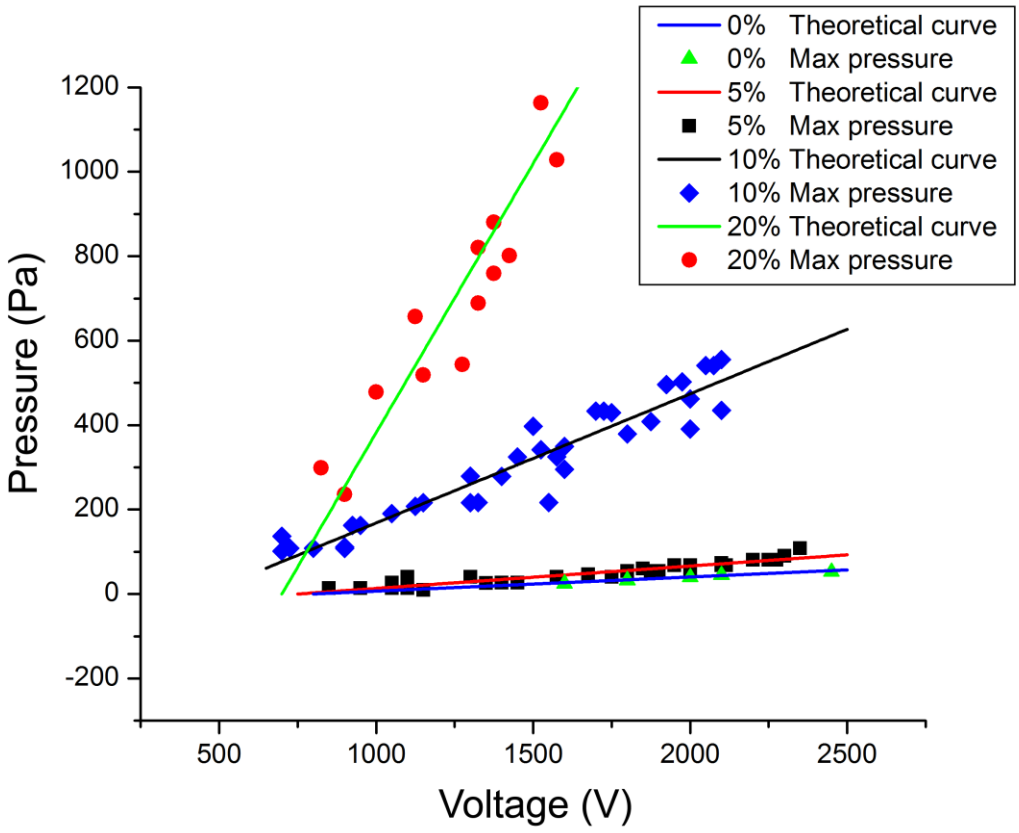

Figure 5-4. The microfludic T-junction was used to measure the maximum pressure generated by the micropump for different CB wt% for DI water. The output pressure varies linearly with the applied voltage and matches the theoretical pump curve given by Eq. (5).

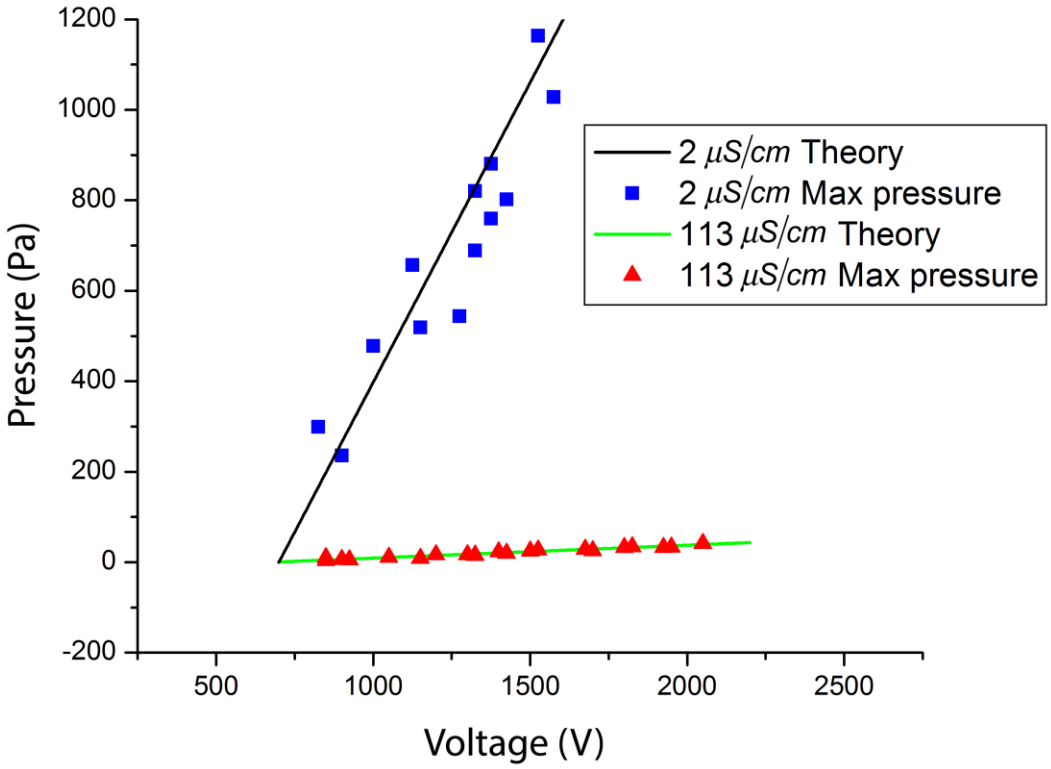

Figure 5-5. Experimental and theoretical pump pressure vs. voltage for DI water (2μS/cm) and PBS (113μS/cm) for 20 wt% CB.

The semilog plot in Figure 5-5 illustrates the influence of CB weight ratio and buffer conductivity on maximum micropump pressure. The voltage was fixed at 2000 V for all four datasets to give a direct comparison between buffer conductivity, CB wt% and the resulting pump pressure. First, high conductivity buffer combined with high resistivity PDMS membranes undermine the pump performance due to the extremely low efficiency of non-CB PDMS membranes; no fluid motion was observed for dilute PBS buffer. Much higher pressures are achieved with the addition of CB to the PDMS

membrane. Shown in the Figure 5-6, pump output pressure increases from 70 Pa to 1600 Pa when CB weight ratio increases from 5% to 20% when DI water is used as a working buffer. The addition of CB enables the successful pumping of conductive PBS buffer, which was not possible using solely PDMS. However, the maximum pump pressure still significantly decreases when compared to DI water from 1600Pa to 80Pa, 480 Pa to 30Pa and 70Pa to 20Pa, for a CB wt% of 20%, 10% and 5%, respectively.

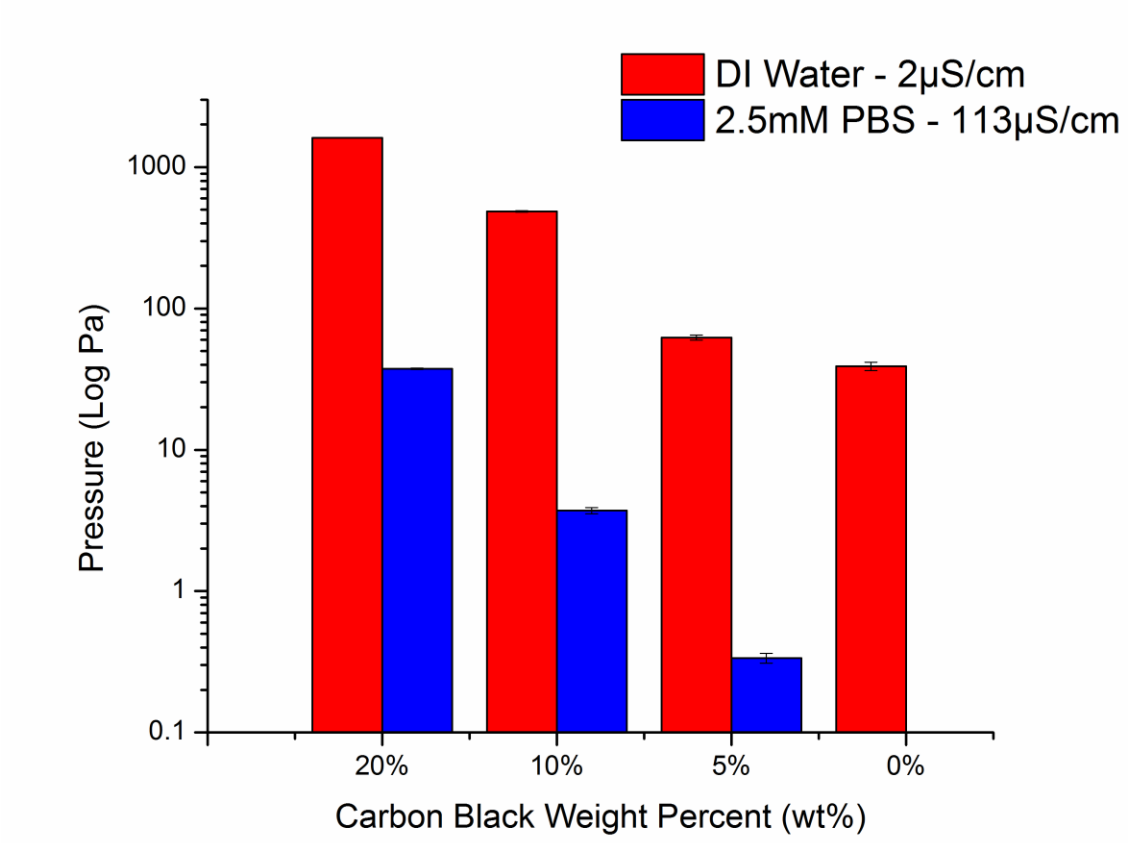

Figure 5-6. Pump pressure for different values of CB wt% for DI water and diluted PBS

5.6 Conclusions

In this work, we have demonstated the ability to pump conductive buffer using a contactless DC electro-osmotic micro pump with conductive carbon black PDMS membranes and solid metal galium electrodes. The PDMS/CB membranes are used to separate the flow channel from solid gallium electrodes, and contain patterned regions of conductive composite for enhanced electric field penetration into the main flow channel. CB membranes with weight ratios of 5%, 10% and 20% were integrated directly into the side walls of flow channel using soft lithography. Using a microfluidic "T" junction shaped geometry we measured the maximum output pumping pressure for different values of CB wt% and investigated this influence on the ability to pump conductive buffer. Under an applied external potential range, (600-2500 V), the resulting pressure curves agree well with our electro-osmotic flow model. This work demonstates that CB conductive membranes greatly enhance contactless micropump performance for conductivity buffer processing. Although the buffer conductivity value reported here still falls below common values for physiological buffer, with further optimization and more conductive additives, the proposed contactless micro pump is a promising tool for portable microfluidic biological buffer processing. Future work will focus on optimizing pump geometry and membrane additives to increase pump efficiency without sacrificing electric field stability and buffer electrolysis, and further applying this work to other electrokinetic applications including dielectrophoresis and electrophoresis.

Reference

1 J. West, M. Becker, S. Tombrink, and A. Manz, Anal. Chem. (2008).

2 S. Haeberle and R. Zengerle, Lab Chip 7, 1094 (2007).

3 D. Mark, S. Haeberle, G. Roth, F. von Stetten, and R. Zengerle, Chem. Soc. Rev. 39, 1153 (2010).

4 J. Melin and S.R. Quake, Annu. Rev. Biophys. Biomol. Struct. 36, 213 (2007).

5 J. Siegrist, R. Gorkin, M. Bastien, G. Stewart, and R. Peytavi, Lab Chip (2010).

6 S.K.R.S. Sankaranarayanan and V.R. Bhethanabotla, J. Appl. Phys. 108, 104507 (2010).

7 Y. Nakashima, S. Hata, and T. Yasuda, Sensor Actuat B-Chem 145, 561 (2010).

8 Y. Sun, T.L. Quyen, T.Q. Hung, W.H. Chin, A. Wolff, and D.D. Bang, Lab Chip 15, 1898 (2015).

9 Billy T C Lau, Chris A Baitz, A. Xiao P Dong, and C.L. Hansen, J. Am. Chem. Soc. 129, 454 (2006).

10 G. Hu, Y. Gao, P.M. Sherman, and D. Li, Microfluid Nanofluid (2005).

11 S. Lindström and H. Andersson-Svahn, Lab Chip 10, 3363 (2010).

12 L.Y. Yeo and J.R. Friend, Http://Dx.Doi.org/10.1146/Annurev-Fluid-010313-141418 46, 379 (2014).

13 C. Zhao and C. Yang, Microfluid Nanofluid 13, 179 (2012).

14 P. Woias, Sensor Actuat B-Chem (2005).

15 T.A. Moore and Y. Lai, in (IEEE, 2008), pp. 157–160.

16 A. Homsy, S. Koster, J.C.T. Eijkel, A. van den Berg, F. Lucklum, E. Verpoorte, and N.F. de Rooij, Lab Chip 5, 466 (2005).

17 S. Sengupta, D. Patra, I. Ortiz-Rivera, A. Agrawal, S. Shklyaev, K.K. Dey, U. Córdova-Figueroa, T.E. Mallouk, and A. Sen, Nature Chemistry 6, 415 (2014).

18 J. Wu, M. Lian, and K. Yang, 90, 234103 (2007).

19 Z.R. Gagnon and H.-C. Chang, 94, 024101 (2009).

20 R.B. Fair, Microfluid Nanofluid 3, 245 (2007).

21 Z. Gagnon and H.-C. Chang, Electrophoresis 26, 3725 (2005).

22 Z. Gagnon, J. Mazur, and H.-C. Chang, Lab Chip 10, 718 (2010).

23 M.B. Sano, R.C. Gallo-Villanueva, B.H. Lapizco-Encinas, and R.V. Davalos, Microfluid Nanofluid 15, 599 (2013).

24 H.-S. Chuang and S. Wereley, J. Micromech. Microeng. 19, 045010 (2009).

25 X. Gong and W. Wen, Biomicrofluidics 3, 012007 (2009).

26 C.-X. Liu and J.-W. Choi, J. Micromech. Microeng. 19, 085019 (2009).

27 Q. Ouyang, Microelectronic Engineering 87, 1266 (2010).

28 X. Niu, S. Peng, L. Liu, W. Wen, and P. Sheng, Adv Mater 19, 2682 (2007).

29 X. Fu, N. Mavrogiannis, S. Doria, and Z. Gagnon, Lab Chip 15, 3600 (2015).

30 M.J. Assael, I.J. Armyra, J. Brillo, S.V. Stankus, J. Wu, and W.A. Wakeham, Journal of Physical and Chemical Reference Data 41, 033101 (2012).

31 P. Wang, Z. Chen, and H.-C. Chang, Sensor Actuat B-Chem 113, 500 (2006).

32 V. Studer, A. Pépin, Y. Chen, and A. Ajdari, Analyst 129, 944 (2004).

6 Building a Low-cost Microfluidic Sensor: On-chip Pressure and Flow Rate Measurements with Integrated Carbon Black Membranes

6.1 Overview

Pressure sensors and flow meters play a key role in microfluidic device operation and control. Most commercial available pressure sensors and flow meters are bulky, expensive and only work externally. To realize the real point of care microfluidics, on-chip pressure and flow monitoring are highly desired. In this chapter, we present an on-chip cost-efficient piezoresistive microfluidic sensor that is capable of both pressure and flow rate measurements. Compared to the current flow meters that cost more than 1000 USD per piece, the new sensor has a fabrication cost that is less than two USD. The sensor utilizes the carbon-PDMS films design associated with an impedance analyzer to read local pressure inside microfluidic channel. The elastic carbon-PDMS membranes serve as a transducer to convert pressure information into electrical signal. By integration multiple pressure sensing units, we are able to conduct flow rate measurement in the same time. Moreover, this design allows the sensor to be integrated to any microfluidic devices without interrupting the fluidic flow, which significantly facilitates on-chip sensor integration. In this chapter, we first introduce an overall background of on-chip pressure sensors and flow meters, the role they play in a completed microfluidic system. Then we demonstrate the fabrication process of sensor device and experiment setup. Operation frequency of impedance analyzer is optimized before we characterize the

pressure sensor to build a linear relation between local pressure and impedance. Lastly, we construct the actual flow meter with two integrated pressure sensing units and compare the measured flow rate to another commercial flow meters.

6.2 Introduction

The miniaturizing technologies known as the lab-on-chip (LOC) are popular among biologists and chemists because of their small size, low sample consumption, high portability, and ability to produce results quickly. The LOC techniques feature sample-in-and-result-out designs and have been widely adapted to diagnostic and analytical instruments. Advances in microfabrication allow the integration of extra functions into current LOC designs, including droplet generation, cell trapping, and biomolecules separation (1-3). But it also leads to increased chip complexity and makes acquiring reliable test results difficult as more precise hydrodynamic pressure control is required. Flow meters and pressure sensors have been developed to provide real-time monitoring and feedbacks during the operation of LOC devices. However, the high cost of external sensors, typically around a couple of thousands USD, greatly undermines their accessibility in LOC applications.

The bulky sensor size also leads to the emergence of integrated LOC sensors utilizing different signal transducing methods. Significant progress has been made in developing heat transfer-based sensors (4-7), mechanical flow sensors (8-11), acoustic-ultrasonic flow meter(12), particle tracing with optical detectors (13), time-of-flight detector(14) and flapping of a planar jet (15). Among current sensor technologies, piezoresistive transistor, a sensor that relies on pressure induced electric

property changes, features a fine sensitivity, a wide operation range, as well as a simple signal transduction mechanism between the mechanical and the electrical domain.

To create piezoresistive sensors, carbon nanocomposite is an ideal fabrication material due to the extraordinary electric conductivity and the inert chemical properties. Studies characterizing carbon nanocomposite's electric properties and pressure responses have been reported since early 2000 (16, 17). Grow et al first investigated the electromechanical response of the single-wall carbon nanotube patterned semiconducting surface (18). Later, Al2O3, PMMA (polymethyl methacrylate), PET (poly ethylene terephthalate) and other surface materials coated by carbon nanocomposite were reported to have pressure-resistivity characteristics (19-21). The designs either required multiple photolithography steps to fabricate the thin film structure or expensive equipment to facilitate carbon black integration. Poor adhesion of carbon nanopowder on the surface of materials also raised repeatability issue regardless of the advances in surface coating techniques (22). In addition, to the best of our knowledge, the reported devices have only been applied to pressure measurement. Higher shear stress and reactive working solutions may destabilize the coated carbon film and explain the reason why it is generally not used for flow rate measurement.

In this article, we developed a highly portable and cost-efficient piezoresistive microfluidic sensor that is capable of both pressure and flow rate measurements with an external impedance analyzer. Compared to the current flow meters that cost more than 1000 USD per unit, our device cost less than two USD to fabricate. The sensor

contains two conductive PDMS films and two metal electrodes directly fabricated next to the main flow channel. This design allows the sensor to be embedded into any microfluidic device and monitor pressure changes in real time without interrupting fluid flow. It's also possible to integrate multiple units along the flow channel for flow rate measurement. In contrast to the previous piezoresistive microfluidic sensors, the fabrication process is significantly simplified by doping carbon blacks nanocomposite into the PDMS to modify its electric conductivity, thus, alleviate the adhesion problem. In the first part of this paper, we optimized the geometry of the membrane and the operating frequency of the impedance analyzer. We then investigated the pressure responses of PDMS/CB membrane to correlate the impedance measurement and applied pressure. Lastly, two sensors were integrated into a microfluidic chip for flow rate measurement and the test results were compared to a commercial flow sensor for evaluation.

6.3 Materials and Methods

6.3.1 Microfabrication

The microfluidic device consists of a main flow channel and two separate pressure sensors in order to detect the pressure gradient. Each sensing unit contains two metal electrodes separated from the flow channel by PDMS/CB membranes, Figure 6-1a. To locally pattern each membrane, we used a multistage soft lithographic process we have reported previously (23). Briefly, we fabricated the soft lithographic microchannel mold using a negative photoresist, SU-8 3050 (Microchem Corp). The main flow channel is 400 μm in width and 3cm long. Each sensing unit consists of two gallium electrode

channels separated from the main flow channel by a 20 μm thick gap, Figure 6-1b. Carbon black nanocomposite (Sigma-Aldrich, 633100) was combined with a 1:5 weight ratio of PDMS elastomer. The resulting nanocomposite gel was then patterned into each gap between the channels. After removing the excess gel using a razor blade, a 1:10 mixture of PDMS elastomer and curing agent was poured atop the mold and allowed to cure for an hour at 80°C. The cured PDMS slab was gently peeled off the mold and fluid ports at the channel inlet and outlet were punched using a 0.75 mm biopsy punch (Ted Pella, Inc.). The device and a glass coverslip were exposed to oxygen plasma (Tesla) and immediately aligned and sealed under an inverted microscope. Finally, the chip was baked for 24 hours at 80°C to enhance bond strength. To fabricate each metal electrode, solid gallium metal (Sigma-Aldrich, 263265) and the PDMS chip were heated to 40 °C on a hot plate. With a melting temperature of 29.7 °C, the newly melted liquid gallium was loaded into a 1 mL plastic syringe and immediately injected into the electrode channels. Electrical connection was made using 0.75 mm diameter copper wire leads inserted into each electrode injection hole.

6.3.2 Experimental setup

1X PBS was used as the working solution for all the sensor characterizations and tests. Briefly, a PBS solution was driven by a constant pressure flow system (Elveflow) and directed into the main flow channel. A commercial flow sensor (Elveflow) was attached to the inlet for real time flow rate measurement during sensor tests. An electrical connection was made between the gallium electrodes and impedance spectrometer (Agilent, HP4192A) through copper wire leads, which were inserted into the gallium electrode ports. Two separate Labview scripts were used in order to perform impedance

measurements. The first script used measured the magnitude of impedance (|Z|) and angle (θ) while sweeping the applied frequency at a specific step size from start to end frequency. The second script used measured both |Z| and θ, while holding the applied frequency constant, in real time. All measurements acquired from experiments were exported and analyzed with software.

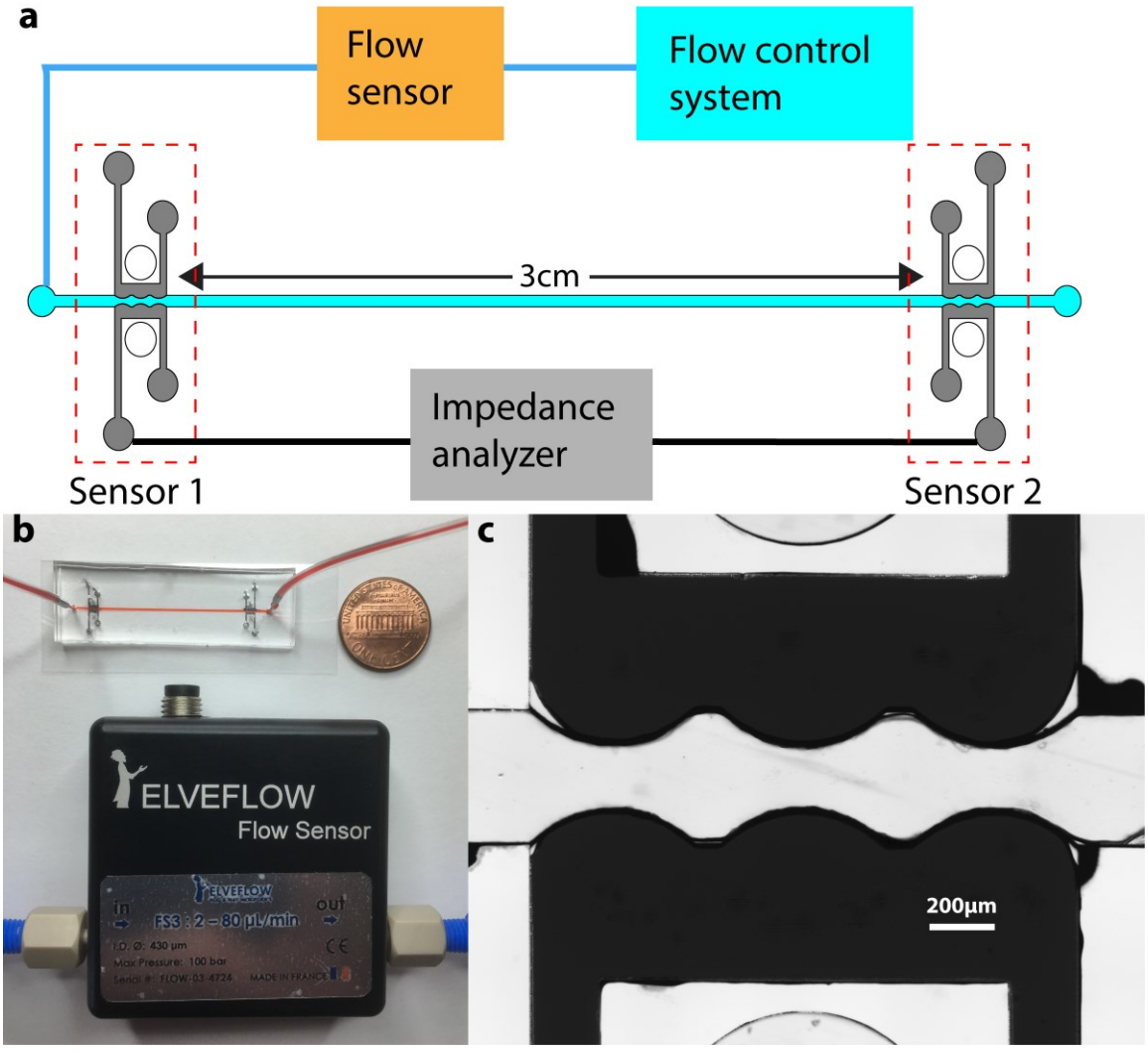

Figure 6-1. An illustration of experiment setup. (a) A schematic shows experiment setup. An external flow control system and flow meter were used to deliver pressure to sensor device. Sensor device itself contains two sensing units along the main channel, one near inlet, and one near outlet. Both pairs of electrodes were connected to an impedance

analyzer. (b) Comparison between the commercial sensor and the sensor we developed. The actual sensing unit is much smaller so that can be easily embedded onto other microfluidic designs. (c) A zoom-in subfigure shows the electrodes and carbon-PDMS membrane. The carbon-PDMS membranes form the channel walls that can deform under pressure. The membranes are 20um thick and designed to this semi-sphere shape in order to maximize deformation.

6.4 Results and Discussions

6.4.1 Working mechanism

The pressure sensing system consists of two parts, the deformable PDMS/CB membranes and external impedance analyzer. The thin layer of conductive PDMS/CB membranes is fabricated directly to the flow channel sidewalls. When the main flow channel is pressurized, the normal stress applied to the sidewall deforms the membranes and changes the sidewall electrical resistance. The membrane resistance can be transduced to an external impedance analyzer connected through the gallium electrodes. Because the resistance variation is proportional to the membrane deformation, which is a function of the applied pressure inside the flow channel, by correlating the impedance measurements to the applied pressure, we are able to measure the pressure changes inside the main flow channel in real time. To further monitor the flow rate, two pressure sensing units were embedded to both ends of a main flow channel. We measured the pressure at each end and then calculated the actual flow rate with a known hydrodynamic resistance between the two sensors.

6.4.2 Optimize the operation frequncy

The external impedance analyzer has a working frequency ranges from 0 to 13 MHz. In order to achieve a better sensitivity, we optimized the operating frequency by running the frequency sweep at different applied pressures. We use a Labview script to sweep a wide frequency range, from 500 Hz to 200 kHz, and plot the measured impedance verse frequency. Then the experiment was repeated multiple times under different applied pressure. Figure 6-2 shows the sweep curves for three applied pressures, 10mbar, 50mbar and 100mbar. Under low frequency, the AC field is not strong enough to overcome the membrane resistance and the corresponding impedance is larger than the reading limit (2 Mohm). As frequency increases, the AC field becomes stronger and penetrates the PDMS/CB membrane. The corresponding impedance starts to drop and eventually reaches steady state. We found the largest impedance difference at an applied frequency of 1.5 kHz, which was as the operating frequency for all subsequent experiments. Note that at high frequency ranges, the impedance becomes very small thus the pressure difference is barely noticeable.

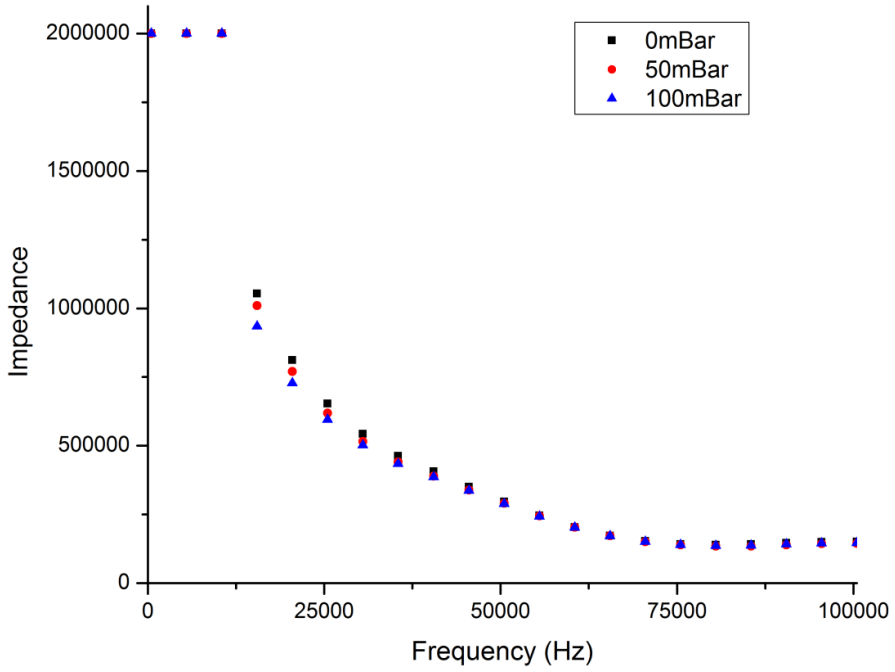

Figure 6-2. Frequency sweep curves under three different pressures. Under each applied pressure, we used impedance analyzer to sweep a wide range of frequency, from 1kHz to 100kHz, and record corresponding impedance. The upper detection limit of our impedance analyzer is 2 MOhms, seen as the flat segment. Impedance decreases dramatically as operation frequency goes up and reaches minimum after 75kHz. We observed the maximum impedance difference under three applied pressures around 15-20kHz, which also gives the best detecting senility.

6.4.3 Pressure sensor calibration

Next, we characterized the pressure sensor to correlate the impedance measurements with local pressure changes by plotting the step curve. To do that, we kept the impedance analyzer applying a constant frequency of 1.5 kHz while alternating the external pressure source. The outlet was blocked to achieve uniformed pressure across the entire channel. Then we adjusted the external pressure and impedance variation of the

inlet sensor was recorded in real time, shown in Figure 6-3. At each pressure, we recorded quadruplicated data sets and each set contains 10 to 15 data points. To achieve better accuracy and avoid external interferences, we used OriginPro, data analysis software, to create a baseline according to the impedance reading at 0 mbar. Thus, all the data points at 0mbar were normalized to the same level after subtracting the baseline. This step guarantees all the impedance readings have the same reference point, therefore impedance changes are only caused by pressure variation inside the flow channel. Then the entire process was repeated on another sensor near the outlet.

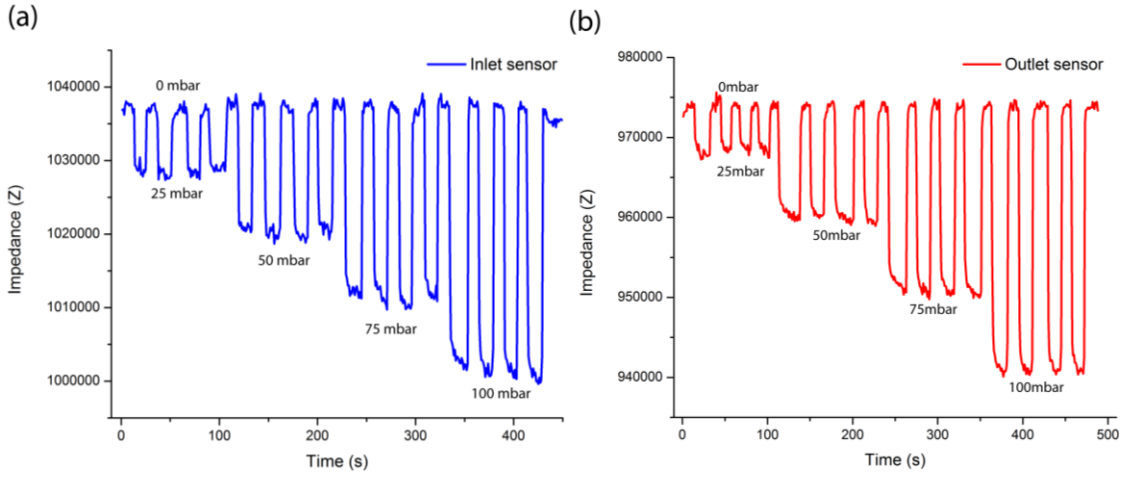

Figure 6-3. Data plots show the corresponding impedance under different pressures, blue for the sensing unit near inlet, red for the unit near outlet. For both sensors, the reference point was the top line at zero pressure. Other three pressures tested here were 25mbar, 50mbar, 75mbar and 100mbar. Sensor can response to pressure change within a second but require certain time to reach steady state.

We calculated the averaged impedance for each pressure with all the data points and plotted it against the applied pressure (Figure 6-4). Figure 6-4 shows two calibration curves for the inlet and outlet pressure sensors, respectively. The impedance decreases linearly with increased pressure from 0mbar to 100mbar. The good linearity shows this

new created sensor works as well as other reported piezoresistive sensor. The error bars represent the standard deviation calculated from all data points under the same pressure, which proves the robustness of the sensor's accuracy.

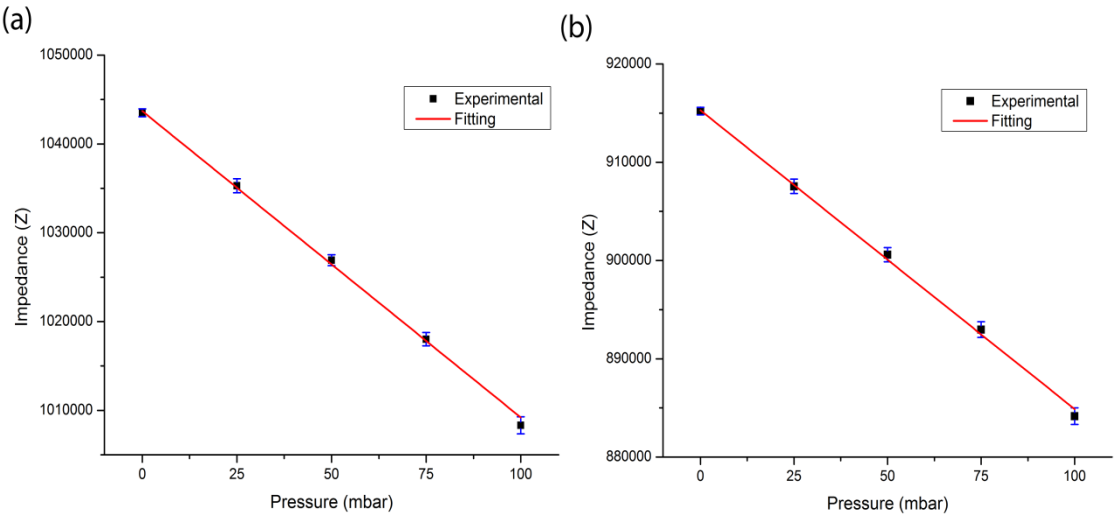

Figure 6-4. Calibration curves correlate impedance readings to local pressures. The calibration curves were constructed from data plots in Figure 6-3. Impedance data was extracted from Figure 6-3 and averaged to calculate actual impedance under each pressure. Linear fitting builds the mathematical relation used to back calculate local pressure. Small error bars shows the reliability of sensor performance.

6.4.4 Flow rate measurements

One advantage of this new designed sensor is that the sensor can be integrated directly to the microfluidic channel sidewall without blocking fluid flow. This allows the sensor to be applied to any existing microfluidic network and monitor local pressure gradient or flow rate. Compared to current commercial flow meters, the new sensor has the capability for on-chip integration, which allows much smaller sensor size, shown in Figure 6-1. To turn this pressure sensor to an actual flow meter that can monitor flow rate, we integrated two sensors atthe inlet and outlet regions of the microfluidic channel. Each

sensor can monitor the local pressure changes individually. Then the pressure values from both sensors were used to determine the pressure gradient between the two points. The flow rate inside the microchannel was then calculated with hydrodynamic resistance and compared to the actual flow rate measured by an external flow meter. Figure 6-6 shows the comparison between the actual flow rate and the flow rate from the sensor within the inlet pressures range from 25 mbar to 100 mbar. All the impedance measured flow rates are close to the actual flow rate except the 100 mbar. We assume the relatively large pressure pushes the elastic film to the limit of deformation and thus causes certain non-linearity between applied pressure and impedance reading. The actual impedance reading at 100 mbar is lower than the linear fitting curve, shown in Figure 6-4, which explains the large deviation. But other than 100 mbar, the flow rate measurements are similar to the real value with 1-2 μl/min standard deviations, as the error bars show.

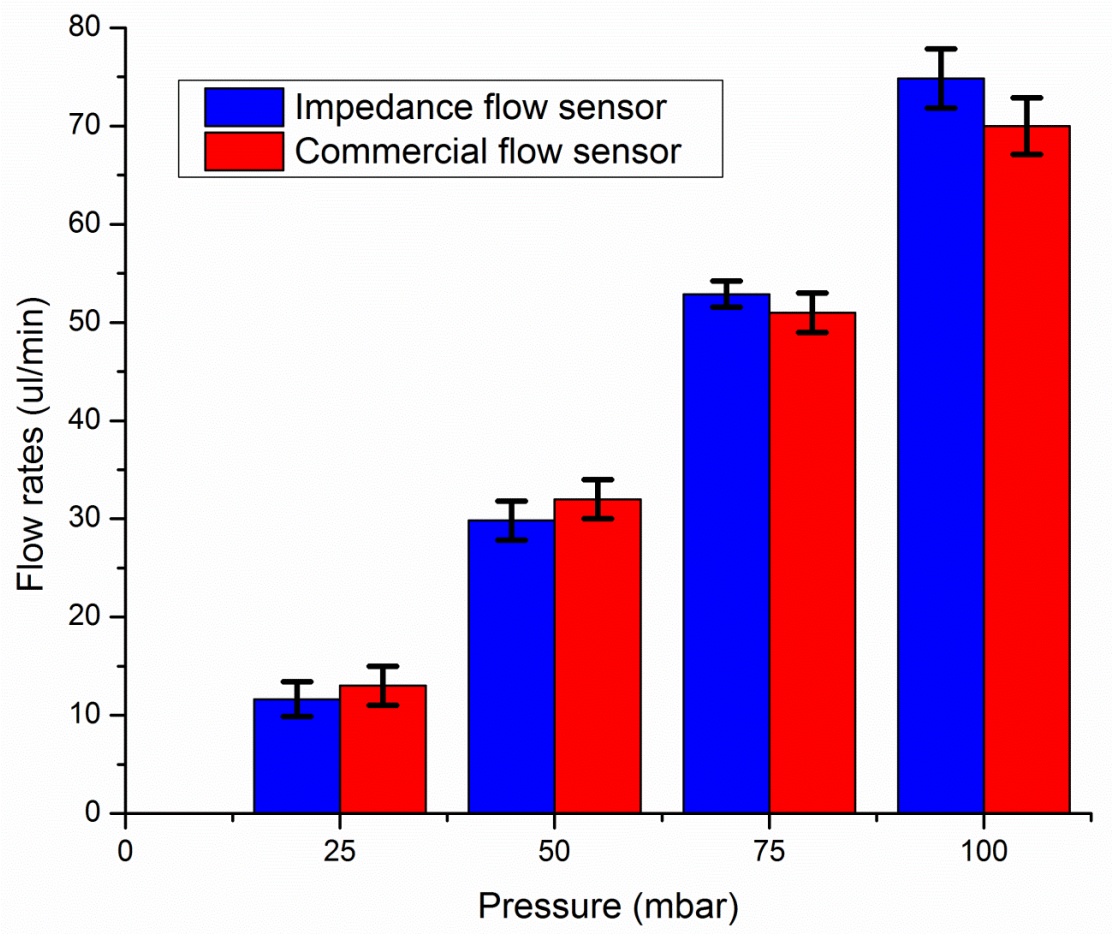

Figure 6-5. Compare flow rates measured by created flow meter to commercial sensor. The blue bars represent measurements acquired from created on-chip flow meter and the red bars represent results from commercial sensor. Both sensors measured flow rates from 10 to 80 ul/min, a common range in most microfluidic applications. All measurements are pretty close with less than 10% errors.

6.5 Conclusion

We developed an on-chip cost-efficient piezoresistive microfluidic sensor that is capable of both pressure and flow rate measurements. Compared to the current flow meters that cost more than 1000 USD per piece, the new sensor has a fabrication cost that

is less than 2 USD. The sensor has two integrated conductive PDMS films on the microfluidic side wall. An impedance analyzer is connected to the elastic PDMS film through the gallium metal electrodes. The film deformation caused by internal pressure changes can be translated into electrical resistance variations and further read by the impedance analyzer. This design allows the sensor to be integrated to any microfluidic devices and monitor pressure changes or measure flow rate in real time without interrupting the fluidic flow. In contrast to the previous piezoresistive microfluidic sensors, the new designed sensor features simple fabrication process, low cost, on-chip integration and the capability to monitor both pressure and flow rate information. We characterized the created sensor to determine the linear relation between pressure and impedance changes. The impedance value decreased linearly with increasing applied pressure from 0 to 100mbar. We then used the sensor to measure the local pressure gradient inside microfluidic channel and plotted the pressure changes with standard deviation. Small error bars proved the robustness and accuracy of the measurements. Last we developed the actual flow meter with two integrated sensors and applied it to a microfluidic chip. The flow rates at variety of external pressures were measured and compared to the actual flow rates from other commercial flow meters. The measured flow rates range from 10 μl/min to 80 μl/min and very close to the actual flow rate with 1-2 μl/min deviation. Considering cost efficiency and the capability for on-chip integration, this new development sensor has huge potential in real time fluidic monitoring for increasingly complicated microfluidic systems.

References

1. Tao Xu, Chakrabarty K. A Droplet-Manipulation Method for Achieving High-Throughput in Cross-Referencing-Based Digital Microfluidic Biochips. Computer-Aided Design of Integrated Circuits and Systems, IEEE Transactions on. 2008;27(11):1905-17.

2. Liu XY, Sun Y. 9 - Microfluidic devices for single-cell trapping and automated micro-robotic injection. In: Li X(, Zhou Y, editors. Microfluidic Devices for Biomedical Applications. Woodhead Publishing; 2013. p. 365e.

3. Hoffmann P, Ji H, Moritz RL, Connolly LM, Frecklington DF, Layton MJ, et al. Continuous free-flow electrophoresis separation of cytosolic proteins from the human colon carcinoma cell line LIM 1215: a non two-dimensional gel electrophoresis-based proteome analysis strategy. Proteomics. 2001;1(7):807.

4. Kuo JTW, Yu L, Meng E. Micromachined Thermal Flow Sensors—A Review. Micromachines. 2012;3(3).

5. Chen J, Fan Z, Zou J, Engel J, Liu C. Two-Dimensional Micromachined Flow Sensor Array for Fluid Mechanics Studies. J Aerospace Eng. 2003;16(2):85.

6. Sabat N, Santander J, Fonseca L, Grcia I, Can C. Multi-range silicon micromachined flow sensor. Sensors & Actuators A: Physical. 2004;110(1-3):282.

7. R. J. Adamec, D. V. Thiel. Self Heated Thermo-Resistive Element Hot Wire Anemometer. IEEE Sensors Journal. 2010;10(4):847-8.

8. Wang Y, Chen C, Chang C, Lin C, Lin C, Fu L, et al. MEMS-based gas flow sensors. Microfluidics and Nanofluidics. 2009;6(3):333.

9. T. S. J. Lammerink, J. C. Ltters, R. J. Wiegerink, J. Groenesteijn, J. Haneveld. Single chip flow sensing system with a dynamic flow range of more than 4 decades. 2011 16th International Solid-State Sensors, Actuators and Microsystems Conference; ; 2011.

10. Smith R, Sparks DR, Riley D, Najafi N. A MEMS-Based Coriolis Mass Flow Sensor for Industrial Applications. IEEE Trans Ind Electron. 2009;56(4):1066.

11. J. Haneveld, T. S. J. Lammerink, M. Dijkstra, H. Droogendijk, M. J. de Boer, R. J. Wiegerink. Highly sensitive micro coriolis mass flow sensor. 2008 IEEE 21st International Conference on Micro Electro Mechanical Systems; ; 2008.

12. Y. Wang, Z. Li, L. Qin, M. K. Chyu, Q. M. Wang. Theoretical and experimental studies of a surface acoustic wave flow sensor. IEEE Transactions on Ultrasonics, Ferroelectrics, and Frequency Control. 2012;59(3):481-90.

13. Lima R, Wada S, Takeda M, Tsubota K, Yamaguchi T. In vitro confocal micro-PIV measurements of blood flow in a square microchannel: The effect of the haematocrit on instantaneous velocity profiles. J Biomech;40(12):2752-7.

14. Meng E, Li P, Tai Y. A biocompatible Parylene thermal flow sensing array. Sensors & Actuators A: Physical. 2008;144(1):18.

15. Lee G, Kuo T, Wu W. A novel micromachined flow sensor using periodic flapping motion of a planar jet impinging on a V-shaped plate. Exp Therm Fluid Sci. 2002;26(5):435-44.

16. Wichmann MHG, Buschhorn ST, Gehrmann J, Schulte K. Piezoresistive response of epoxy composites with carbon nanoparticles under tensile load. Phys Rev B. 2009;80(24):245437.

17. and XY. A carbon nanotube/cement composite with piezoresistive properties. Smart Mater Struct. 2009;18(5):055010.

18. Grow RJ, Wang Q, Cao J, Wang D, Dai H. Piezoresistance of carbon nanotubes on deformable thin-film membranes. Appl Phys Lett. 2005;86(9):093104.

19. Stampfer C, Helbling T, Obergfell D, Schberle B, Tripp MK, Jungen A, et al. Fabrication of single-walled carbon-nanotube-based pressure sensors. Nano Letters. 2006;6(2):233.

20. Loh KJ, Lynch JP, Shim BS, Kotov NA. Tailoring Piezoresistive Sensitivity of Multilayer Carbon Nanotube Composite Strain Sensors. J Intell Mater Syst Struct. 2008;19(7):747-64.

21. Inpil Kang and Mark J Schulz and Jay H Kim and Vesselin Shanov and, Donglu Shi. A carbon nanotube strain sensor for structural health monitoring. Smart Mater Struct. 2006;15(3):737.

22. Xie R, Wang J, Yang Y, Jiang K, Li Q, Fan S. Aligned carbon nanotube coating on polyethylene surface formed by microwave radiation. Composites Sci Technol. 2011;72(1):85-90.

23. Fu X, Gagnon Z. Contactless microfluidic pumping using microchannel-integrated carbon black composite membranes. Biomicrofluidics. 2015;9(5):054122.

7. Conclusions and Future Work

7.1 Conclusions

To date, many microfluidic designs reported that optimized design could enhance the sensitivity of uTAS system or allow for faster operation. However, the development of on-chip sample preparation module has just started and far behind the progress made in detection. As a result, regardless of all the advances in detection strategies, most uTAS devices still require a series of benchtop process to simplify sample complexity. Sample consumption and extended processing time during benchtop operation completely offset the benefits of utilizing uTAS. While on-chip sample preparation remains challenging, this thesis seeks to address two main obstacles researchers are facing during on-chip sample preparation module development: continuity and integration. Despite the quick growth of module functions, most sample preparation devices still work in the batch model and require certain sample collection mechanisms in order to proceed to next step. In other words, current sample preparation modules are lacking of capability to process samples in a continuous manner, which significantly increases the processing time. Contamination induced during sample collection may also impact detection results and hinder uTAS reliability. In the meantime, essential on-chip flow control modules that can facilitate chip connection and automation are missing from most uTAS designs. Many uTAS still relies on external driving forces to power its function, thus bring portability issues to uTAS.

In this thesis, we proposed to solve the continuity challenge by developing a new membrane-based electrokinetic platform with the capability to realize continuously on-chip sample preparation. This platform not only delivers uniformed three-dimensional electric field into microfluidic channels in an effective and robust manner, also has superiorities in fabrication, portability and cost aspects. Two common sample preparation techniques, separation and enrichment, were demonstrated using free flow electrophoresis technology. On the other hand, several on-chip flow control modules essential for microfluidic integration have been reported in order to tackle the chip integration challenge. We applied the newly designed platform, once again, into on-chip fluid control units, including a micro-pump, a sample injector, a fluid controller and a flow sensor. Presented modules all feature a sidewall design that allows for direct integration into common microfluid designs without impacting the original functions. This feature not only simplifies chip-to-chip connection, also provides a potential strategy for integrating multi-functional flow control module onto microfluidic chips.

In the first chapter, we introduced the background of microfluidics technology and uTAS concept. uTAS typical consist of a core sensing module and several assisting sample processing modules. While many techniques have been adopted in developing the core sensing module, the development efforts on sample processing remain limited until recent years. The unbalance between core detection technique advances and limited on-chip sample preparation modules undermines further utilizations of uTAS. We briefly summarized current on-chip sample preparation work related to our research work, along with the two biggest challenges of on-chip sample preparation. This leads to Chapter 2, where current microfluidic platforms designed for electrokinetic applications were

discussed. We proposed new membrane structure, which consists gallium metal electrode separated by thin layers of carbon nano-composite membrane. A simple electrocurrent model followed to demonstrate its working mechanism and characterize performance efficiency. An extensive comparison between this new platform and other reported devices then reviewed the advantages and drawbacks of this platform. In the end of this chapter, a detailed fabrication process for building this membrane structure was included.

In chapter 3, we presented the free flow electrophoresis module developed with the reported platform. Free flow device features sample processing in a continuous manner, such as free flow separation, enrichment or mixing. We demonstrated two electrophoresis-based free flow applications, free flow zone electrophoresis and free flow isotachophoresis. Both applications serve as powerful tools for charged molecules separation and concentration. Due to the continuous nature of free flow design, the sample preparation modules we created can be easily integrated into a downstream sensing unit, which completely eliminates manual sample collections.

Chapter 4-6 constructed the second block of this thesis, where on-chip flow control modules essential for chip integration were addressed. We demonstrated a micro electro-osmotic pump and a sample injection, a micro flow sensor in chapters 4, 5 and 6, respectively. On-chip micro electroosmotic pumping offers an additional option to microfluidic driving force while flow and pressure sensor can actively collect real time fluid information used for feedback control. The combination of both modules allows a self-sufficient design of any uTAS and greatly facilitates uTAS automation. In addition to fluid pumping and monitoring, we also developed fluid control system consists multiple on-chip micro pumps and a control panel regulated through LabVIEW. The fluid control

system successfully proved its capability in fluid routing and sample injection, which may offer another possibility to construct automatic controlled uTAS.

7.2 Future Work

Current research has made great stride to develop an electrokinetic platform for on-chip sample preparation and both challenges have been addressed. Future investigations are needed to further our understanding of the fundamental mechanism as well extend platform applications to real world setting. We will discuss the future research directions in the following sections.

7.2.1 Surface characterization

In Chapter 2 we described the platform characterization work including calculating chip efficiency and comparing advantages of different platform designs. A key factor used for performance evaluation is the capability to minimize undesired surface reactions, such as electrode depletion, gas generation and electro-thermal flow. We compared three platform designs performing electrophoresis separation. Platform with direct integrated metal electrode suffered gas generation, Joule heating and electrode depletion. There are two reasons associate with it. One is the high current density caused by low system resistance, which also means excellent chip efficiency. On the contrary, no issue has been observed in PDMS insulator design. However, the proved low chip efficiency shows insulator design is inapplicable for electrokinetic applications. The ideas of avoiding surface reactions under high current density and improving chip efficiency become a dilemma and we have to trade off one way or the other. The solution falls on to the second reason for surface reactions: the physic properties of electrode materials.

Metals turn to give out electrons more easily compare to some inert materials, such as carbon or organic polymer. We observed higher current density change with gallium electrodes during cyclic voltammetry as gallium metal is more reactive than gold, which means it suffers severer surface reactions. On the other hand, carbon combined with PDMS remains the inert property and unlikely to give or take electrons from bulk fluid, which may explain why we did not observe surface reaction even with the same current density range. However, a comprehensive understanding of the mechanism behind using carbon polymer to suppress surface reactions has not been acquired. Further investigations shall focus on surface characterization using scan electronic microscopy or other similar tools to monitor the surface alternations under the electric field, for example, surface roughness, deformation or porosity. The electrochemical study shall be another powerful tool to characterize surface reaction types during operation. Reactions occur under metal and carbon electrode systems may be different, thus leads to a higher current density threshold before reactions occur.

7.2.2 Real sample processing and integration

In this thesis, we addressed the increasing demand of on-chip sample preparation and the main challenges associated with it. We presented several microfluidic devices capable of performing sample separation, enrichment, buffer pumping and flow control in chapter 3, chapter 4 and chapter 5, and successfully demonstrated the capability of manipulating charged species or fluid. However, for most experiment setups we introduced here, we used clean samples made from stock solutions instead of dirty samples, such as physiological samples. Physiological samples, for example, whole blood or urine, are considered “dirty” because of the presence of all types of biomolecules and

bioparticles, ranging from big cells to small ions, positive charges to negative charges. The benefit of using man-made sample is to avoid undesired components and simplify experiment. This allows us to demonstrate device capability without extended troubleshooting. Nevertheless, real physiological samples cannot be processed in one step and typically require multiple pretreatment modules to become "clean" enough for detection. It not only requires modular integration, also a robust working mechanism that can remain effective under the presence of interferential molecules. This leads to further troubleshooting work and device customization, which will become the biggest challenge on our way to push the platform into real world applications. Additionally, physiological samples also contain high ion concentrations, which results higher buffer conductivity. For electrokinetic applications, Faradaic reaction becomes more severe when buffer conductivity increases to mili-Siemens range. A high concentration of ions in bulk fluid will saturate electrode surface in a short time and reach the threshold density, which further leads gas formation and electrode depletion. Thus, how to avoid Faradaic reaction under physiological setting is another big challenge for real world applications.

The new developed platform shows great potential for modular integration, integration between sample preparation module and downstream sensor has not been completed yet. The main obstacle of integration lies in sample fractionation. The free flow design not only allows continuous sample collection that benefits processing speed, in the meantime, it also requires more precise flow control in order to fractionate sample stream right into connected sensor module. As a result, local flow meters or optical detection is needed for a close flow monitoring, which further complicates device setup.

Besides, we must consider the interaction between two connected modules and minimize interferences from modular integration.

Publications

Peer reviewed publications:

1. Fu, X., Mavrogiannis,N., Gagnon, Z., “Microfluidic Pumping, Routing, and Metering by Contactless Metal-Based Electro-osmosis”, Lab on a Chip, (2015), 15, 3600-3608

2. Fu, X., Gagnon, Z., “Contactless Microfluidic Pumping Using Microchannel-integrated Carbon Black Composite Membranes”, Biomicrofluidics, (2015), 9, 054122

3. Fu, X., Mavrogiannis,N., Ibo, M.,Crivellari, F., Gagnon, Z., “Microfluidic free-flow zone electrophoresis and isotachophoresis using carbon black nano-composite PDMS sidewall membranes”, Electrophoresis(2016)

4. Fu, X., Mavrogiannis,N., Gagnon, Z., “A low cost on-chip pressure and flow sensor with integrated carbon nano-composite transducer”, Sensor & Actuator B (2017) (Submitted)

6. Mavrogiannis,N., Ibo, Fu, X., M.,Crivellari, F., Gagnon, Z., “Microfluidics made easy: A robust low-cost constant pressure flow controller for engineers and cell biologists”, Biomicrofluidics 10, 034107 (2016)

7. Mavrogiannis,N., Fu, X., Desmond, M., Gagnon, Z., “Monitoring Microfluidic Interfacial Flows Using Impedance Spectroscopy”, Sensors and Actuators B Chemical (June 2016)

8. Mavrogiannis,N., Desmond, M., Fu, X., Gagnon, Z., “Microfluidic Mixing and Analog On-Chip Concentration Control Using Fluidic Dielectrophoresis”, Micromachines (Nov 2016)

Conferences:

Fu, X., Gagnon, Z., “Microfluidic Free Flow Electrophoresis Using Conductive PDMS Polymer Membranes” (2015 AIChE annual conference, USA)

Fu, X., Gagnon, Z., “Microfluidic free flow electrophoresis using tunable conductive PDMS polymer membranes” (18th International Symposium on FFF Field-Flow Fractionation, Germany, 2016)

Fu, X., Gagnon, Z., “Conductive Nano-composite Membranes For On-chip Microfluidic Electrokinetics” (2016 AIChE annual conference, USA)